THESIS FOR THE DEGREE OF DOCTOR OF PHILOSOPHY

Charting Circumstellar Chemistry of Carbon-rich AGB Stars

RAMLAL UNNIKRISHNAN

CHALMERS
UNIVERSITY OF TECHNOLOGY

Department of Space, Earth and Environment
Division of Astronomy and Plasma Physics
Chalmers University Of Technology
Gothenburg, Sweden 2025

Charting Circumstellar Chemistry of Carbon-rich AGB Stars

Ramlal Unnikrishnan

ISBN 978-91-8103-346-5

Acknowledgements, dedications, and similar personal statements in this thesis reflect the author's own views.

Doktorsavhandlingar vid Chalmers tekniska högskola
Ny serie nr 5803
ISSN 0346-718X

DOI: https://doi.org/10.63959/chalmers.dt/5803

Division of Astronomy and Plasma Physics
Department of Space, Earth and Environment
Chalmers University of Technology
SE-412 96 Gothenburg, Sweden
Telephone: +46 (0)31 772 1000
Email: ramlal.unnikrishnan@chalmers.se

Cover image: ALMA map of the HC_3N (colour) and SiC_2 (contours) line emission around the C-type AGB star II Lup. Representative molecules and a starry background have been added. *Credits: ALMA (ESO/NAOJ/NRAO) / R. Unnikrishnan / L. -Å. Nyman, 2024.*

This thesis has been prepared using LaTeX

Printed by Chalmers Reproservice
Gothenburg, Sweden, December 2025

Charting Circumstellar Chemistry of Carbon-rich AGB Stars

Ramlal Unnikrishnan
Department of Space, Earth and Environment
Chalmers University of Technology

Abstract

Stars of low to intermediate initial masses (~0.8 - 8 $M_{\odot}$) enter the asymptotic giant branch (AGB) phase in their late evolution. The intense mass loss during the AGB forms an extended circumstellar envelope (CSE) of chemically rich gas and dust around the star. These stars also form heavy elements via the *s*-process, and contribute substantially to the chemical enrichment of the interstellar medium (ISM).

Carbon-rich AGB stars present more chemically complex CSEs than their oxygen-rich counterparts. The chemical characterisation of carbon-star CSEs is crucial for unravelling the astrochemical networks that form complex molecules and dust. However, most of our current knowledge of the circumstellar chemistry in carbon-stars is based on observations and models of a single object, IRC+10 216, often regarded as the archetype carbon-star. To address this lack of sufficient sampling evident in the literature, this thesis presents the first spatially resolved, unbiased spectral survey of circumstellar molecular line emission from carbon-stars other than IRC +10 216, revealing their complex morphologies and chemical contents. We derive the emitting region sizes and LTE fractional abundances for a large number of molecular species.

We further employ non-LTE radiative transfer models, constrained using a large number of interferometric and single-dish observations, to determine both the physical and chemical characteristics of these envelopes. We derive the circumstellar abundance distributions of various molecular species (CS, SiO, SiS), and compare these to IRC +10 216, informing state-of-the-art chemical models as well. The large amount of observational constraints available also helps illuminate the limitations inherent to such modelling. Overall, this work leverages the high sensitivity and angular resolution of the ALMA interferometer, combined with detailed radiative transfer and chemical models, to provide a broader, more generalised understanding of the chemistry in carbon-star CSEs, extending beyond IRC +10 216.

Keywords: Stars: AGB and post-AGB – stars: carbon – stars: winds, outflows – stars: mass-loss – stars: abundances – submillimeter: stars – circumstellar matter – radiative transfer – astrochemistry.

എത്രയും പ്രിയപ്പെട്ട മാതാപിതാക്കൾ ഉണ്ണിക്കൃഷ്ണൻ നായർക്കും ശ്രീലതയ്ക്കും,
പ്രപഞ്ചത്തോളമനന്തമായ, നിസ്സീമമായ സ്നേഹത്തിന്.

To my most beloved parents Unnikrishnan Nair and Sreelatha,
for love boundless, and infinite as the universe.

"നിന്നാത്മ ശിഖരത്തിലൊരു കൂടു തന്നു,
എന്റെ ചിറകിനാകാശവും നീ തന്നു." [1]

[1] മധുസൂദനൻ നായർ, വി. (Madhusoodanan Nair, V.) 'ഇരുളിൻ മഹാനിദ്രയിൽ'. Order of verses changed.

താരകളേ, കാൺമിതോ നിങ്ങൾ [...]
പാലപൂത്ത പരിമളമെത്തി-
പ്പാതിരയെപ്പുണർന്നൊഴുകുമ്പോൾ;
മഞ്ഞണിഞ്ഞു, മദാലസയായി
മണ്ണുചന്ദ്രിക നൃത്തമാടുമ്പോൾ,
[...] താദൃശോത്സവമുണ്ടോ, കഥിപ്പിൻ
താരകളേ, നിങ്ങൾതൻ നാട്ടിൽ? ...
[...] ഹന്ത, യിന്നതിൻ ചിത്തരഹസ്യ-
മെന്തറിഞ്ഞു, ഹാ, ദൂരസ്ഥർ നിങ്ങൾ?[2]

കവിഭാവനയ്ക്കും ശാസ്ത്രാന്വേഷണത്തിനും ഒരുപോലെ പ്രിയങ്കരരായ ദൂരതാരകങ്ങളെപ്പറ്റി ഒരെളിയ പഠനശ്രമം.

[2] ചങ്ങമ്പുഴ (Krishna Pillai, C.), 'സ്പന്ദിക്കുന്ന അസ്ഥിമാടം'. Verses selected intermittently and reordered.

Research Contributions

This thesis is based on the work contained in the following papers:

[I] **R. Unnikrishnan**, E. De Beck, L. -Å. Nyman, H. Olofsson, W. H. T. Vlemmings, D. Tafoya, M. Maercker, S. B. Charnley, M. A. Cordiner, I. de Gregorio, E. Humphreys, T. J. Millar, and M. G. Rawlings:
Charting circumstellar chemistry of carbon-rich AGB stars I. ALMA 3 mm spectral surveys.
Astronomy & Astrophysics, Volume 684, A4 (2024).

[II] **R. Unnikrishnan**, M. Andriantsaralaza, E. De Beck, L.-Å. Nyman, H. Olofsson, W. H. T. Vlemmings, M. Maercker, M. Van de Sande, T. Danilovich, T. J. Millar, S. B. Charnley, and M. G. Rawlings:
Charting circumstellar chemistry of carbon-rich AGB stars II. Abundances and spatial distributions of CS.
Astronomy & Astrophysics, Volume 699, A48 (2025).

[III] **R. Unnikrishnan**, E. De Beck, L.-Å. Nyman, H. Olofsson, W. H. T. Vlemmings, M. Maercker, M. Van de Sande, T. J. Millar, T. Danilovich, M. Andriantsaralaza, S. B. Charnley, and M. G. Rawlings:
Charting circumstellar chemistry of carbon-rich AGB stars III. SiO and SiS abundances.
Submitted to Astronomy & Astrophysics.

Other publications by the author, not included in this thesis:

- D. Tafoya, J. A. Toalá, **R. Unnikrishnan**, W. H. T. Vlemmings, M. A. Guerrero, S. Kimeswenger, P. A. M. van Hoof, L. A. Zapata, S. P. Treviño-Morales, and J. B. Rodríguez-González:
First images of the molecular gas around a born-again star revealed by ALMA.
The Astrophysical Journal Letters, Volume 925, L4 (2022).

- D. Tafoya, P. A. M. van Hoof, J. A. Toalá, G. Van de Steene, S. Randall, **R. Unnikrishnan**, S. Kimeswenger, M. Hajduk, D. Barría and A. Zijlstra:
The heart of Sakurai's object revealed by ALMA.
Astronomy & Astrophysics, Volume 677, L8 (2023).

- T. Schirmer, T. Khouri, W. H. T. Vlemmings, G. Nyman, M. Maercker, **R. Unnikrishnan**, B. Bojnordi Arbab, K. K. Knudsen, and S. Aalto:
An empirical view of the extended atmosphere and inner envelope of the asymptotic giant branch star R Doradus. II. Constraining the dust properties with radiative transfer modeling.
Astronomy & Astrophysics Volume 704, A4 (2025).

- A. Roshi Damodaran, L. Anderson, J. Dey, M. Padovani, **R. Unnikrishnan**, A. Zavagno, G. M. Umana, J. D. Pandian, J. van den Eijnden, G. Sabatini, K. L. Emig, A. Traficante, and Á. Sánchez-Monge:
The Impact and Environment of Massive Stars and Stellar Clusters.
Submitted to 'Advancing Astrophysics with the SKA II'.

- A. Traficante, C. Mininni, F. Cavallaro, [...] M. Audard, I. Jimenez-Serra, T. L. Bourke, B. Mookerjea, **R. Unnikrishnan**, [...] K. Wang, and T. Wilson:
The 10-15 GHz radio continuum survey of the Galactic Plane with SKAO.
Submitted to 'Advancing Astrophysics with the SKA II'.

- M. Andriantsaralaza, E. De Beck, **R. Unnikrishnan**, and the DEATHSTAR collaboration:
DEATHSTAR - Nearby AGB stars with the Atacama Compact Array III. Mass-loss rates for a sample of carbon-stars.
Manuscript intended for submission to Astronomy & Astrophysics.

Acknowledgements

There is a long list of people who have contributed in various ways to this project, and have helped and supported me a lot during this Ph.D. journey.

First and foremost, I wish to express my deepest gratitude to my Ph.D. supervisor, Dr. Elvire De Beck, for simply being the best supervisor I could ever imagine working with, far exceeding every expectation of supervision I had before taking up this position. You have taught me a lot of wonderful science, and always addressed my every little doubt and question with never-ending patience. You have also contributed greatly to my overall development as a researcher, be it by encouraging me to attend various workshops and conferences, or by sending me to Chile for observations, to just name a few things. Thank you, Elvire, from the bottom of my heart, for guiding me these past five years. If I had to select a supervisor again, I am certain I would choose you without a moment's hesitation.

Next, I would like to thank Dr. Lars-Åke Nyman and Prof. Hans Olofsson. It is indeed a great honour and privilege to be called your student. Lars, I can never thank you enough for always finding the time to be involved in the project, even from continents apart. Hans, thanks a lot for your expert advice and impeccable guidance throughout, and for helping me navigate the writing of my first research paper. My sincere gratitude also to Prof. Wouter Vlemmings, for being my Ph.D. examiner. Thank you, Wouter, for the many spontaneous discussions, and for helping me on many occasions as if I were your own student. My thanks to Dr. Matthias Maercker, for being an amazing co-supervisor and line manager. You strive tirelessly to ensure that the work environment is continuously improved for all of us. You make AoP a better place. Your constant reassurances have helped me manage the pressure of academic research and continue onwards on many occasions. I also thank Dr. Theo Khouri, for his valuable comments and suggestions throughout this project.

I do not have words to express my gratitude to my dear friend and mentor Dr. Daniel Tafoya. Daniel, you have been an amazing teacher, perhaps even the best I have ever had, and simultaneously one of my closest friends. I could not have done this without you. You share, to the same extent or probably more, my childish curiosity towards space and astronomy. I shall always cherish our countless random conversations, little moments of frustration and breakthroughs during the data processing days, and our many long fikas and dinners.

Next, I would like to thank my dear friends and colleagues, Behzad Bojnordi Arbab and Dr. Miora Andriantsaralaza. Behzad and Miora, I shall always treasure the moments of knowledge and fun we shared, be it at the office, the ping-pong table,

or during our travels. Many thanks to Behzad for finding time to teach me bits and pieces of his immensely beautiful language, Persian, as well. I could never have asked for a better office mate than you. Thank you Miora, for your significant contribution to my PhD project too. I also want to thank my close friends and colleagues Asnakew Bewketu Belete, Mamiko Sato, and Santiago Del Palacio. It has been a pleasure to share a department with you all. I also thank all my fellow Ph.D. students and postdocs, Kiana, Chentao, Mark, Thiébaut, Alex, and Alejandro, to name a few, and everyone else at AoP and OSO as well.

I also wish to thank my external collaborators, Marie, Taissa, Tom, and others. A special thanks to Tom for making my childhood dream of watching Manchester United play at Old Trafford come true. Many thanks also to Dr. Per Bergman for his patient replies to all my queries about radiative transfer and the ALI code. I want to thank my Indian scientific mentors, Anish, Desh, Bhaswati, and Ananta, whose exemplary guidance and support during my Master's was foundational in equipping me with the necessary skills to pursue this PhD. I also thank all my friends, both in India and Sweden, for their continuous support and encouragement.

I express my sincere gratitude to Prof. Dr. Karl Menten, for introducing me to the field of sub-millimeter astronomy. You shall forever be fondly remembered by the astronomy research community.

അച്ഛനമ്മമാരോടുള്ള കടപ്പാടറിയിക്കാൻ മാത്രം ആംഗലേയഭാഷ അപൂർണ്ണമാകുന്നു. അല്ലെങ്കിലും എന്തിനൊക്കെയാണ് നന്ദിപറയുക? തിരിഞ്ഞുനോക്കാൻ ഓർമകൾ മുഴുവൻ സ്നേഹം മാത്രം കരുതിവെച്ചതിന്. ഇഷ്ടപ്പെട്ട പഠന/ഗവേഷണ മേഖലകൾ തിരഞ്ഞെടുക്കാൻ പിന്തുണച്ചതിന്. കൈപിടിച്ചതിന്, വഴിതെളിച്ചതിന്, ഒറ്റപ്പെടലെന്നാലെന്തെന്ന് ഇന്നേവരെ ഞാനറിയാതിരിക്കുന്നതിന്. നെത്രുദയെ വായിക്കുന്നതിനുമെത്രയോ മുന്നേതന്നെ അറിയപ്പെടാത്ത മനുഷ്യത്വമായെനിക്ക് സാഹോദര്യം നൽകിയതിന്[3]. 'അന്യജീവനുതകി സ്വജീവിതം ധന്യമാക്കുമമലേ വിവേകികൾ'[4] എന്നാശാൻ. ജീവിതമൊന്നാകെ എനിക്കായി നീക്കിവെച്ചതിന്.

Ramlal Unnikrishnan
Gothenburg, December 2025

[3] Neruda, P., 'A mi Partido' Translated from the Spanish: "Me has dado la fraternidad hacia el que no conozco"
[4] കുമാരനാശാൻ (Kumaran Asan, N.), 'നളിനി'

List of abbreviations

ACA : Atacama Compact Array
AFGL : Air Force Geophysical Laboratory
AGB : Asymptotic giant branch
ALI : Accelerated lambda iteration
ALMA : Atacama Large Millimeter/submillimeter Array
AOS : Array Operations Site
APEX : Atacama Pathfinder EXperiment
CDMS : Cologne database for molecular spectroscopy
CNO : Carbon-Nitrogen-Oxygen
CSE : Circumstellar envelope
DARWIN : Dynamical Atmospheres and Radiation-driven Wind models with Implicit Numerics
DEATHSTAR : DEtermining Accurate mass-loss rates for THermally pulsing AGB STARs
DSB : Double side band
EHT : Event Horizon Telescope
ESA : European Space Agency
ESO : European Southern Observatory
FAST : Five-hundred-meter Aperture Spherical radio Telescope
FDU : First dredge-up

FIR : Far-infrared
GARD : Group for Advanced Receiver Development
HB : Horizontal branch
HBB : Hot bottom burning
HIFI : Heterodyne Instrument for the Far-Infrared
HR : Hertzsprung-Russell
IF : Intermediate frequency
IR : Infrared
IRAM : Institut de Radioastronomie Millimetrique
IRAS : Infrared Astronomical Satellite
IRC : Infrared catalog
ISM : Interstellar medium
ISO : Infrared Space Observatory
ISRF : Interstellar radiation field
JWST : James Webb Space Telescope
KIDA : KInetic Database for Astrochemistry
kpc : kiloparsec
LO : Local oscillator
LPV : Long-period variable
LTE : Local thermodynamic equilibrium
mas : milli-arcsecond
MB : Main beam
MCP : Monte Carlo programme
MLR : Mass-loss rate
MS : Main sequence
NIR : Near-infrared
NOEMA : Northern Extended Millimeter Array
NRAO : National Radio Astronomy Observatory
PAH : Polycyclic aromatic hydrocarbon
PN : Planetary nebula
pp : proton-proton
PSF : Point spread function
PWV : Precipitable water vapor
RGB : Red giant branch
RML : Regularized Maximum Likelihood
RT : Radiative transfer

SD : Single-dish
SDU : Second dredge-up
SED : Spectral energy distribution
SEST : Swedish-ESO Submillimeter Telescope
SIS : Superconductor-insulator-superconductor
SKA : Square Kilometre Array
SMA : Submillimeter Array
SN : Supernova
SPHERE : Spectro-Polarimetric High-contrast Exoplanet Research
SR : Semi-regular
SSB : Single side band
SWS : Short-wavelength spectrometer
TDU : Third dredge-up
TP : Thermal pulse
TP-AGB : Thermally pulsing asymptotic giant branch
UDfA : UMIST Database for astrochemistry
VLT : Very Large Telescope
VLTI : Very Large Telescope Interferometer
VLTP : Very Late Thermal Pulse
WD : White dwarf
WSU : Wideband Sensitivity Upgrade
ZIMPOL : Zurich Imaging Polarimeter
2SB : Dual side band

List of mathematical symbols

k_ν : Absorption coefficient
$\theta_{\rm res}$: Angular resolution
β : Beta particle
χ^2 : Chi-squared
γ_{ul} : Collisional rate coefficient
C_{ul}, C_{lu} : Collisional rates
$R_{\rm c}$: Dust condensation radius
$T_{\rm c}$: Dust condensation temperature
$R_{\rm e}$: e-folding radius
A_{ul}, B_{ul}, B_{lu} : Einstein coefficients
ν_e : Electron neutrino
j_ν : Emission coefficient
$T_{\rm ex}$: Excitation temperature
$v_{\rm exp}$: Expansion velocity
$f_{\rm X}$: Fractional abundance
ν : Frequency
γ : Gamma ray
$T_{\rm kin}$: Kinetic temperature
$\eta_{\rm MB}$: Main beam efficiency

$\dot{M}$: Mass loss rate
τ_ν : Optical depth
f_0 : Peak abundance
$R_{1/2}$: Photodissociation radius
B_ν : Planck function
h : Planck's constant
e^+ : Positron
$Z_{\rm rot}$: Rotational partition function
$T_{\rm rot}$: Rotational temperature
σ : Sigma (RMS noise / Sensitivity)
$L_\odot$: Solar luminosity
$M_\odot$: Solar mass
$R_\odot$: Solar radius
Ω : Solid angle
S_ν : Source function
I_ν : Spectral intensity
$\phi(\nu)$: Spectral line profile
g_u, g_l : Statistical weights
$M_\star$: Stellar mass
$v_{\rm sys}$: Systemic velocity
$N_{\rm tot}$: Total column density
λ : Wavelength

Contents

List of Figures

List of Tables

Outline of the thesis

This thesis, titled *Charting Circumstellar Chemistry of Carbon-rich AGB Stars*, provides the necessary astrophysical and chemical background, both theoretical and observational, for the research work presented in the three appended papers. Papers I, II, and III form a series of publications, which are together structured to approach the question of carbon-chemistry in AGB CSEs using multiple tools, including observations and radiative transfer analysis, and to a smaller extent, chemical modelling.

Chapter 1 offers a general introduction to stars and stellar evolution, while Chapter 2 delves into asymptotic giant branch (AGB) stars specifically. Their physical structure and evolution are discussed, and the mass loss process leading to the formation of the circumstellar envelope (CSE) is explained. The scientific relevance of the study of AGB stars is also explored, in the context of their contribution to nucleosynthesis and galactic chemical replenishment.

In Chapter 3, the physics of molecular transitions and emission line spectra is outlined, and their capacity as excellent diagnostic tools to explore the physical conditions and chemical evolution of astronomical sources including AGB CSEs is looked into. The various types of molecular transitions, including electronic, vibrational, and rotational transitions are explained, along with processes like ro-vibrational transitions and infrared pumping. The benefits offered by unbiased spectral surveys of molecular line emission are laid out.

Chapter 4 explores the chemistry in the circumstellar envelopes of AGB stars. The chemical classification of AGB stars, and the various processes influencing cir-

cumstellar chemistry are discussed. This chapter briefly summarises the existing knowledge on the chemistry of carbon-rich CSEs, based on observations and models available in the literature. The context of, and need for this particular project are then delineated by situating the goals of the project within the context of our current understanding of these objects.

Observational techniques and instrumentation used to obtain the data used in this project are described in Chapter 5. The chapter describes both single-dish and interferometric observations, and gives an overview of the technique of radio interferometry. The calibration and data reduction methods employed are briefly discussed. The specific telescopes used to obtain the data used in this work are also introduced, including ALMA, APEX, and *Herschel*/HIFI.

Chapter 6 introduces the essential theory and techniques of radiative transfer (RT) modelling, a key method to derive the physical properties of the emitting medium using the observed emission. The RT equations are first described, followed by the physical model of the circumstellar envelope adopted in this work. This is followed by a description of dust RT modelling, which fits the observed spectral energy distributions (SEDs) of the stars, to determine the stellar and dust properties. Gas RT modelling, of both the CO and other molecular line emission is then discussed. We use CO RT modelling to constrain the gas properties including temperature and density in the CSE, whereas RT modelling of other molecular species is aimed at deriving their fractional abundances. An overview of the various molecular excitation mechanisms, and the differences between local thermodynamic equilibrium (LTE) and non-LTE scenarios is also presented. The advantage of using both spatial and excitation information simultaneously to constrain RT models is briefly discussed.

Chapter 7 gives a brief overview of the chemical modelling, an important astrochemical tool to study the evolution and complexity of the molecular chemistry in astrophysical sources. An overview of the techniques and methods of chemical modelling in general, and the current state of such modelling as applied specifically to AGB CSEs are discussed, and various chemical models which account for different physical and chemical phenomena relevant to circumstellar envelopes are touched upon. Reaction networks, or databases containing large arrays of chemical reactions and reaction rates, which are key inputs to chemical models, are also briefly introduced along with a few state-of-the-art examples.

Chapter 8 summarises the three appended papers, highlighting the aims, methodology, main results and conclusions of the respective works. Finally, Chapter 9 presents the prospects and outlook for follow-up research.

1

Introduction

"The stars are the landmarks of the universe."

– John Herschel

1.1 Stars

Stars are some of the most fascinating objects in the universe, from the perspective of both fundamental physics and human culture. The sparkling dots in the night sky have inspired emotions of awe, wonder, and curiosity in humans across the globe, from time immemorial. They have stimulated poetry and romance, fostered fateful superstitions, and have been the subject of countless myths and legends across civilisations. Societies from all parts of the world gave birth to great folklore and beautiful stories by ascribing familiar shapes and patterns to groups of stars, a practice we have joyfully kept alive to date. At the same time, stars have also been objects of great scientific relevance and intensive study for centuries, and have played a crucial role in time reckoning, and in the development of agriculture, navigation, and much more. The history of the study of stars is thus the history of the progress of mankind, from

the hunter-gatherer to the modern human.

It is the energy from our star, the Sun, that is responsible for the sustenance of most life on Earth. Stars are responsible for the production of all elements heavier than lithium, and a large part of the radiation in the universe. They are also the drivers of the physical and chemical evolution of galaxies and thereby the universe itself. Inevitably, research on the formation, structure, and evolution of stars plays a central role in the continuous development of modern-day astronomy and astrophysics, and is pivotal to understanding our origin and place in the universe.

There are hundreds of billions of stars in our galaxy, the Milky Way, itself. Most of them, including our Sun, are of relatively low or intermediate masses, ranging from around 0.8 to 8 $M_{\odot}$. Over billions of years, these stars will eventually evolve into a phase called the *asymptotic giant branch* (AGB). AGB stars are the sites of production of a large variety of elements, including carbon and oxygen which are crucial for the origin and maintenance of life on Earth. Their circumstellar envelopes (see Sect. 2.5) are also rich sites of molecule and dust formation. AGB stars contribute significant amounts of gas and dust to the surrounding interstellar medium (see Sect. 2.6). The study of the physics, chemistry, and evolution of these stars is therefore of great significance in understanding the chemical evolution of the universe. The main focus of this thesis is on the molecular chemistry in the circumstellar envelopes of AGB stars.

1.2 The life cycle of stars

The contents of this section are broadly based on Lattanzio & Wood, in Habing & Olofsson (2003), which serves as the general reference wherever other literature is not explicitly cited.

The evolutionary trajectory of a star is primarily determined by its initial mass, although other factors, including the presence of companion stars, and initial metallicity (abundance of elements heavier than helium), also play major roles. Stars are formed by the fragmentation and collapse of dense molecular clouds. These clouds collapse under the effect of their own gravity, until their central regions reach temperatures and pressures high enough to initiate hydrogen fusion, which is the point we denote as the *birth* of a star. A detailed review of the star formation process and related phenomena is outside the scope of this thesis. The interested reader is referred to Stahler & Palla (2004); McKee & Ostriker (2007); Ward-Thompson & Whitworth

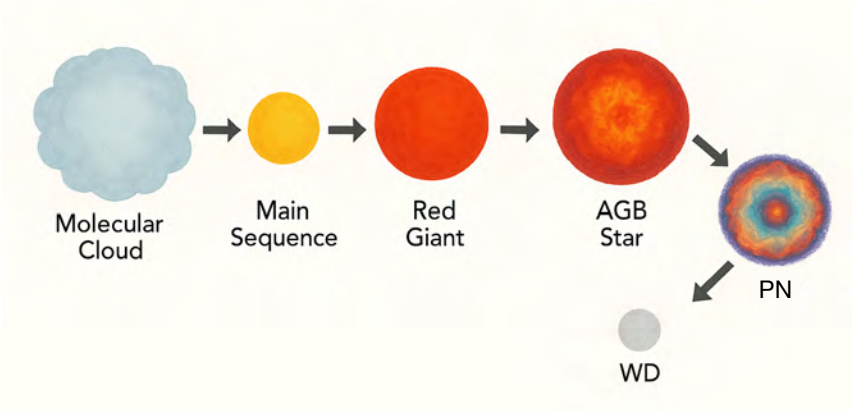

Figure 1.1: The stages in the life cycle of low/intermediate mass ($0.8\ M_\odot < M_\star < 8\ M_\odot$) stars. PN and WD stand for planetary nebula and white dwarf, respectively. The physical sizes of the different phases are not drawn to scale. (credit: OpenAI/DALL.E 2).

(2011); or Bodenheimer (2011).

The main stages in the evolutionary sequence of a single low/intermediate mass ($0.8\ M_\odot < M_\star < 8\ M_\odot$) star is depicted in Fig. 1.1. The various phases in the evolution of a star are named according to the position of the star in each phase in a plot of luminosity vs surface temperature. Such a plot is known as the *Hertzsprung-Russell diagram* (HR diagram, see Fig. 1.2a). The HR diagram is a fundamental tool in the study of stellar evolution, developed in the early 1900s by astronomers Ejnar Hertzsprung and Henry Norris Russell. The path traced by a star in the HR diagram as it evolves is called its *evolutionary track*. The evolutionary tracks of stars of initial masses in the range 1 - 15 $M_\odot$ are shown in Fig. 1.2b, and Fig. 1.3 zooms into the evolutionary track of a 1 $M_\odot$ star, and shows the internal structure of the star during the different phases in its evolution.

The sections below briefly outline the characteristics of the various evolutionary stages of a low/intermediate mass star, starting from its birth. See Kippenhahn & Weigert (1990), and Lamers & Levesque (2017) for detailed descriptions of the physics and phases of stellar evolution.

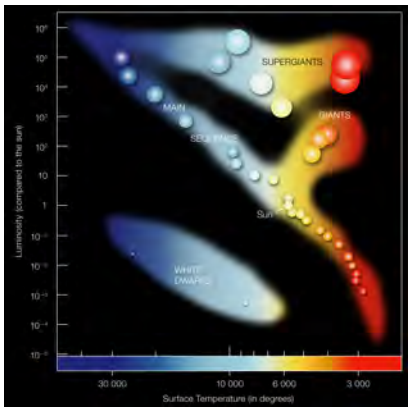

(a) HR diagram

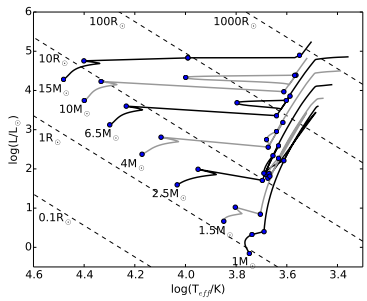

(b) Evolutionary tracks

Figure 1.2: (a) Schematic view of the HR diagram, showing the different phases in stellar evolution (credit: ESO). (b) Evolutionary tracks of 1 - 10 $M_\odot$ stars in the HR diagram (credit: Toonen et al. 2016).

1.2.1 Pre-AGB evolution

1.2.1.1 Main sequence

The *main sequence* (MS) phase is the first and longest stage in the evolution of stars, It is the long strip running diagonally across the HR diagram (Fig. 1.2a), from the high luminosity and temperature region at the top-left to the low luminosity, cool region at the bottom right. The time spent by a star in this phase is dependent on its initial mass. While a star of ~0.1 $M_\odot$ takes roughly 10^{12} years (more than the current age of the universe) to complete its MS evolution, a massive star of ~60 $M_\odot$ will only spend 10^6 years in the main sequence.

In this phase, the star releases energy by fusing the hydrogen in its core to helium. The reaction pathway by which this fusion occurs also depends on the birth mass ($M_\star$) of the star. For stars with $M_\star < 1.3\ M_\odot$ (see Salaris & Cassisi 2005), the hydrogen fusion is dominated by the *proton-proton* (pp) chain. The reaction sequence for the pp chain is as follows:

$$\begin{cases} {}^1\mathrm{H} + {}^1\mathrm{H} \longrightarrow {}^2\mathrm{H} + \mathrm{e}^+ + \nu_e \\ {}^2\mathrm{H} + {}^1\mathrm{H} \longrightarrow {}^3\mathrm{He} + \gamma \\ {}^3\mathrm{He} + {}^3\mathrm{He} \longrightarrow {}^4\mathrm{He} + 2\,{}^1\mathrm{H} \end{cases} \tag{1.1}$$

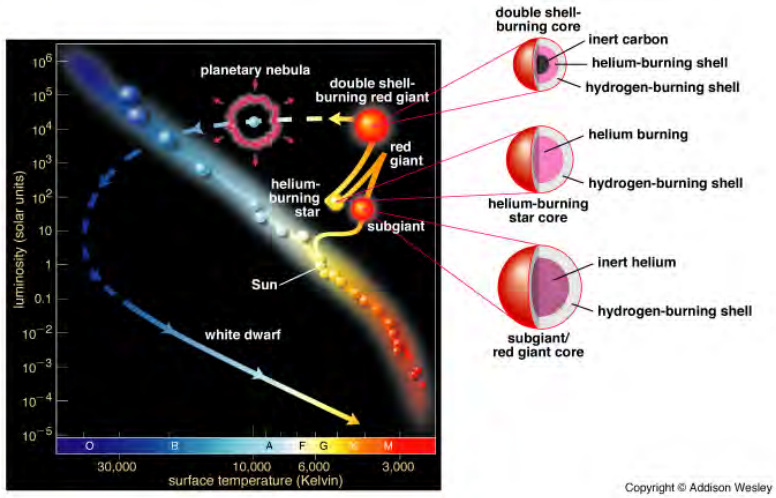

Figure 1.3: The evolutionary track of a 1 $M_\odot$ star in the HR diagram, showing the stellar structure at various phases (credit: Pearson Education).

where e^+ denotes a positron, ν_e is an electron neutrino, and γ is a gamma ray. The formation of ^{4}He as per the third reaction in Eq. 1.1, is referred to as the pp1 chain. Fig. 1.4 shows the schematic view of H-fusion through the pp1 chain. At different temperatures, other proton-proton chains (pp2 and pp3) can be activated, which lead to the production of heavier elements Li and Be in addition to ^{4}He. See LeBlanc (2010) for the details of these less-frequent pathways.

For stars having $M_\star > 1.3\ M_\odot$, the *carbon-nitrogen-oxygen* (CNO) cycle dominates the H-burning. The reactions involved in the major branch of the CNO cycle are:

$$\begin{cases} ^{12}\mathrm{C} + {}^{1}\mathrm{H} \longrightarrow {}^{13}\mathrm{N} + \gamma \\ ^{13}\mathrm{N} \longrightarrow {}^{13}\mathrm{C} + \mathrm{e}^+ + \nu_e \\ ^{13}\mathrm{C} + {}^{1}\mathrm{H} \longrightarrow {}^{14}\mathrm{N} + \gamma \\ ^{14}\mathrm{N} + {}^{1}\mathrm{H} \longrightarrow {}^{15}\mathrm{O} + \gamma \\ ^{15}\mathrm{O} \longrightarrow {}^{15}\mathrm{N} + \mathrm{e}^+ + \nu_e \\ ^{15}\mathrm{N} + {}^{1}\mathrm{H} \longrightarrow {}^{12}\mathrm{C} + {}^{4}He \end{cases} \tag{1.2}$$

[1] https://en.wikipedia.org/wiki/Proton-proton_chain

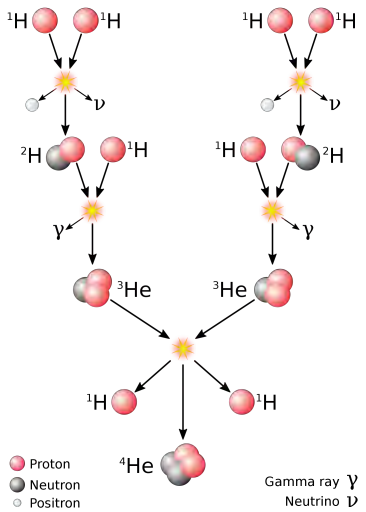

Figure 1.4: Schematic view of the pp1 chain, showing the formation of ^{4}He by H-fusion (credit: *Wikipedia*[1]).

and

$$\begin{cases} ^{15}\mathrm{N} + {}^{1}\mathrm{H} \longrightarrow {}^{16}\mathrm{O} + \gamma \\ ^{16}\mathrm{O} + {}^{1}\mathrm{H} \longrightarrow {}^{17}\mathrm{F} + \gamma \\ ^{17}\mathrm{F} \longrightarrow {}^{17}\mathrm{O} + \mathrm{e}^{+} + \nu_e \\ ^{17}\mathrm{O} + {}^{1}\mathrm{H} \longrightarrow {}^{14}\mathrm{N} + {}^{4}He \end{cases} \tag{1.3}$$

The reactions in Eq. 1.2 constitute the CN cycle, shown schematically in Fig. 1.5. Eq. 1.2 and 1.3 together form the CNO cycle. The CNO cycle produces ^{14}N as a byproduct, and is relevant to the hot bottom burning process (see Sect. 2.3.2.4) in the AGB phase as well, in addition to the core hydrogen fusion in the main sequence phase.

1.2.1.2 Red Giant Branch and Horizontal Branch

Once the star has exhausted the hydrogen in its core by converting it to helium, the core contracts due to the absence of radiation pressure to balance self-gravity. As the core contracts, the outer layers of the star expand, increasing the stellar radius

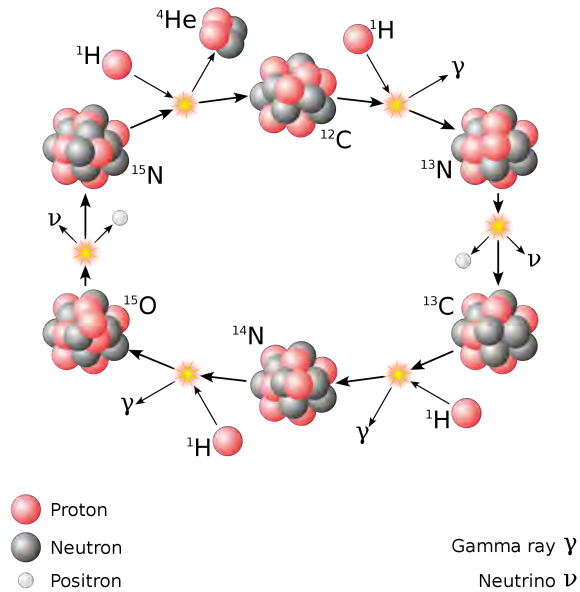

Figure 1.5: Schematic view of the CNO cycle, showing the formation of ^{4}He by H-fusion (credit: *Wikipedia*[2]).

($R_\star$) more than an order of magnitude in a timescale of roughly a million years. A layer of hydrogen in a shell above the core will reach temperatures sufficient enough to initiate hydrogen fusion, which now becomes the source of energy production in the star. The expanded star is now a *red giant*, and this phase in the HR diagram is called the red-giant branch (RGB). This stage is characterised by an inert helium core surrounded by shell burning of hydrogen. As the outer layers expand and cool, the luminosity of the star rises to more than 100 times the solar luminosity. During this phase, large convective motions will move nucleosynthetic products from the internal layers to the surface of the star, in a process known as the *first dredge-up* (see Sect. 2.3.2.3).

The shell-burning of hydrogen continues to produce more and more helium as the star ascends the RGB, increasing the mass and temperature of the helium core. For low-mass ($0.8\ M_\odot < M_\star < 2\ M_\odot$) stars, helium fusion is initiated at the tip of the RGB in a thermal-runaway process called the *helium flash* which rapidly raises the core temperature ($\sim 10^8$ K) and lifts its degeneracy. The star now enters the *horizontal*

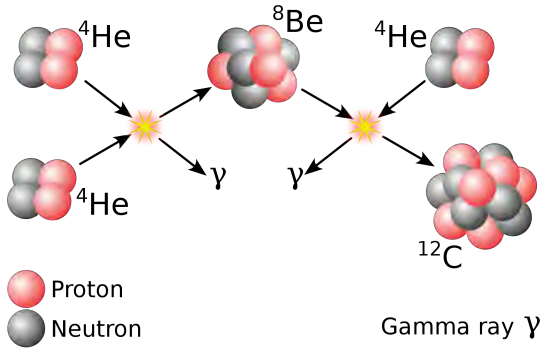

Figure 1.6: Schematic view of the triple-alpha process, showing the formation of ^{12}C by helium fusion (credit: *Wikipedia*[3]).

branch (HB). The HB is characterised by a helium-fusing core surrounded by a shell of hydrogen burning.

Helium burning in the core of HB stars occurs through the *triple-alpha* process, where three helium nuclei are fused to form one carbon nucleus. The reactions involved in the triple-alpha process are given below, and are shown schematically in Fig. 1.6.

$$\begin{cases} {}^4\mathrm{He} + {}^4\mathrm{He} \rightleftharpoons {}^8\mathrm{Be} + \gamma \\ {}^4\mathrm{He} + {}^8\mathrm{Be} \rightarrow {}^{12}\mathrm{C} + \gamma \end{cases} \tag{1.4}$$

1.2.2 The AGB phase

After the exhaustion of the core helium, the stellar core will start to contract again, as it did at the end of the MS phase. For stars with birth masses ($M_\star$) $\lesssim 8\ M_\odot$, this will result in the formation of a degenerate core composed mainly of carbon and oxygen. These stars are not massive enough to attain core temperatures high enough to fuse carbon. They now pass through the *asymptotic giant branch* (AGB) phase, characterised by an inert C-O core, and burn helium and hydrogen in shells outside the core. The evolution along the AGB can be divided into two distinct stages, the

[2] https://en.wikipedia.org/wiki/CNO_cycle

early AGB (E-AGB) and the *thermally-pulsing* AGB (TP-AGB).

1.2.2.1 Early AGB

In this phase, the star has just begun its ascent along the AGB. The energy production in the star at this stage is initially dominated by the shell burning of He above the core. However, the luminosity of the star keeps increasing due to the larger and larger energy being output by the shell-H burning in a region further outside than the He-burning shell (see Sect. 2.3.2). After around 10^5 years, the luminosity of the star will come to be dominated by the H-shell. For stars in the mass range $4 - 8\ M_\odot$, the second dredge-up (see Sect. 2.3.2.3) occurs during this period, and results in the enrichment of the stellar surface with products from the CNO cycle. The early AGB stage is understood to last for approximately 10^6 to 10^7 years (Vassiliadis & Wood 1993).

1.2.2.2 Thermally-pulsing AGB

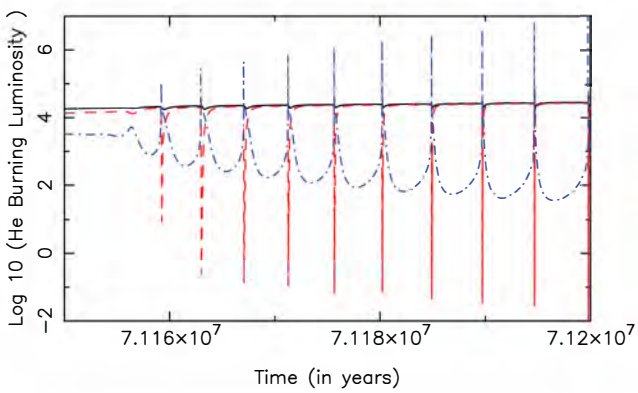

Figure 1.7: Variation in luminosity from the H (blue) and He (red) burning shells, and the total radiated surface luminosity (black) during the TP-AGB phase (credit: Karakas & Lattanzio 2014).

During the shell burning of He and H, the energy production from the He shell will increase to very high (10^6 to 10^7 $L_\odot$) values over a relatively short timescale

[3] https://en.wikipedia.org/wiki/Triple-alpha_process

of around 100 years. This happens due to explosive thermonuclear runaway in the triple-alpha process in the He-shell owing to the continuous accumulation of helium on it from the H-shell burning above. This process is termed the *helium shell flash*. It brings about convectional instabilities in the stellar envelope, and leads to the third dredge-up (TDU, see Sect. 2.3.2.3). These processes together, i.e., the helium shell flash, the instabilities, and the subsequent TDU, are collectively called a *thermal pulse* (TP). AGB stars where thermal pulses occur are said to be in the TP-AGB phase. TP events are repeated on a timescale ($\sim 10^3$-10^5 years) dependent on the stellar mass, as the quiescent He-shell burning is restarted by the repeated accumulation of helium from the H-burning shell. The number and intensity of these events depend on the birth mass and composition of the stars. The time between subsequent thermal pulses is termed the *interpulse* phase ($\sim 10^4$ years, Karakas & Lattanzio 2014). Fig. 1.7 shows the variation in the luminosities of the H and He burning shells, and the total radiated surface luminosity in the TP-AGB phase (Karakas & Lattanzio 2014).

During the AGB phase, several interesting and complex phenomena take place, including processes like hot bottom burning (see Sect. 2.3.2.4), and strong mass loss (Sect. 2.4) which creates chemically rich circumstellar envelopes (CSEs, Sect. 2.5). The structure, evolution, and properties of AGB stars are explored in more detail in Chapter 2.

1.2.3 Post-AGB evolution

At the end of the AGB phase, the convective envelope decreases in mass, and the thermal pulses (Sect. 1.2.2.2) stop. The stars now move towards higher effective temperatures at roughly constant luminosity, and are known as post-AGB stars. The mass loss from the stellar surface ends, and the stellar and circumstellar envelopes are slowly ejected into the interstellar medium (ISM), exposing the inert, luminous C-O core. Fig. 1.8 shows the CSEs of two typical AGB and post-AGB sources mapped in CO $J = 3 - 2$ line emission at their systemic velocities. While the AGB star shows centrally-peaked CO emission, the post-AGB star displays a ring morphology, due to the lack of present-day mass loss.

In a timescale of around 10^4 years, the strong UV radiation from the central star will ionise the ejected material around it, forming objects known as planetary nebulae (PNe). The exposed core will eventually form a white dwarf (WD) star. The locations of the PN and WD stages in the HR diagram are shown in Fig. 1.3. Over the course of billions of years, the WD will cool down to become an invisible black dwarf.

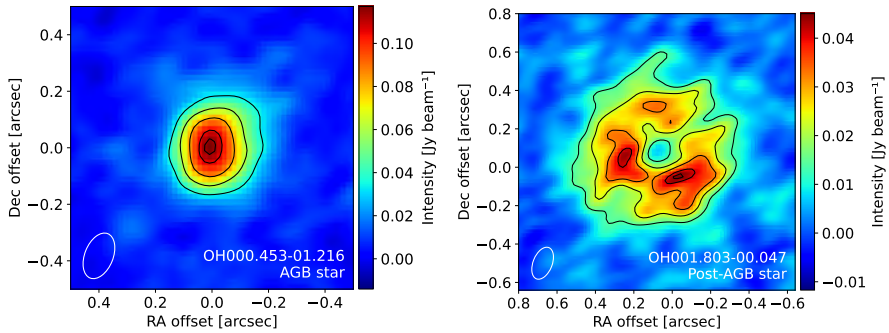

(a) **(b)**

Figure 1.8: CO $J = 3 - 2$ line emission around the systemic velocity, for a typical (a) AGB CSE, and (b) post-AGB CSE, mapped by ALMA (credit: Olofsson et al. in prep.). Both these sources are located in the Galactic bulge, at comparable distances. The white ellipses at the bottom-left corners indicate the synthesised beam sizes of the observations. The black contours are at 0.3, 0.5, 0.7, 0.9, and 0.975 times the peak intensity of the respective images.

It is thought that around 10-25% (e.g. Iben et al. 1983; Blöcker 2001; Herwig 2005) of post-AGB sources experience a final helium shell flash (Iben et al. 1983), also known as a very late thermal pulse (VLTP), where the growing helium layer due to the shell burning of hydrogen reaches the critical mass to initiate helium fusion. As the VLTP is extremely short-lived, only two sources have so far been directly observed undergoing this phenomenon, V 605 Aql and V 4334 Sgr (also known as Sakurai's Object, see Tafoya et al. 2022, 2023, and references therein). Such objects, which thus go through a brief nuclear fusion phase once again during their original post-AGB evolution, are often called born-again stars. After quickly looping through the HR diagram, passing through the helium fusing phase followed by an AGB-like phase, the central star re-enters the WD track and once again becomes hot enough to ionise the surrounding material, which was ejected during the born-again phase, forming a hydrogen-deficient, helium- and carbon-rich PN, often called a born-again PN (e.g. Guerrero et al. 2012), within the old hydrogen-rich extended PN (e.g. Jacoby 1979; Guerrero & Manchado 1996; Toalá et al. 2021). Born-again sources are important in the study of evolved stars as they offer an excellent opportunity to observe multiple stages of late-stage stellar evolution in relatively human timescales. Recent high-resolution sub-mm interferometric studies (e.g. Tafoya et al. 2022, 2023) have

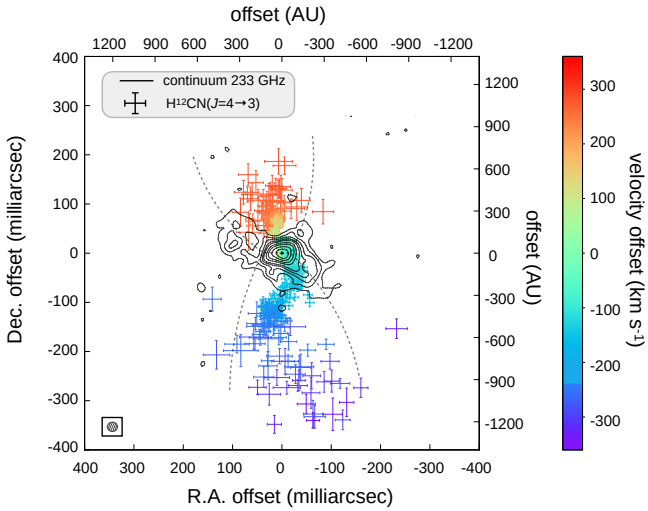

Figure 1.9: ALMA observations of the born-again star Sakurai's object. The black contours denote the 233 GHz continuum emission, displaying a bright compact central component and faint elongated structures along the northeast and southwest directions. The coloured points denote the spatial distribution of the centroid positions of the HCN $J = 4 - 3$ line emission at different velocities, showing a bipolar distribution. The physical distance scales shown assume a distance of 3.5 kpc to the source. (credit: Tafoya et al. 2023).

revealed disc-like structures and bipolar outflows in these rapidly evolving sources (see e.g. Fig. 1.9).

1.3 The evolution of massive stars

Massive stars ($M_\star > 8-10\ M_\odot$) are known as supergiants or hypergiants, due to their very high luminosities (up to $10^6\ L_\odot$, see LeBlanc 2010). After depleting their core hydrogen as MS stars, they go on to fuse helium in their cores, and as supergiants, continue to more cycles of nuclear burning in their cores after the exhaustion of helium, forming heavier and heavier elements up to iron. They finally end their life in extremely bright supernova (SN) explosions, triggered by the sudden implosion of their cores. During a supernova explosion, the outer layers of the star are violently

ejected into the interstellar medium. The core remnant after the explosion may form a neutron star or a black hole, depending on the mass of the star.

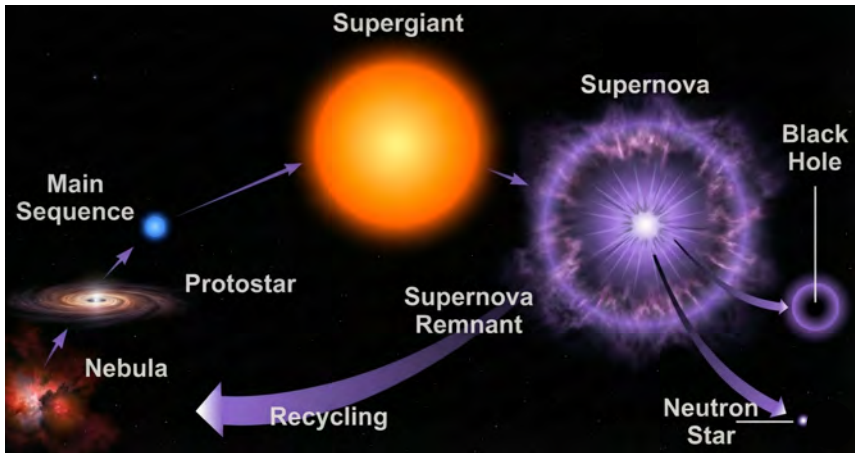

Figure 1.10: The stages in the life cycle of high mass ($M_\star > 8\ M_\odot$) stars. The physical sizes of the different phases are not drawn to scale. (credit: Brooks/Cole Thomson Learning / Google Gemini Pro 3.0).

Fig. 1.10 shows a schematic diagram of the typical evolutionary sequence of a massive star. The details of the steps and processes involved in high-mass stellar evolution are not further discussed here, as the central focus of this work is the AGB. The reader is referred to Kippenhahn & Weigert (1990) or LeBlanc (2010) for an elaborate discussion on the evolution and end stages of such massive stars. The remaining chapters of this thesis will focus exclusively on AGB stars.

2

AGB stars and why to study them

The contents of this chapter are broadly based on Habing & Olofsson (2003) and Herwig (2005), which serve as the general references wherever other literature is not explicitly cited.

2.1 Introduction

The brightest stars in galaxies are often on the AGB, with luminosities rising up to as much as 10^4 $L_\odot$. However, AGB stars are also very cool objects, with surface temperatures around just 2000-3000 K. This is due to the fact that their radii are very large, with the stellar surface extending up to several 100 times the solar radius. These stars have low surface temperatures, around 2000-3000K, making the stellar emission peak in the red, at $\sim 1\mu$m, and significantly fainter in the optical. Some of these stars are even invisible to the naked eye, as they can be efficiently obscured by large amounts of dust formed in their outflows (see Sect. 2.3.3.3 and Sect. 2.5). The AGB is one of the most important phases in the stellar life-cycle. It is the last stage in which the star can release nuclear energy. The evolution to and from the AGB was briefly described in Section 1.2. This chapter focuses on the physical properties of AGB stars and their circumstellar envelopes, and paves the way for a more elaborate

discussion of circumstellar chemistry in Chapter 4.

2.2 Classification of AGB stars

AGB stars are classified mainly based on their atmospheric carbon-oxygen elemental abundance ratio (C/O). This scheme splits AGB stars into three categories or chemical types: *(1)* M-type stars, or oxygen-rich stars (C/O < 1), *(2)* C-type stars or carbon-rich stars (or simply carbon-stars, C/O > 1), and *(3)* S-type, or intermediate stars (C/O $\lessapprox$ 1). This categorisation is very useful in investigating the variations in circumstellar chemistry across AGB CSEs (see Chapter 4).

At the start of the AGB, typical C/O ratios found in stars are around 0.3, meaning all stars start their AGB phase as oxygen-rich. As the star evolves, the C/O ratio changes. For stars with masses greater than $\sim 1.5 M_{\odot}$, newly nucleosynthesised ^{12}C is brought to the surface by dredge-ups (see Sect. 2.3.2.3), increasing the C/O ratio. For stars with $M_{\star} > 4 M_{\odot}$, the effect of this process is reversed when ^{12}C is removed from the surface by hot bottom burning (HBB, see Sect. 2.3.2.4), by reprocessing the ^{12}C via the CNO cycle. Hence, only stars in the mass range $\sim$1.5 - $4 M_{\odot}$ become carbon-rich, or C-type, AGB stars.

In addition to the spectral-type classification, AGB stars are also classified on the basis of their variability (see Sect. 2.3.3.1), into three main groups: *(1)* Mira variables, *(2)* Semi-regular (SR) variables, and *(3)* Irregular variables. Miras are typically well-evolved AGB stars having regular periods and showcasing large amplitudes. The semi-regular variables have smaller amplitudes, and are further divided into two subgroups, SR type-a (SRa), which are still mostly regular, and SR type-b (SRb), with poor regularity. The irregular variables present ill-defined periods at very small amplitudes. Fig. 2.1 shows the V-band light curves of a Mira variable and a semi-regular variable star.

2.3 The structure of AGB stars

The structure of an AGB star can be divided into four major components: *(1)* the core, *(2)* the stellar envelope, *(3)* the stellar atmosphere, and *(4)* the circumstellar envelope (CSE). The physical and chemical processes taking place in these regions are schematically shown in Fig. 2.2. The temperature and density fall drastically as we move to the successive outer layers from the stellar core. The characteristics of these four components are described below.

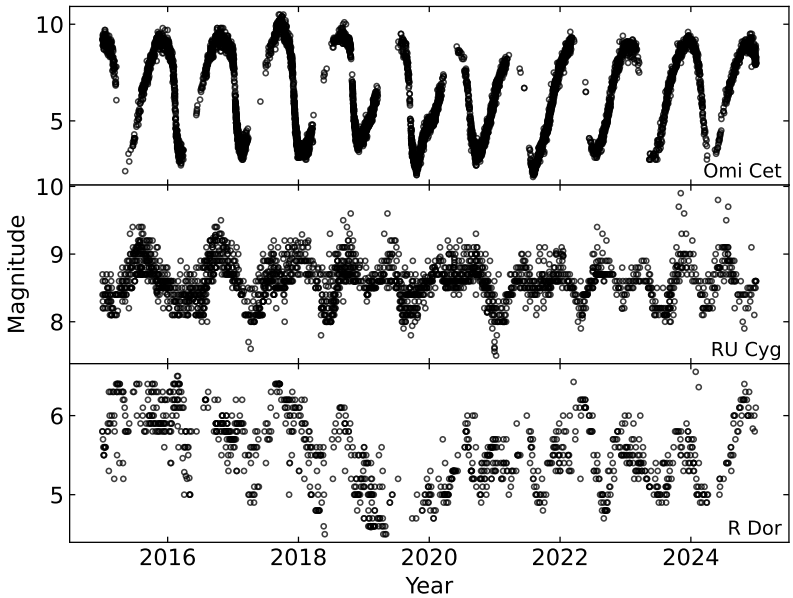

Figure 2.1: Visible/V-band light curves of the Mira variable o Ceti (top), and the semi-regular variables RU Cyg (SRa, middle) and R Dor (SRb, bottom). Photometric data shown in this plot were obtained from the AAVSO[1] database.

2.3.1 The core

The core is the central, innermost region of an AGB star, having only 0.5−1 $M_{\odot}$ in mass, and extending only to less than 0.01% of the total radial size of the star. The core is the hottest and densest part of the star, with temperatures of up to 10^8 K, and densities already comparable to those of white dwarfs. In contrast to the core of a main-sequence star, the AGB core is inert and does not carry out nuclear fusion. It is composed mainly of carbon, oxygen, and degenerate electrons, and is often called an inert C-O core. The composition and properties of the core do not change significantly during the AGB phase, owing to its degeneracy, implying that unlike in the previous evolutionary phases, AGB evolution is no longer controlled exclusively by the evolution of the core (see Sect. 2.4).

[1] https://www.aavso.org

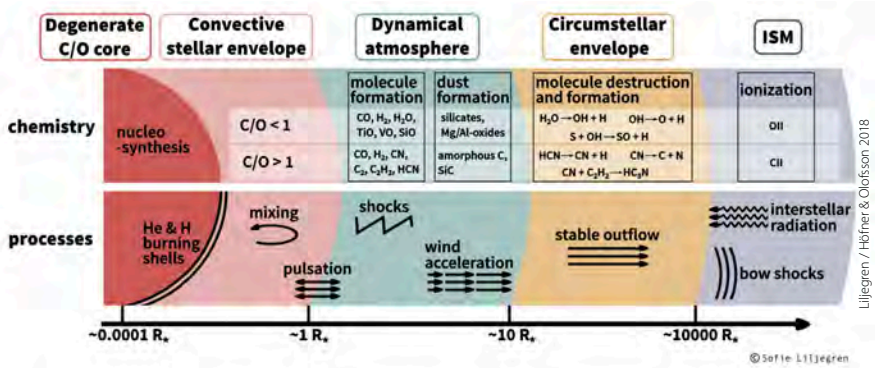

Figure 2.2: A schematic view (not to scale) of the inner layers, atmosphere, and the circumstellar envelope of an AGB star (credit: Höfner & Olofsson 2018).

2.3.2 The stellar envelope

The stellar envelope is the large, hot region surrounding the core, and it contains roughly 50–80% of the stellar mass. Around 99.99% of the size of the star is constituted by the envelope. Fig. 2.3 shows a schematic diagram of the core and envelope structure of an AGB star. The stellar envelope consists of two shells of alternate nuclear burning, an inner one of helium, and an outer one of hydrogen. These shells are separated by an intershell region (Fig. 2.3). The majority of the stellar envelope is comprised of a large convective envelope, lying above the hydrogen-burning shell, and reaching up to the surface of the star. For stars of low envelope masses, a thin radiative shell lies between the H-burning shell and the convective envelope.

2.3.2.1 Nucleosynthesis: fusion

The primary nucleosynthesis in AGB stars occurs in the two shell regions described above. In the outer shell, H is fused to form ^{4}He, principally via the CNO cycle. This influences the composition of the intershell region below it, which is processed by the inner He-burning shell. There, He is burnt via the triple-alpha process to form ^{12}C. See Karakas & Lattanzio (2014) for an elaborate review of the nucleosynthesis and stellar yields of AGB stars.

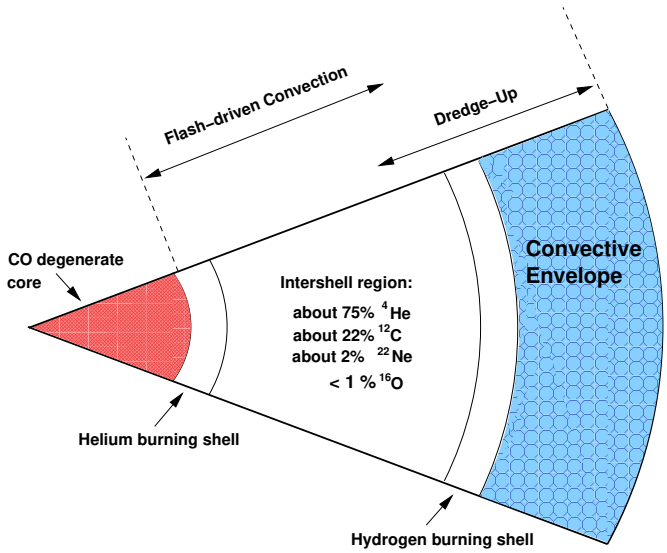

Figure 2.3: Schematic view of the core and stellar envelope of an AGB star (credit: Karakas & Lugaro 2010).

2.3.2.2 Heavy element nucleosynthesis: the *s*-process

The slow neutron-capture process or simply the *s*-process involves, as the name suggests, slow capture of neutrons followed by β^- decay, leading to the formation of successively heavier elements. The *s*-process elements, like lead, technetium and zirconium, are produced in the helium-rich intershell region (Fig. 2.3) between the H and He burning shells. Fig. 2.4 shows an example of *s*-process nucleosynthetic pathways. During the dredge-ups (see Sect. 2.3.2.3), the *s*-process elements are brought from the intershell region to the surface of the star, where they are incorporated into the stellar wind, eventually enriching the ISM.

2.3.2.3 Dredge-ups

During the evolution of a star, there are multiple *dredge-up* processes that bring up the nuclear-burning products from the interior of the star to the surface (Iben 1975; Sugimoto & Nomoto 1975). The first dredge-up (FDU) occurs during the red-giant branch (RGB, see Sect. 1.2.1.2), when the convective envelope penetrates inwards, mixing the products from partial H-burning to the surface. This decreases the surface

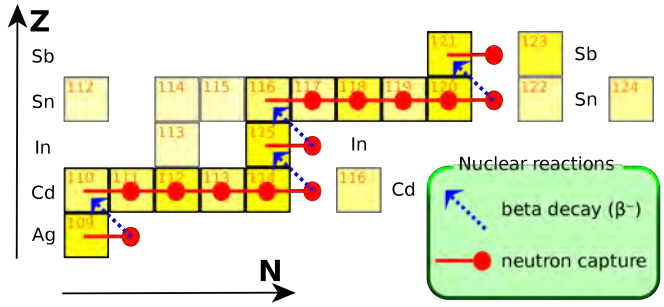

Figure 2.4: Example of a typical *s*-process nucleosynthesis sequence, from Ag to Sb (credit: *Wikipedia*[2]).

abundance of ^{12}C, while increasing those of ^{13}C and ^{14}N.

The second dredge-up (SDU) occurs in stars heavier than 4 $M_{\odot}$, during the early AGB (see Sect. 1.2.2.1) phase, after the exhaustion of core helium burning. This time, the convective envelope brings up material from the old burning layers, which are rich in He and ^{14}N, to the surface layers of the young AGB star. Owing to the increased luminosity following the helium shell flash (see Sect. 1.2.2.2), a third dredge-up (TDU) occurs, due to the convective envelope penetrating what was previously the intershell convection zone. He and ^{12}C are mixed upwards in this process. Repeated TDU events significantly alter the stellar surface abundances of AGB stars, increasing, in particular, the amount of ^{12}C at the surface. Fig. 2.5 shows the abundance ratios of various elements and isotopes at the stellar surface, after the first and final thermal pulses, as a function of initial stellar mass, based on the models by (Karakas & Lugaro 2016). The variations seen between the initial and final TPs are brought about by successive dredge-ups altering the abundance ratios.

2.3.2.4 Hot bottom burning (HBB)

In thermally-pulsing AGB (TP-AGB, see Sect. 1.2.2) stars with masses above ~4 $M_{\odot}$ (at solar metallicity, see Karakas & Lugaro 2016), the thin radiative layer present between the hydrogen-burning shell and the convective envelope can disappear if the bottom of the convective envelope reaches temperatures ($3-8\times10^7$K) high enough to start nuclear burning. Such a situation is called *hot bottom burning* (HBB, Iben 1973; Sackmann et al. 1974). The CNO cycle products produced by HBB are im-

[2] https://en.wikipedia.org/wiki/S-process

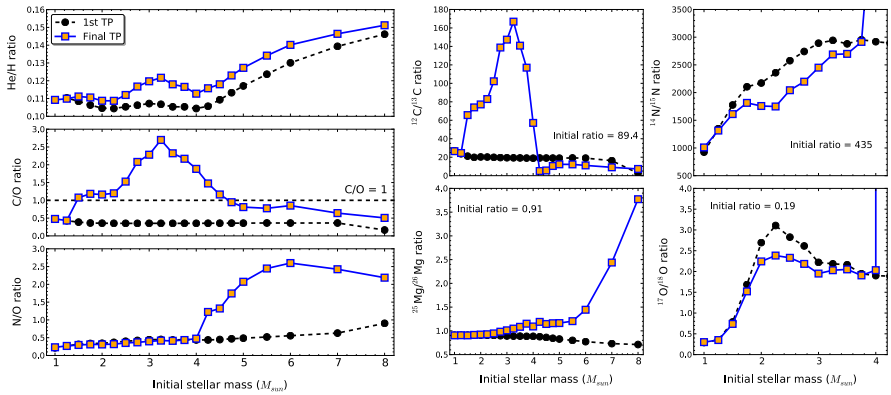

Figure 2.5: Stellar surface abundance ratios of various elements and isotopes, after the first and final thermal pulses, as a function of initial stellar mass for a star of metallicity 0.014 (Karakas & Lugaro 2016).

mediately transported via convection to the surface of the star, leading to an increase in the surface abundance of ^{13}C and ^{14}N, at the cost of a reduced abundance of ^{12}C, counteracting the effect of the third dredge-up (see Sect. 2.3.2.3), and a drastic increase in the ^{17}O/^{18}O isotopic ratio (see Fig. 2.5). For stars which are not massive enough to undergo HBB, the ^{17}O/^{18}O ratio remains constant throughout the whole TP-AGB phase, and is an excellent tracer of the initial stellar mass (De Nutte et al. 2017; Alcolea et al. 2022; Khouri et al. 2025).

2.3.3 The stellar atmosphere

The name *atmosphere* is attributed to the layers immediately above the convective envelope of the AGB star. It is the outermost layer of the star, often viewed as the *surface* of the star, and is the region where the stellar wind originates. The interplay of various complex physical phenomena in the stellar atmosphere is crucial to mass loss and AGB evolution. High-resolution interferometric images of the stellar surface of two AGB stars, showing convective patterns, are shown in Fig. 2.6.

2.3.3.1 Pulsations

Radial pulsations arise in the outer parts of the convective envelope of AGB stars due to opacity effects (e.g. Bowen 1988). These intrinsic pulsations lead to repeated

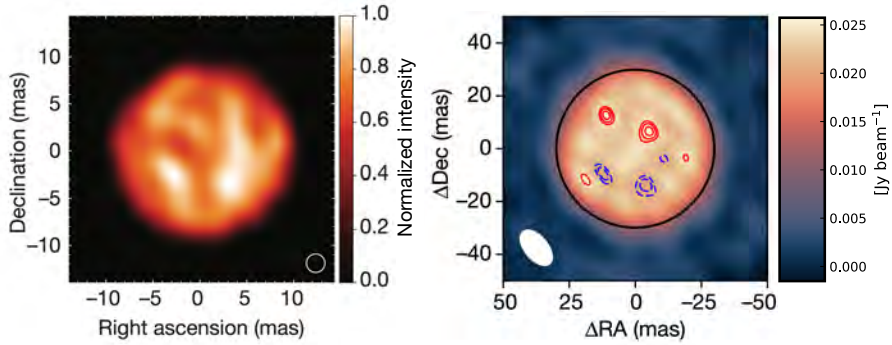

Figure 2.6: *Left*: VLTI-PIONIER near-infrared interferometric images of the surface of the evolved giant star π^1 Gruis at 1.625 μm (Paladini et al. 2018); *Right*: ALMA sub-millimeter interferometric images of the surface of the AGB star R Doradus at 338 GHz (Vlemmings et al. 2024).

contractions and expansions of the photosphere, leading to periodic variations in the stellar brightness and radius. AGB stars are long-period variables (LPVs) with pulsation periods ranging from 10 to around 2000 days. Pulsations produce supersonic shock waves that propagate through the atmosphere of the star, heating up, compressing, and pushing out material (e.g. Cherchneff 2006; Liljegren 2018). This process plays an important role in driving the stellar wind (see Sect. 2.4).

2.3.3.2 The formation of molecules

As the temperatures of the atmospheric layers of AGB stars are ~2000 - 3000 K, they are cool enough to allow the formation of molecules. For carbon-rich (C-type) stars, the main molecules formed are CO, HCN, CN, and C_2H_2, while oxygen-rich (M-type) stars form molecules including CO, H_2O, SiO, and SO_2 in their atmospheres. Convectional mixing and the presence of shocks caused by pulsations complicate the molecule formation process in the atmosphere. The broad emission and absorption bands of the formed molecules can be seen in the stellar spectrum of AGB stars, as shown in Fig. 2.7. C-type stars display molecular bands of carbon-bearing parent species, including HCN, C_2H_2, and C_3, whereas M-type stars show those of oxygen-bearing species like SiO, H_2O, and CO_2.

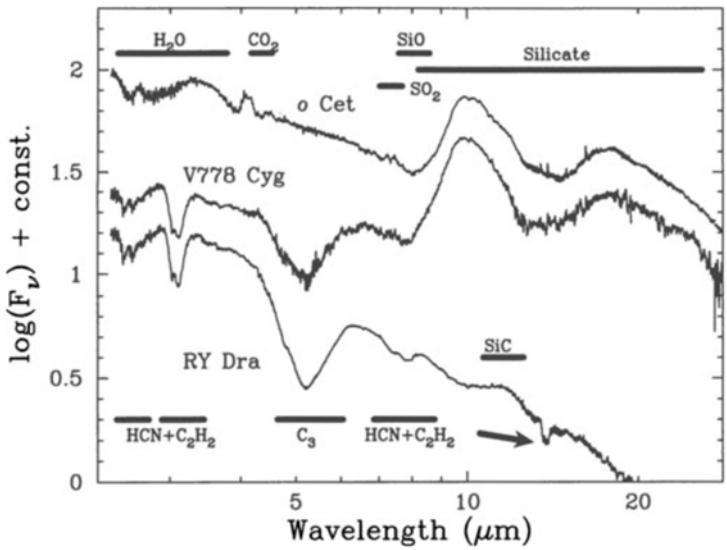

Figure 2.7: ISO short-wavelength spectrometer (SWS) spectra of the M-type star *o* Ceti (upper), and the C-type star RY Dra (lower). The spectrum of the star V778 Cyg (middle) shows features from both C- and O-rich chemistry. The different molecular absorption bands and dust emission features are marked. (Olofsson, in Habing & Olofsson 2003)

2.3.3.3 Dust

Along with the formation of molecules as described above, the cool and dense nature of the outer atmospheric layers of AGB stars also leads to the abundant formation of dust grains (e.g. Millar (Ch. 5), in Habing & Olofsson 2003; Gail & Sedlmayr 2013; Höfner & Olofsson 2018). Refractory material released by stellar nucleosynthesis and convective dredge-up episodes condense in the inner CSE to form solid grains, typically around a distance of 2-3 stellar radii ($R_\star$) from the AGB star (see Höfner & Olofsson 2018, and references therein), where the local temperature drops below condensation thresholds ($\lesssim$ 2000 K). As discussed in Sect. 2.3.3.1, the density of the gas in the atmosphere is temporarily increased by pulsations which levitate its outer layers. This leads to an increase in the efficiency of the dust formation process. The dust condensation sequence is highly sensitive to the C/O ratio in the stellar atmosphere: in oxygen-rich (M-type) stars, silicate grains (e.g.Mg_2SiO_4, $MgSiO_3$)

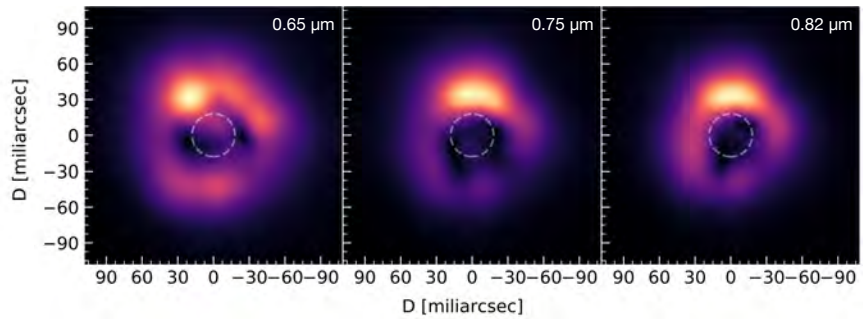

Figure 2.8: VLT SPHERE/ZIMPOL observations of the polarised light around the AGB star W Hya at 0.65, 0.75, and 0.82 μm (Khouri et al. 2020). The dashed circles denote the NIR stellar radius of 18 mas (Woodruff et al. 2009).

dominate, whereas in carbon-rich (C-type) stars, amorphous carbon and SiC grains are prevalent. This can be seen in the dust features that appear in the spectra of the two types of AGB stars, with the SiC ∼11 μm feature being prominent in the spectra of C-type stars, and the silicate features at ∼10 and 18 μm dominating that of M-type stars (see Fig. 2.7).

The nucleation and subsequent grain growth processes are regulated by complex non-equilibrium chemistry, gas densities, pulsation-driven shocks, and the stellar radiation field, all of which influence the efficiency and spatial scales of condensation. The radially increasing expansion velocity of the CSE in the inner region leads to decreasing densities, eventually causing dust formation to stop. From this region onwards, the dust composition does not change in general, until the grains are irradiated by the interstellar radiation field at the outer parts of the CSE.

Polarimetric observations can map the dust around AGB stars, as the scattering of stellar radiation from the surrounding dust grains produces polarised light. Such high-resolution observations, carried out using the ZIMPOL instrument on the VLT, towards the AGB star W Hya are shown in Fig. 2.8. These type of observations can help study the spatial distribution of dust around AGB stars, and constrain their dust condensation radii and the extents of their wind acceleration regions.

Understanding the microphysics of dust nucleation and growth around AGB stars is crucial not only for constraining late-stage stellar evolution but also for tracing the origins of cosmic dust in general, which seeds the formation of new stars, planetary systems, and potentially even prebiotic chemistry. See Gail & Sedlmayr (2013) for

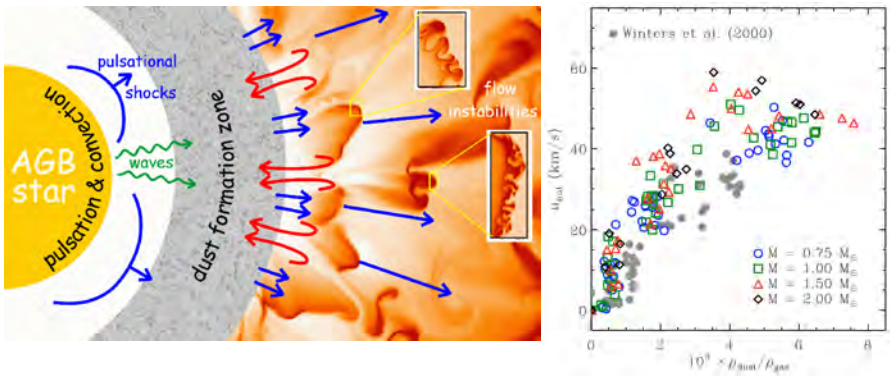

Figure 2.9: *Left*: Schematic diagram of the dust-driven winds of AGB stars (courtesy: Peter Woitke); *Right*: Wind speed as a function of dust-to-gas ratio (Winters et al. 2000; Mattsson et al. 2010).

an in-depth study of dust formation and properties in AGB stars.

2.4 Dust-driven mass loss

AGB stars display heavy mass loss from the stellar surface into the surrounding ISM. The mass-loss rates of AGB stars are typically in the range $10^{-8} - 10^{-4}\ M_{\odot}\ \mathrm{yr}^{-1}$. The very high mass loss from the stellar surface outweighs the minor growth of the core that occurs as a consequence of the fusion processes ongoing in the shells. It is the mass loss that hence drives the onward evolution of AGB stars.

Outward motion of the top layers of the stellar atmosphere due to pulsations can not be the sole cause of the wind, as this process alone is not powerful enough to make these layers attain escape velocity (Wood 1979). The currently accepted formalism of the origin of AGB mass loss is the *dust-driven wind* model (e.g. Sedlmayr & Dominik 1995). In this scheme, dust formation occurs in the pulsation-levitated, shocked outer layers of the atmosphere (see Fig. 2.9). These dust grains are accelerated by the radiation pressure as they absorb and scatter photons from the central star. They then collide with and transfer momentum to the gas particles around them. Such dust-gas collisions create an outflow of gas and dust that we call the stellar wind. Fig. 2.9 shows that the wind velocity steadily increases with increasing dust-to-gas ratio (Winters et al. 2000; Mattsson et al. 2010), a strong indication that the

wind arises due to the momentum transfer from radiation to the gas via dust grains.

The study of the causes and mechanisms of mass loss, and its dependence on fundamental stellar parameters, is crucial to understanding the evolution of AGB stars (e.g. Willson 2000). Numerical simulations like DARWIN (Dynamical Atmospheres and Radiation-driven Wind models with Implicit Numerics, Höfner et al. 2016) are being used extensively to study these phenomena further.

2.5 The circumstellar envelope

The circumstellar envelope (CSE) is the extended, tenuous, chemically rich environment surrounding the AGB star, formed by the extensive mass loss described above. The CSE can be divided into three regions, based on the variation in physical properties present within it (see Fig. 4.1). First, the *inner wind* is the region extending from the atmosphere to the dust-condensation zone. It presents exponentially falling gradients of temperature and density. Above it is the *intermediate wind* where dust forms and grows. The characteristics of this region are not yet well-understood. The part of the CSE from the radius where the wind has achieved terminal velocity, till it merges into the ISM is termed the *outer wind*. CSEs are rich sites of molecule and dust formation, and complex chemistry. The various chemical processes and pathways taking place in AGB CSEs are discussed in Chapter 4.

2.5.1 A note on complex morphology

The density gradient in the CSE is typically assumed to roughly follow an r^{-2} distribution, though discrete variations are routinely observed (e.g. Agúndez et al. 2017; Velilla Prieto et al. 2019; Kim et al. 2015b, and Paper I), possibly induced by the presence of binary companions. Observed complex circumstellar morphology includes density enhancements such as arcs and shells, as seen in IRC +10 216 and II Lup (Cernicharo et al. 2015; Agúndez et al. 2017; Lykou et al. 2018, and Paper I), to spiral structures as observed in stars like CIT 6 and LL Peg (Kim et al. 2015b, 2017). Fig. 2.10 shows the multi-shell density enhancements seen in molecular emission towards II Lup by ALMA, and the asymmetric spiral seen in the CSE of the carbon-star CIT 6 in interferometric CO and HC_3N observations. Hydrodynamical simulations (e.g. Kim & Taam 2012) of the effects of stellar/sub-stellar binary companions on the AGB wind have shown that such large-scale arcs and spiral density patterns can be created by the existence of a companion close to the mass-losing AGB star.

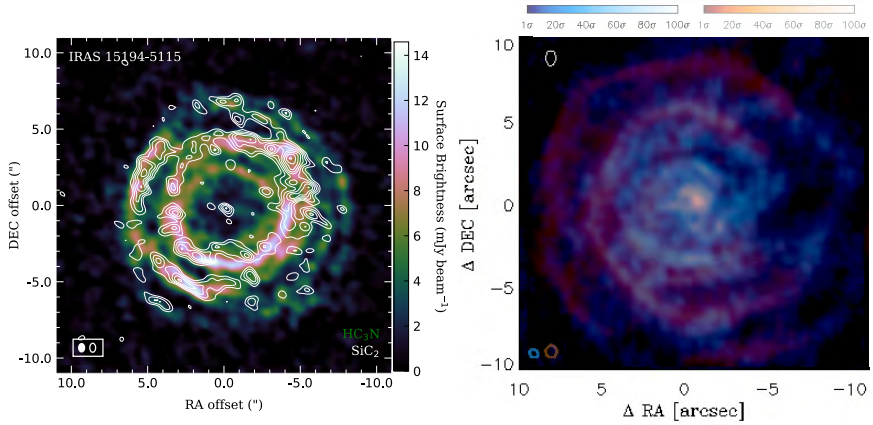

Figure 2.10: *Left*: Complex substructure in the CSE of the carbon-star II Lup, as observed in molecular line emission with ALMA (Paper I). *Right*: The asymmetric spiral structure in the CSE of the CIT 6. CO $J = 2\text{˜}1$ line emission, observed with the SMA, is shown in blue, and that of HC_3N $J = 4\text{˜}3$, observed with the VLA, is given in red (Kim et al. 2015b; Claussen et al. 2011).

It is to be noted that despite the presence of such local enhancements in the gas density, 1D radiative transfer models (see Chapter 6) of circumstellar molecular line emission, which usually employ smooth density and temperature gradients across the CSE, generally perform reasonably well in fitting the observed line spectra and constraining gas properties and molecular abundances (see e.g. Agúndez et al. 2012; Massalkhi et al. 2019, 2024; Danilovich et al. 2015, 2018, 2019, Paper II and Paper III). A proper analysis of these morphological structures, including directional asymmetries, warrants 3D radiative transfer modelling.

2.6 Building blocks of the universe

AGB stars play a major role in the universal cycle of matter, by nucleosynthesising heavy elements and releasing them into the ISM of their host galaxies through their stellar winds. They are also responsible for the formation of dust grains. The periodic table of elements is shown in Fig. 2.11, with the different nucleosynthesis sources indicated by different colours. It can be seen that the AGB stars are major contributors of many elements, ranging from carbon and nitrogen, to the *s*-process

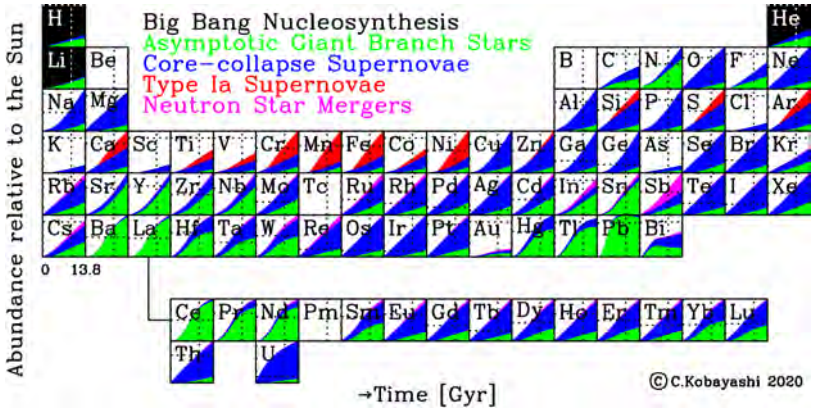

Figure 2.11: The periodic table of elements. Colours indicate different nucleosynthesis sources (credit: Kobayashi et al. 2020).

elements like lead.

The mass loss from AGB stars thus forms the building blocks of the next generation of molecular clouds and stars (see e.g. Tielens 2005). They are also drivers of the chemical evolution of galaxies. Therefore, a thorough characterisation of the physics and chemistry on the AGB is of paramount importance to astrophysics in general.

3

Molecules as diagnostic tools

The contents of this chapter are broadly based on Kwok (2007) and Wilson et al. (2013), which serve as the general references wherever other literature is not explicitly cited.

Molecules, through their spectral lines, are excellent probes of the physical and chemical characteristics of circumstellar and interstellar gas. The intensity of a spectral line traces the amount and physical properties of the emitting matter, and its interactions with the local radiation field, while the spectral line profile sheds light on its kinematics, and also reveals important details about optical depth effects. For unresolved sources, the line width, through Doppler broadening, is often a direct measure of how fast the circumstellar material is moving.

The specifics of the molecular chemistry in the circumstellar envelopes of AGB stars will be dealt with in Chapter 4, and the major methods employed to observe line emission will be described in Chapter 5. This chapter offers a summary of the basic characteristics of molecular transitions and emission lines, examining how they are useful in estimating various properties of the emitting material.

3.1 Molecular transitions and line spectra

As is the case for atoms, molecules too have ground states and several excited states, and transitions between them. However, molecules are more complicated structures than atoms, and their Schrödinger equations are, therefore, more complex, and difficult to analyse directly. The *Born-Oppenheimer approximation* (Born & Oppenheimer 1927) offers some simplification, by stating that the nuclear and electronic motion in a molecule can be treated separately, dividing the molecular wave function into a nuclear and an electronic component. Energy levels of a molecule, and consequently the transitions between them, can then be divided into three separate categories, namely *electronic*, *vibrational*, and *rotational*, based on the type of energy level among which they occur. Fig. 3.1 shows a schematic of the arrangement of these three types of energy levels in a molecule. The classification of molecular transitions based on this division is briefly summarised below.

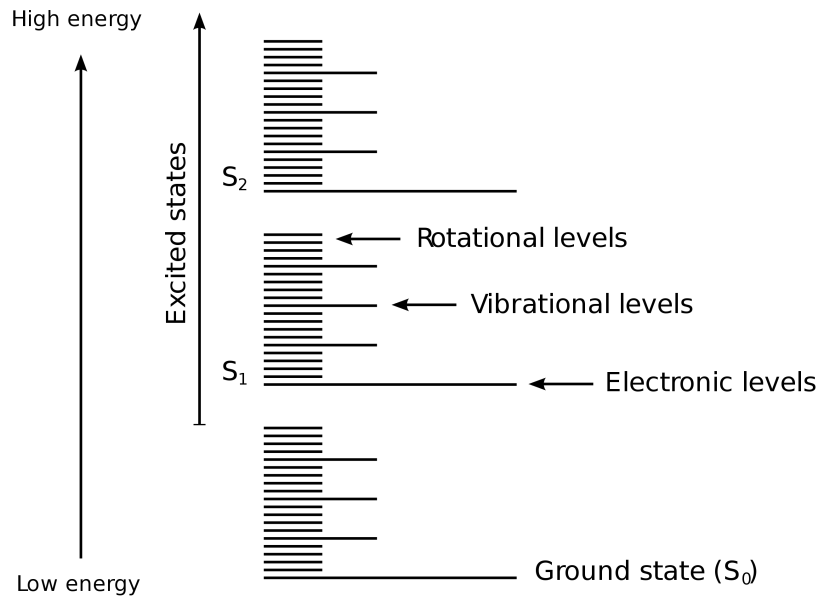

Figure 3.1: A schematic representation of the arrangement of the electronic, vibrational, and rotational energy levels of a molecule (credit: *Wikimedia Commons*[1]).

[1] https://commons.wikimedia.org/wiki/File:Molecular_energy_levels_en.svg

1. **Electronic transitions:** These are transitions caused by the excitation or de-excitation of electrons between the different electronic states or energy levels of the molecule. These energy levels are separated by large energy gaps ($\sim$ a few eV), and hence the spectral lines corresponding to these transitions fall in the visible or UV regions of the electromagnetic spectrum.

2. **Vibrational transitions:** These transitions arise from the oscillations or vibrations of the relative nuclear position with respect to its equilibrium position. There is a range of vibrational states within every electronic state. There can be different types of vibrations, depending on the type of molecule involved. For a diatomic molecule like CO, *stretching*, or the periodic elongation and compression of the bond between the constituent atoms forms the molecular vibration mode. For molecules with more than two atoms, stretching can be *symmetric* or *asymmetric*, and additional vibration modes, e.g. *bending* (periodic change of the angle between bonds), and different combinations of the above, can also exist.
   For an N-atom molecule, there will be $3N$-5 vibration modes if it is linear, and $3N$-6 if non-linear. The typical differences between the energies of adjacent vibrational levels of molecules are in the range of 0.01-0.1 eV, and hence the corresponding spectral lines fall in the infrared part of the electromagnetic spectrum.

3. **Rotational transitions:** These transitions arise from the rotation of the nuclei, as a result of either the torque exerted by the irradiating field on the dipole of the molecule, or collisions. For molecules with no intrinsic dipole moment, like H_2 or C_2H_2, there can be no pure rotational transitions. Molecular rotational transitions have typical energies around $\sim 10^{-3}$ eV, leading to spectral lines in FIR, sub-mm and radio wavelengths. The CO $J = 1-0$ rotational transition at 115 GHz is a commonly studied example. It is also to be noted that rotational transitions are constrained by the electric dipole moment selection rule to have $\Delta J = \pm 1$ due to the symmetries in the rotational wave function of molecules.

The spectral lines of rotational transitions are what we mainly observe using telescopes like ALMA and APEX (see Chapter. 5), and are the primary tools employed in this work to study the physics and chemistry of circumstellar gas. As an exam-

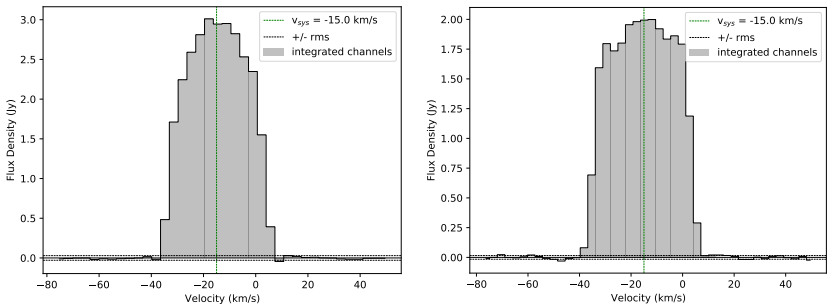

(a) SiO ($J = 2 - 1$) **(b)** HC_3N ($J = 11 - 10$)

Figure 3.2: Spectral lines of the SiO ($J = 2 - 1$, left) and HC_3N ($J = 11 - 10$, right) rotational transitions observed towards IRAS 15194−5115, using ALMA (Paper I)

ple, Fig. 3.2 shows emission lines of SiO and HC_3N observed towards the AGB star IRAS 15194−5115 (Paper I). The molecules studied in this work, and the properties of the circumstellar material derived from the observed spectral lines will be discussed in Chapter 4. Sect. 4.2 of Paper I explains in detail the methods employed to estimate molecular abundances from spectral lines, including *population diagrams* and analytical methods.

In addition to the above, there are also *ro-vibrational* transitions, which involve changes in both the vibrational and rotational state of a molecule. A particularly important mechanism related to ro-vibrational transitions is infrared (IR) pumping. In this process, molecules absorb infrared photons, typically emitted by warm dust grains or stars, exciting them into higher vibrational states ($v > 0$). These excited vibrational levels are usually short-lived and decay into a range of rotational states of the ground vibrational level ($v = 0$). As a result, IR pumping can significantly alter the rotational level populations compared to what would be expected from purely collisional excitation, often leading to enhanced line intensities or population inversions that drive maser action. This mechanism is especially relevant in environments with strong IR radiation fields, such as the envelopes of evolved stars (see Paper II and Paper III).

The energy levels of certain molecules are split into further divisions than those described above, due to the coupling of their spin- and orbital-angular momentum. This process is known as *spin-orbit coupling*, and leads to a splitting of the observed emission lines into components called *fine-structure*. In molecules like CN and C_2H,

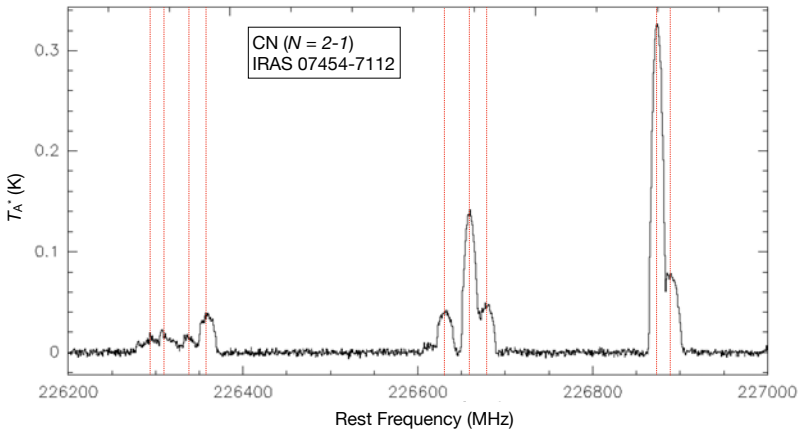

Figure 3.3: Hyperfine components of the CN ($N = 2 - 1$) rotational line towards the C-rich AGB star IRAS 07454−7112, observed with APEX. The red vertical lines denote the frequencies of the major components (Paper I).

interactions between the electric or magnetic moments of the nuclei with electrons lead to further splitting of the energy levels, and consequently the line spectra, known as *hyperfine splitting*. Fig. 3.3 shows the hyperfine components in the line spectrum of the CN ($N = 2-1$) rotational line towards the C-rich AGB star IRAS 07454−7112.

3.2 What can molecules tell us?

Molecular spectra can be analysed to reveal a host of information about the astrophysical environments from which the emission originates (e.g., see Fig. 4.6a). Different molecules can be used to trace different properties of the sources. In AGB CSEs, the emission from carbon monoxide (CO) is often used to derive the physical properties of the gas, such as its mass, temperature, density, and velocity (e.g. De Beck et al. 2012; Danilovich et al. 2015; Olofsson et al. 2022). The observed profiles of such quantities determine the circumstellar physical models underlying our molecular line radiative transfer models (see Paper II). Fig. 3.4 shows the distribution of gas mass-loss rates and expansion velocities, from a large sample of AGB stars in the galactic bulge, derived from CO radiative transfer modelling by Olofsson et al. (2022).

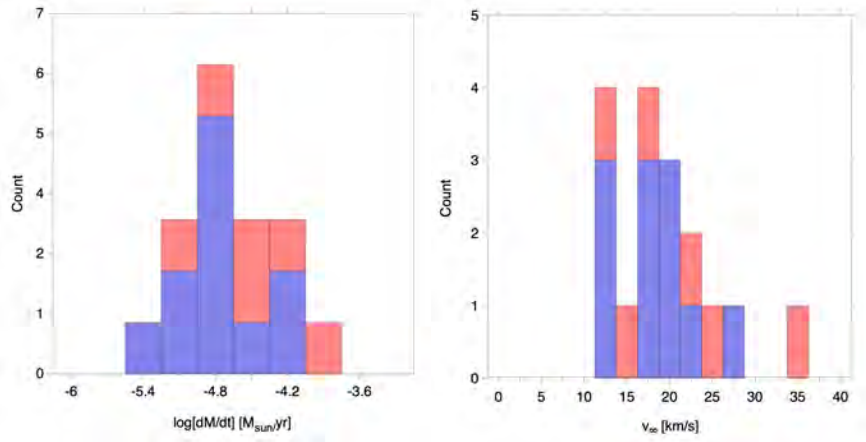

Figure 3.4: Mass-loss rates (left) and expansion velocities (right) of a large sample of AGB stars from the galactic bulge, derived from CO radiative transfer modelling (Olofsson et al. 2022). The blue and red colours denote sources with standard and detached dust envelopes, respectively.

Another example is H_2O, which, with its high dipole moment, serves as a good tracer of the variations in the radiation field, and plays a crucial role in line cooling in the inner CSEs of M-type AGB stars (e.g. Maercker et al. 2016a). Using high spectral-resolution observations, the kinematics and dynamics of the stellar winds, including expansion velocities, asymmetries, and turbulence, can be studied in great detail. The excitation analysis, abundance calculations, and mapping of the emission from other molecules, such as SiO, HCN, and HC_3N, are used to further constrain the physical properties of CSEs, and also to study the chemistry of the gas, as described in Chapter 4.

The more molecules we can detect, study, and compare, the more we can say about the chemical processes and pathways occurring in circumstellar environments. Observations of different isotopologues of molecules can help constrain the isotopic ratios of various elements, like $^{12}C/^{13}C$, which can be used to study the evolutionary history of the star. For example, the three stars studied in Paper I have very different $^{12}C/^{13}C$ ratios. We derived the isotopic ratios of carbon, silicon, and sulphur for the three stars. The estimates match well with the expected AGB values (see Table 8 of Paper I).

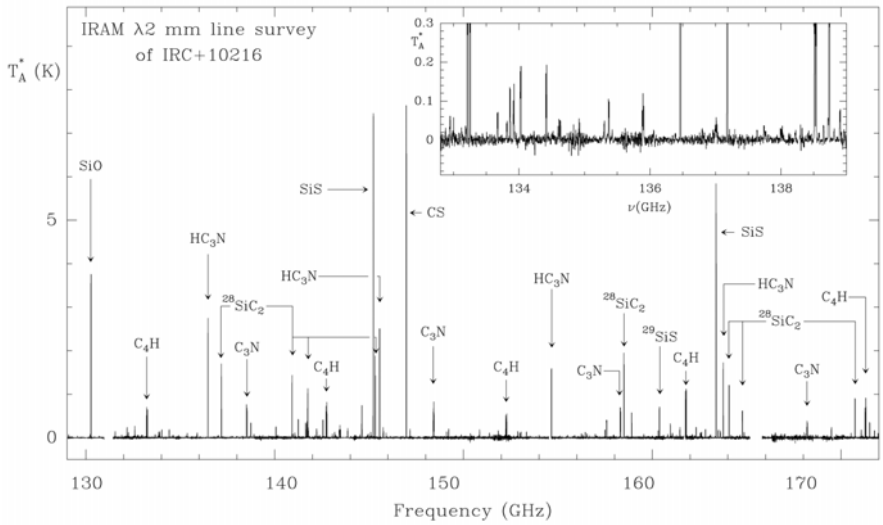

Figure 3.5: The IRAM 30-m spectral survey of the C-rich AGB star IRC +10 216, showing the identified lines (credit: Cernicharo et al. 2000).

3.3 Spectral surveys: how and why

Targeted observations of specific spectral lines, for example those of CO, are used to study specific properties of AGB CSEs, as mentioned in Sect. 3.2. In addition, a vast amount of information about the chemistry of these outflows can be obtained by observing their spectra across wide bandwidths, not targeted specifically at any molecule, but to obtain as many emission lines from various molecules as possible. This type of observation is commonly known as an *unbiased spectral survey*, as it is not biased to any particular molecular species. This is the mode of observation employed in this work.

Unbiased spectral surveys have led to the detection of many new molecules. For example, around half of the total molecules detected to date towards the nearby carbon-star IRC +10 216 were discovered in the course of such a survey of that star by Cernicharo et al. (2000), using the IRAM 30-m telescope. An overview of this survey, showing the large number of detected molecules, is shown in Fig. 3.5. The ALMA band 3 spectral surveys performed in this work, towards three C-rich AGB stars, IRAS 15194−5115, IRAS 15082−4808, and IRAS 07454−7112, are shown in

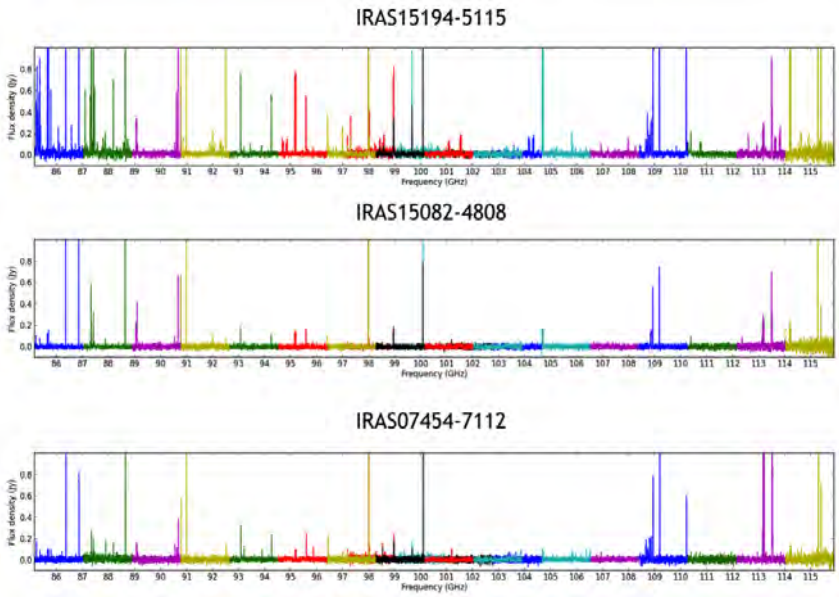

Figure 3.6: Overview of the spectral survey of three C-rich AGB stars, IRAS 15194−5115 (top), IRAS 15082−4808 (middle), and IRAS 07454−7112 (bottom), adapted from Paper I. Colours indicate spectral windows of ALMA observations.

Fig. 3.6. The observations yielded a large number of molecular rotational emission lines, indicating that the CSEs of these stars are also equally chemically diverse as that of IRC +10 216. The survey is presented in detail in Paper I. The upcoming ALMA Wideband Sensitivity Upgrade (WSU[2], see Carpenter et al. 2023; González 2024) will significantly shorten the observing time needed for spectral surveys, by a combination of wider bandwidths, more sensitive receivers, and correlator upgrades, making it possible to conduct such observations much faster.

[2] https://www.almaobservatory.org/en/scientists/alma-2030-wsu/wsu-program/

4

Circumstellar chemistry

As discussed in Chapter 2, AGB stars are highly complex, evolved objects which play a major role in the cosmic chemical cycle. They present extensive mass loss, and their circumstellar envelopes are interesting chemical factories, harbouring numerous molecules and dust species produced through a variety of chemical pathways. This chapter highlights some models and observational results, and the different factors and processes involved therein.

4.1 Molecules around AGB stars

Molecule formation from atomic matter in AGB stars starts in the warm (~3000 K), high-density, outer layers of their atmospheres (Sect. 2.3.3.2). To date, 107 molecular species, and their different isotopologues, have been detected in circumstellar environments (Table 4.1), ranging from two-atom molecules like CO and SiO, to relatively long carbon chains like C_8H, and large cyanopolyynes like HC_7N and $HC_{11}N$. Salts like NaCl and KCl, and refractory heavy metal oxides including AlO and TiO_2 have been detected in AGB CSEs. These species and their spectral lines can be used to estimate various characteristics of circumstellar matter, as described in Chapter 3.

In the work presented in Paper I, we identified a total of 311 emission features

Table 4.1: Molecules detected in circumstellar envelopes, sorted left to right in the increasing order of the number of constituent atoms, indicated at the top of each column. Molecules detected up to 2021 are listed from McGuire (2022). The newer detections included here are from Fonfría et al. (2022); Koelemay & Ziurys (2023); Cabezas et al. (2023); Cernicharo et al. (2023, 2025) and Pardo et al. (2025). See McGuire (2022) and the CDMS catalogue (Müller et al. 2005), for the references to the publications presenting the detection of each of the following species. Tentative detections are labelled with a (?) symbol.

2	3	4	5	6	7	≥8
AlF	C_3	l-C_3H	C_5	C_5H	C_6H	C_7H
AlCl	C_2H	C_3N	C_4H	l-C_4H_2	CH_2CHCN	C_6H_2
C_2	C_2S	C_3O	C_4Si	C_2H_4	CH_3C_2H	CH_3SiH_3
CN	HCN	C_3S	c-C_3H_2	CH_3CN	HC_5N	MgC_6H
CO	HCO^+	C_2H_2	CH_4	C_5N	C_6H^-	HC_7N
CP	H_2O	NH_3	HC_3N	l-HC_4N	MgC_5N	C_8H
SiC	H_2S	H_2CO	HC_2NC	C_5N^-	MgC_5N+	C_8H^-
HCl	HNC	H_2CN	HNC_3	MgC_4H	SiC_6	HC_9N
KCl	MgCN	H_2CS	SiH_4	C_5S	H_2C_5	$HC_{11}N$
NaCl	MgNC	CNCN	CH_4^-	HC_4H		C_6H_6
OH	NaCN	C_3N^-	C_4H^-	SiH_3CN		MgC_6H+
PN	SO_2	PH_3	MgC_3N	MgC_4H+		C_7N^-
SO	SiC_2	HC_2N	SiC_4	HMgCCCN		C_10H^-
SiN	CO_2	HMgNC	MgC_3N+	SiC_5		
SiO	AlNC	MgCCH	NaC_3N	CH_3NC		
SiS	SiNC	l-SiC_3	CH_2NH	H_2C_4		
CS	HCP	c-SiC_3	CH_2CN	CH_3OH (?)		
CN^-	SiCN	HNCS	CH_2CO (?)			
CH	CaNC	HNCO	CH_3Cl (?)			
HF	MgC_2	c-C_3H				
SiP	TiO_2	HOCN (?)				
H_2	C_2P	HCNO (?)				
AlO	KCN	HSCN (?)				
TiO	FeCN	NCCP (?)				
PO	C_2N	HC_2O (?)				
VO	KCN	CH_3 (?)				
FeC	Si_2C	H_3O^+ (?)				
NO	AlOH					
NS	OCS					
FeO (?)	CaC_2					
SO+ (?)	C_2O (?)					
CO+ (?)						
CH+ (?)						
CF+ (?)						

belonging to 49 molecules (including isotopologues) in the ALMA band 3 survey of three C-rich AGB CSEs.

4.2 Diversity among AGB CSEs

Among the different categories (M-S-C, see Sect. 2.2) of AGB stars, the carbon-rich (C-type) stars are the richest in terms of the number and diversity of molecules formed. While the CSEs of M-type stars present relatively small molecules including CO, H_2O, etc., and a few larger molecules like NH_3, the detection of larger molecules like long-chain hydrocarbons (C_nH) and cyanopolyynes (HC_nN) has been done only towards C-type CSEs. Most of these detections have been made towards the nearby, extreme C-rich AGB star IRC +10 216, which is the most studied AGB star to date (see Sect. 4.4.1).

A similar difference can also be seen in the dust species present in M-type and C-type CSEs (e.g. Gail & Sedlmayr 2013; Höfner & Olofsson 2018). In the CSEs of M-type stars, the dominant dust species are silicates. Based on 9.7- and 18-μm solid-state features, several amorphous silicates have been identified in these stars (see Dorschner 2010, and references therein). Further, alumina (Al_2O_3) and crystalline silicate dust have also been detected towards some M-type stars (e.g. Blommaert et al. 2006, 2014). A detailed modelling of the dust formation in oxygen-rich CSEs was presented by Gobrecht et al. (2016a). In contrast, the CSEs of C-type stars are dominated by amorphous carbonaceous dust (e.g. Kraemer et al. 2019; Sloan et al. 1998; Zijlstra et al. 2006), and also show features (~11.3 μm) of SiC (e.g. Ventura et al. 2014). The nature and types of dust formed in AGB stars are thus dependent on the stellar C/O ratio, which is influenced by the evolutionary pathway of the star, as in the occurrence or not of processes like hot bottom burning. Other factors, including metallicity, also play important roles in the formation of dust in AGB stars (e.g. Tosi et al. 2022).

4.3 Chemical stratification

The radial division of AGB CSEs into the inner-, intermediate-, and outer-wind regions was discussed in Sect. 2.5. Fig. 4.1 shows a schematic diagram of the chemical structure of an AGB CSE, outlining the physical and chemical processes taking place in these regions. The molecules formed in the outer layers of the stellar atmosphere are transported outwards in the stellar wind, and involve in various chemical reactions

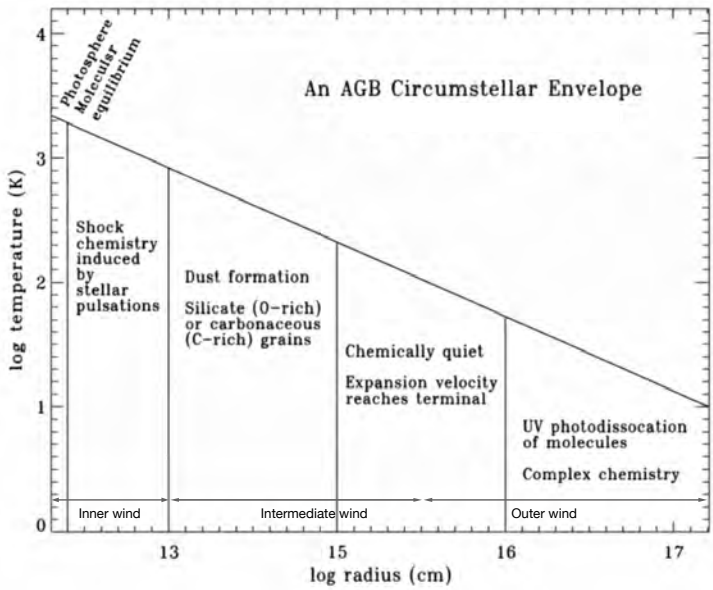

Figure 4.1: Schematic diagram of the chemical structure of an AGB CSE. (adapted from Markwick 2000).

in the CSE, particularly in the outer wind, which is the site of most of the complex chemistry in these sources. The outer wind is characterised by cool gas, expanding at terminal velocity. The molecules in these low-density outermost regions of the CSE are subject to photodissociation by the UV radiation from the interstellar radiation field (ISRF), giving rise to the formation of a multitude of interesting species.

Based on their position in this formation-destruction-formation pathway of circumstellar species, the molecules in AGB CSEs can be categorised into two groups, namely *parent* molecules and *daughter* molecules, as described below.

- **Parent molecules:** These are species which are formed from atomic gas in the inner wind. These include mainly C_2H_2, HCN, CH_4, H_2S, NH_3, CO, CS, SiO, SiS, and N_2 (e.g. Cordiner & Millar 2009; Agúndez et al. 2012). The brightness maps of the line emission from parent molecules present *centrally-peaked* morphologies, i.e., emission that peaks close to the central star (in the inner wind) and extends radially outwards (see Sect. 4.1 of Paper I).

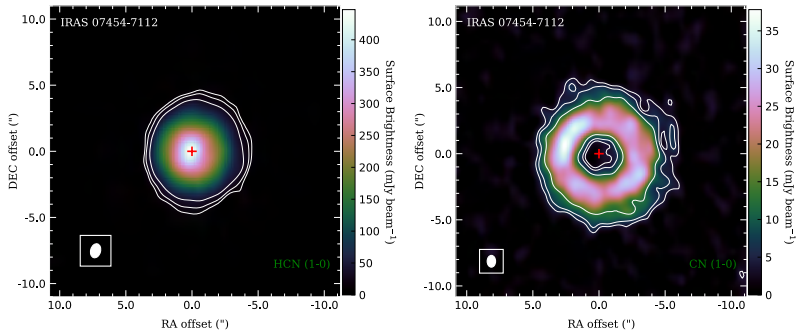

Figure 4.2: Systemic-velocity maps of the $J = 1 - 0$ line emission of HCN (left) and CN (right), showing centrally-peaked and shell emission respectively, for the AGB star AI Vol. Contours are at 3, 5, and 10 σ. The red + sign denotes the continuum peak position (credit: Paper I)

- **Daughter molecules:** These are species formed from the parent molecules, through photodissociation or other chemical pathways. They are found in the outer wind. Most of the species detected in CSEs, including long-chain hydrocarbons and cyanopolyynes are daughter species. These species are distributed in hollow spherical *shells* in the outer CSE, as indicated by their line emission maps which show no emission near the central star, but peak in shells radially farther away (see Sect. 4.1 of Paper I).

The *centrally-peaked* HCN, and the *shell* CN emission morphologies for the carbon-star IRAS 07454−7112 mapped by ALMA are shown in Fig. 4.2. This is consistent with the fact that CN is a photodissociation product of the parent species HCN. The nature of photodissociation of the constituent molecules, i.e., whether they are dissociated in lines or the continuum, and their shielding efficiencies, has a significant influence on the gas-phase chemistry in the CSE. In particular, the photodissociation of CO (e.g. Saberi et al. 2019) is key in precisely determining the extent of circumstellar outflows and their mass-loss rates. In addition to the simple centrally-peaked and shell morphologies, there are also species which can display more complex structures, including having both centrally-peaked and shell emission components, like HC_3N and SiC_2 (see Fig. 2.10).

Fig. 4.3 shows an overview of the radial variation in chemistry for a typical CSE,

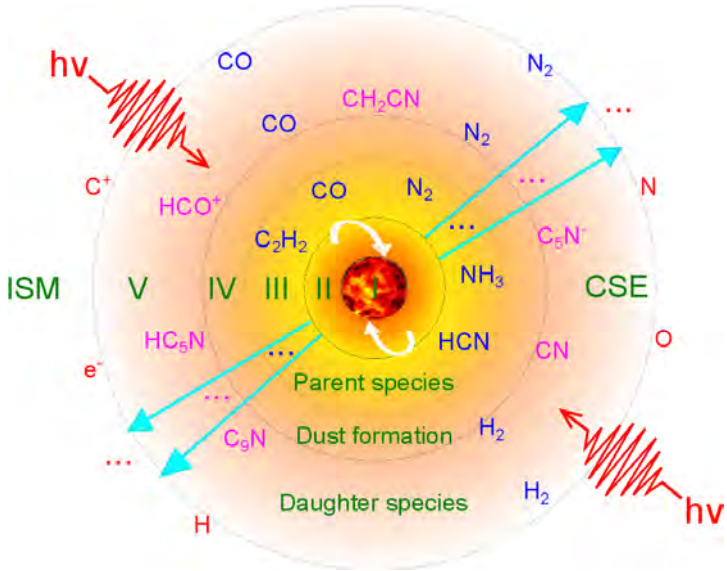

Figure 4.3: Schematic of the chemistry in a circumstellar envelope, showing parent and daughter species. The regions marked in Roman numbers are: (I) degenerate C-O core and He, H burning shells, (II) convective atmosphere, (III) shocked inner wind where parent species are formed, (IV) intermediate wind, (V) outer wind where daughter species are formed primarily by photodissociation, (VI) the ISM. (credit: Li et al. 2014).

schematically depicting the radial arrangement of parent and daughter species. The various chemical pathways in AGB CSEs are subject to intensive study, both through observations and chemical modelling. With the development of modern interferometers like ALMA, VLA, and NOEMA, it is now possible to resolve and map the circumstellar envelopes of AGB stars, and study the chemical structure of these sources in detail (e.g. Dinh-V-Trung & Lim 2008; Velilla Prieto et al. 2015; Maercker et al. 2016b; Agúndez et al. 2017, and Paper I). Single-dish spectral surveys have also significantly advanced our knowledge of circumstellar chemistry (e.g. Cernicharo et al. 2000; De Beck et al. 2012; De Beck & Olofsson 2018, 2020; Velilla Prieto et al. 2017). Such observational studies, along with the advances in our knowledge of chemical reaction networks and rates, have led to the development of detailed chemical models (see Chapter 7) fine-tuned for AGB circumstellar environments (e.g. Brown & Millar 2003; Cordiner & Millar 2009; Agúndez et al. 2017; Van de Sande

et al. 2019, 2020, 2021). To interpret the observations and derive reliable abundance profiles throughout the observed CSEs, one commonly employs radiative transfer modelling (see e.g. Agúndez et al. 2012; De Beck et al. 2012; Danilovich et al. 2016, 2019, 2020, and Paper II and Paper III). The relevant methodologies employed in Paper I, Paper II, and Paper III are described in more detail in chapter 6.

4.4 Carbon chemistry

The high molecular richness of the outflows of C-rich AGB stars is primarily due to the larger versatility of the carbon atom compared to that of oxygen in terms of possible chemical reactions and pathways, owing to its higher valency. The increased ability of carbon to form stable long-chain molecules (catenation), owing to the high bond-strength between C-atoms, also leads to the presence of large, complex molecules in C-rich CSEs. The high carbon abundance also allows the formation of a large number of carbon-bearing species, possibly including polycyclic aromatic hydrocarbons (PAHs, e.g. Cherchneff et al. 1992; Allain et al. 1997), which are not found in M-type CSEs.

4.4.1 The story so far: IRC +10 216

IRC +10 216, also known as CW Leonis, is a nearby (120-190 pc, Groenewegen et al. 2012; Andriantsaralaza et al. 2022), carbon-rich (C/O $>$ 1.5 $\pm$ 0.4, Fonfría et al. 2022) AGB star, with a high mass-loss rate ($\dot{M}$=2-4$\times10^{-5}$ $M_{\odot}$ yr^{-1}, Guélin et al. 2018), making it an easy target for observations. Owing to these properties and the molecular richness in its CSE, the majority of the observational studies and chemical models of carbon-star CSEs so far have focused on this object (e.g. Agúndez et al. 2017; He et al. 2008; Cernicharo et al. 2000; Cordiner & Millar 2009; Guélin et al. 2018; Pardo et al. 2022; Patel et al. 2011; Velilla Prieto et al. 2019; Van de Sande et al. 2019). Hence, IRC +10 216 holds the status of an archetypal carbon-star, the morphology and circumstellar physics and chemistry of which have been extensively observed and modelled.

Line emission from various molecular species in the CSE of IRC +10 216 has been analysed in detail in several studies. Patel et al. (2011) detected a large number of vibrationally-excited rotational lines arising from the inner envelope of IRC +10 216, in an interferometric spectral survey with the Submillimeter Array (SMA). Spectral

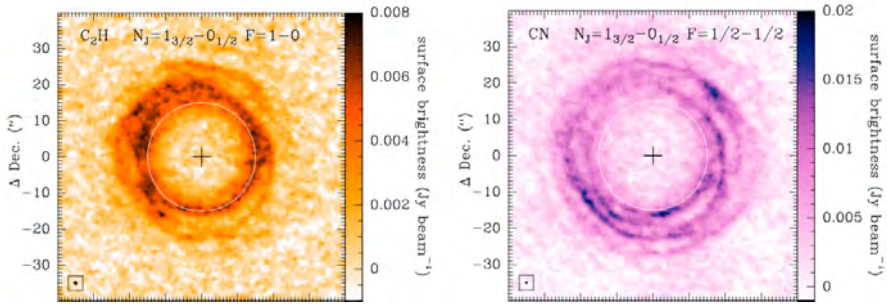

Figure 4.4: Systemic-velocity surface brightness maps of C_2H and CN towards IRC +10 216, observed using ALMA (credit: Agúndez et al. 2017).

surveys using Herschel have led to the detection of many lines from the high-energy rotational transitions of several molecular species, including CO, HCN, CS, and SiC_2 (Cernicharo et al. 2010). Agúndez et al. (2017) used ALMA to map the CSE of IRC +10 216 in various lines, including those of C_2H, C_4H, HC_3N, HC_5N, C_3N, and CN. Fig. 4.4 shows the systemic-velocity surface brightness maps of C_2H and CN towards IRC +10 216 from Agúndez et al. (2017). From such maps, the radial surface brightness profiles of the species can be obtained, which can offer estimates of the sizes of the emitting regions of different molecules. These can help in obtaining accurate abundance estimates, and can also be used to fine-tune chemical models of C-rich CSEs to gain a better understanding of the chemical reactions occurring in these environments.

The chemistry of silicon- and sulphur-bearing species, including CS (see Fig. 4.5), SiO, and SiS, in the CSE of IRC +10 216 has been explored by Velilla Prieto et al. (2015, 2019), and Massalkhi et al. (2019), among others. Similar studies of a sample of other carbon-stars (see Sect. 4.4.2) are presented in this work (see Paper II and Paper III). Radiative transfer modelling has also been extensively employed to estimate circumstellar physical parameters like gas temperature and mass-loss rate, as well as to derive molecular abundances. Fig. 4.6 shows such a model of the circumstellar gas parameters of IRC +10 216, from the radiative transfer models by Agúndez et al. (2012), along with a comparison of the observed and modelled radial surface brightness profiles of different molecular species from Agúndez et al. (2017).

As seen in Fig. 4.4 and Fig. 4.5, the emission maps of different molecules in the CSE of IRC+10 216 trace distinct arc-like structures in addition to a broad shell.

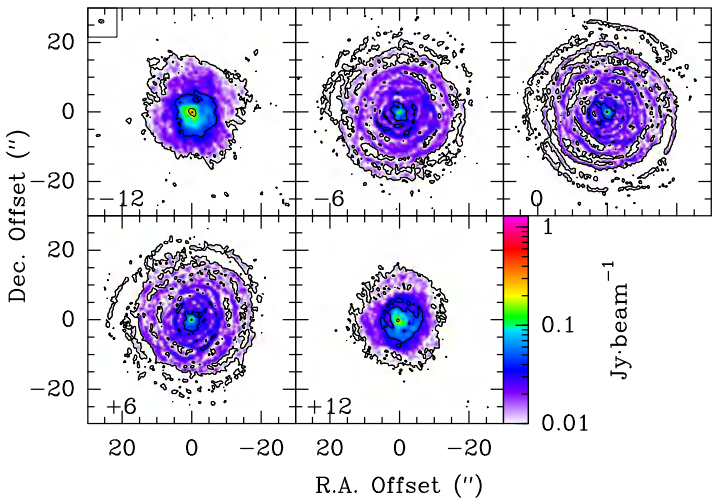

Figure 4.5: Surface brightness channel maps of CS $J = 2 - 1$ line emission towards IRC +10 216, observed using ALMA (credit: Velilla Prieto et al. 2019).

This is also seen towards the stars studied in this work (see Sect. 4.1.1. in Paper I). These are indicative of large-scale radial density enhancements in the CSE, a deviation from the smooth, spherical CSE assumption. Recent chemical models have incorporated the existence of such density-enhanced shells, and hence offer more realistic predictions of the chemical abundances and emission profiles (e.g. Cordiner & Millar 2009). Van de Sande & Millar (2019) further extended the relevant chemical models to include the effects of photo-induced chemistry and clumpiness in the CSE.

While there have been a large number of studies of carbon-star CSEs focused on IRC +10 216 as discussed above, only a handful of studies have looked at other sources in detail. Around 20 carbon-stars were detected in HCN ($J = 1 - 0$) line emission by Olofsson et al. (1990). Bujarrabal et al. (1994) and Olofsson et al. (1998) observed samples of 16 and 22 carbon-stars, respectively, in various molecular lines. Targeted, line-specific observations of larger source samples have also been performed by Schöier et al. (2013); Massalkhi et al. (2019) among others. Nyman et al. (1993) observed IRAS 15194−5115 in the 1.3 mm and 3 mm bands using the Swedish-ESO Submillimetre Telescope (SEST). Line emission from a sample of seven C-rich AGB stars was surveyed in the mm/sub-mm wavelength range by Woods et al. (2003), using the Onsala 20 m telescope and the SEST, while similar

studies were conducted using the Mopra 22 m telescope by Smith et al. (2015). Kim et al. (2015b) interferometrically resolved the CO $J = 2-1$ emission from the CSE of the carbon-star CIT 6, revealing a spiral shell pattern and a nascent bipolar outflow.

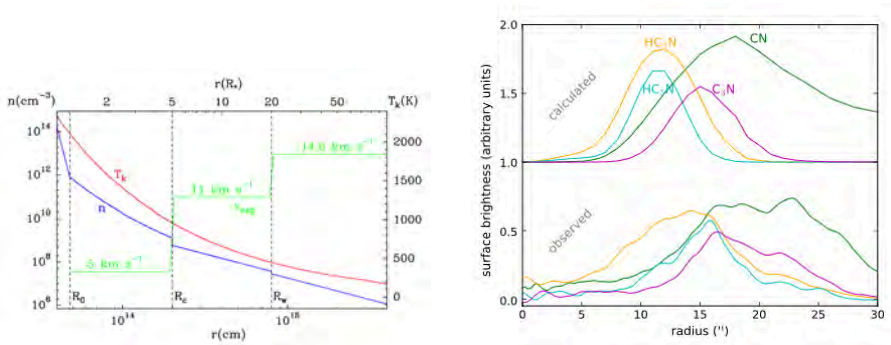

(a) **(b)**

Figure 4.6: **(a)** Model of the number density (n), temperature (T_k), and velocity (v_{exp}) profiles of IRC +10 216. R_0, R_C, and R_W correspond to the radius of the static atmosphere, dust condensation radius, and the end of the dust acceleration region, respectively. (Agúndez et al. 2012). **(b)** Modelled (top) and observed (bottom) radial surface brightness profiles of CN, C_3N, HC_3N, and HC_5N towards IRC +10 216 (Agúndez et al. 2017).

4.4.2 This work

The advent of high angular-resolution telescopes has enabled the mapping of AGB CSEs in previously unattainable detail and sensitivity. However, most of our current knowledge of the circumstellar chemistry of AGB stars, of the C-rich type in particular, is based on observations and models of IRC +10 216 alone, as discussed above. While the few studies of different carbon-stars mentioned above indeed advanced our knowledge of the carbon chemistry in AGB CSEs, they were limited by the fact that most of them were single-dish observations, not intended to spatially resolve the circumstellar emission. Given that the accurate determination of molecular abundances requires knowledge of the sizes of the emitting regions, which are obtainable only by spatially resolving the emission, the lack of spatially resolved observations of multiple C-rich CSEs limit our ability to compare and contrast the chemistry in these objects with one another, and put to test the chemical models optimised for the

Table 4.2: Basic properties of the stars in the sample

Source	Common Name	Distance[(a)] (pc)	MLR[(b)] ($M_\odot$ yr^{-1})	^{12}C/^{13}C[(c)]	$v_{\rm sys}$[(d)] (km/s)	$v_{\rm exp}$[(e)] (km/s)	Period (days)
IRAS 15194−5115	II Lup	690 (+129/−93)	2.2×10^{-5}	6	−15.0	21.5	576[(g,h)]
IRAS 15082−4808	V358 Lup	1050 (±60)	2.2×10^{-5}	35	−3.3	19.5	632[(h)]
IRAS 07454−7112	AI Vol	580 (+70/−56)	8.3×10^{-6}	17	−38.7	13.0	511[(h)]
AFGL 3068	LL Peg	1220 (+70/−60)	4.2×10^{-5}	17	−30.0	14.0	696[(h)]
IRC +10 216	CW Leo	190 (±20)	1.5×10^{-5}	45[(f)]	−26.5[(f)]	14.5[(f)]	630[(i)]

Notes: [(a)]distance estimates from Andriantsaralaza et al. (2022); [(b)]mass-loss rates from Paper II; [(c)]circumstellar ^{12}CO/^{13}CO ratios derived by Woods et al. (2003) from CO radiative transfer modelling; [(d)]systemic velocities of the sources, from Woods et al. (2003); [(e)]expansion velocities of the source CSEs, from Woods et al. (2003); [(f)]The listed ^{12}C/^{13}C ratio, $v_{\rm sys}$, and $v_{\rm exp}$ for IRC +10 216 are from Cernicharo et al. (2000); [(g)] Feast et al. (2003); [(h)] Whitelock et al. (2006) and references therein; [(i)] Menten et al. (2012).

archetype IRC +10 216.

There have been no multi-source studies aimed at resolving the circumstellar emission from carbon-rich AGB CSEs other than IRC +10 216 so far, and this is where the need for the work described in this thesis, based mainly on the ALMA observations presented in Paper I, arises. The high-resolution ALMA observations of three C-rich AGB CSEs, IRAS 15194−5115, IRAS 15082−4808, and IRAS 07454−7112, together with the large range of available single-dish spectral line observations of these sources and AFGL 3068, presented in this work, make it possible to obtain well-constrained estimates of the physical conditions and molecular abundances in their CSEs, enabling comparisons with one another and IRC +10 216. This can bring out similarities and differences in the chemical evolution of AGB CSEs, and also verify whether IRC +10 216 indeed is the archetype carbon-star it is thought to be. The basic properties of the three carbon-stars in our spatially resolved ALMA survey, along with those of AFGL 3068 (included in radiative transfer modelling in Paper II and Paper III) and IRC+10 216 itself, are given in Table 4.2.

5

Observing techniques

5.1 Overview

The stellar continuum from AGB stars peaks in the near-infrared (~0.8 - 3 μm) wavelength range (e.g. Paladini et al. 2018). A major part of the continuum emission from circumstellar dust falls in the mid-infrared (~3 - 15 μm) to sub-mm wavelength range (see e.g. Neugebauer & Leighton 1969; Paladini et al. 2017). The chemistry in AGB CSEs, described in Chapter 4, is best studied by observations of molecular emission lines. The spectral signatures of the rotational transitions (see Sect. 3.1) of the most commonly studied molecular species fall in the *long-wavelength* regime, specifically in the far-infrared (~15 - 200 μm), sub-millimeter, millimeter, and centimeter wavelengths.

The available bandwidth for ground-based observations is severely limited by the Earth's atmosphere, as shown in Fig. 5.1. The amount of precipitable water vapour (PWV) present in the atmosphere affects its transparency. It is measured in millimeters, and is calculated based on combined radiometer measurements and atmospheric models of the telescope sites. PWV is strongly dependent on altitude and local weather. Fig. 5.2 shows the atmospheric transmission at the ALMA array operations site (AOS) at various PWV values.

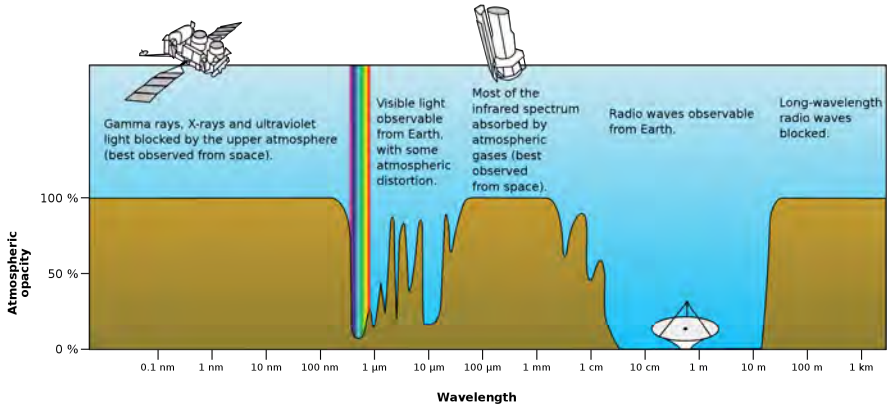

Figure 5.1: Opacity of the Earth's atmosphere across the electromagnetic spectrum (credit: NASA).

All of the radiation in the far-infrared is blocked from reaching the ground due to absorption by the water present in the Earth's atmosphere. To solve this problem, orbiting space telescopes like the Infrared Space Observatory (ISO) and later the Herschel Space Observatory were used to observe the FIR spectra of AGB stars, among other sources, from above the Earth's atmosphere. The recently launched James Webb Space Telescope (JWST) is also opening up possibilities of highly sensitive near- and mid-infrared astronomical observations from space.

In the sub-mm/mm regime, the presence of atmospheric water vapour poses a severe limitation to ground-based observations from low altitudes, and telescopes like the Atacama Pathfinder Experiment (APEX) and the Atacama Large Millimeter/submillimeter Array (ALMA) have been placed at extremely high-altitude sites (~5000 m) in dry, arid, mountainous deserts, to minimize the water column they have to observe through. These observations must still be corrected for the distortion of the signals by the atmosphere, by the use of accurate atmospheric models and calibration.

Early observations of circumstellar emission lines used single-dish telescopes, including the Onsala 20-m telescope, the Swedish-ESO Submillimetre Telescope (SEST), and the IRAM 30-m telescope. More recently, telescopes like APEX have enabled single-dish observations of higher sensitivity at sub-mm/mm wavelengths. However, these telescopes, while providing extremely valuable information about

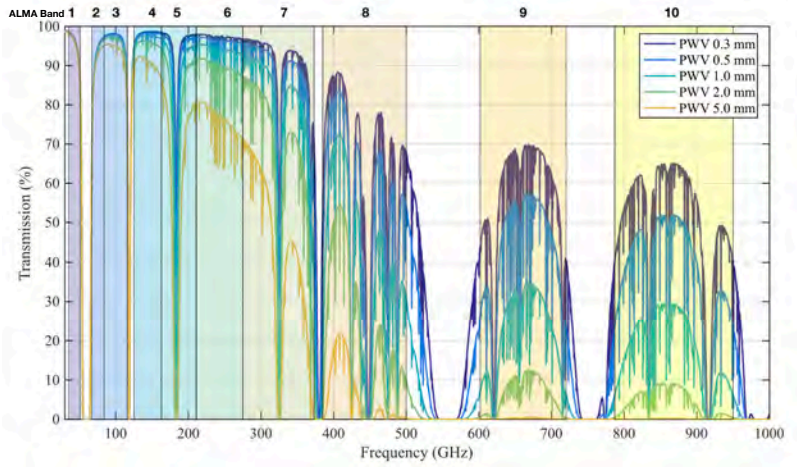

Figure 5.2: Atmospheric transmission at the ALMA site for different PWV values (Carpenter et al. 2020). The frequency ranges of the various ALMA bands are also indicated. Band 1 was made available from 2024 onwards. The Band 2 receivers saw first light in 2023, and are expected to be available for science observations in the coming years.

the sources, could only obtain the spectra of the emission lines, and could not resolve the spatial distribution of the emitting regions. Interferometry using telescopes like ALMA and the Northern Extended Millimeter Array (NOEMA) has made it possible to spatially resolve and map the distribution of the emission, revolutionising the field of sub-mm/mm astronomy. This project makes use of both single-dish and interferometric data observed using APEX, and ALMA, respectively. This chapter is a concise overview of the basic technical and scientific aspects of these observing techniques and telescopes.

5.2 Single-dish observations

A radio or sum-mm/mm telescope consists of an antenna and a receiver, used to capture electromagnetic waves coming from astronomical sources. The emission from astronomical sources is not easily detected, owing to their low intensities, and needs to be amplified. Contemporary single-dish telescopes like APEX employ heterodyne receivers, which are instruments comprised of a mixer, a set of amplifiers,

filters, and finally a spectrometer. The mixer is used to convert the incoming high-frequency signal to a more easily-amplifiable lower frequency signal, by mixing the sky signal of frequency $f_{\rm sky}$) with a signal of frequency $f_{\rm LO}$ generated by the local oscillator (LO). This is done because amplification is much more easily possible for a lower-frequency signal. The mixers used in the receivers of APEX (and ALMA) are superconductor-insulator-superconductor (SIS) mixers, which offer high tunability and low noise in the sub-mm/mm range.

The intermediate frequency ($f_{\rm IF}$) is the frequency at which the incoming signal will be recorded by the spectrometers and is defined as:

$$f_{\rm IF} = |f_{\rm LO} - f_{\rm sky}| \tag{5.1}$$

The IF frequency can only be varied within specific limits for each instrument, which determine the bandwidth of the instrument. The IF signal includes two sidebands, as seen from Eq. 5.1, one on each side of the LO frequency. These sidebands are named the lower sideband (LSB), on the lower end of the LO frequency, and the upper sideband (USB), on its higher end. There are three modes of receiver operation, based on which signal from the respective sidebands is retained or suppressed. Sideband suppression is achieved by the use of selective filters next to the mixer. When only one of the sidebands is retained and the other is suppressed, the receiver is said to work in single sideband (SSB) mode. When both sidebands are retained, but superposed in the output spectrum, the receiver is said to operate in double sideband (DSB) mode. When both sidebands are retained and also separated in the final spectrum, the receiver mode is called sideband separated, or dual sideband (2SB).

The signal in the sideband(s) is then amplified using a cascade of low-noise amplifiers, so that the receiver output has a high signal-to-noise ratio. The spectrometers record the intensity as a function of frequency, in bins of specified width, specified by the frequency resolution. Different spectrometers on the telescope can also process copies of the amplified signal simultaneously, without leading to reduced sensitivity. The intensity of the signal is expressed as an antenna temperature ($T_{\rm A}$). After calibrating for the atmospheric distortion and correcting for instrumental losses, the corrected antenna temperature is denoted by $T_{\rm A}^*$. The calibration process can be done in various ways. To remove the sky background, the *switching* methods usually employed during observations are:

- **Position switching**: repeatedly changing the pointing of the primary mirror between the source (ON) position and a noise-only (OFF) position, at regular intervals.

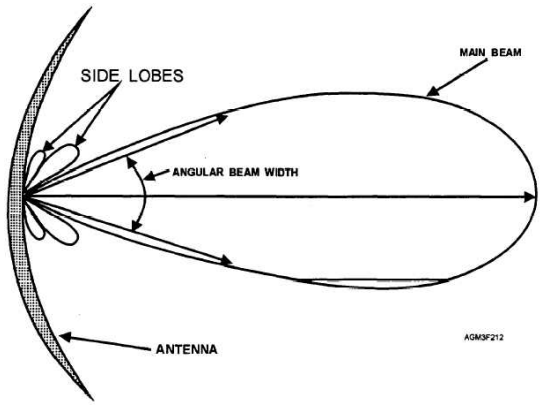

Figure 5.3: Polar plot of an antenna beam pattern, showing the main beam and sidelobes (credit: Argelander-Institut für Astronomie).

- **Beam switching**: repeatedly changing the pointing of the sub-reflector between the source (ON) position and a noise-only (OFF) position, at regular intervals.
- **Frequency switching**: repeatedly changing the LO frequency by a very small amount, at regular intervals. This method is very rarely used for observations of evolved stars.

The *chopper wheel* method, i.e. alternately observing a hot load (of ambient temperature), and then the cold sky, is employed for the flux calibration of sub-mm/mm single-dish telescopes.

As shown in Fig. 5.3, the *beam pattern* of a telescope antenna is characterised by a *main beam* and multiple *sidelobes*, indicating that not all of the power received is in the main beam. To estimate the power received in the main beam only, the main beam efficiency is defined as:

$$\eta_{\mathrm{MB}} = \frac{\Omega_{\mathrm{MB}}}{\Omega_{\mathrm{total}}} \tag{5.2}$$

where Ω_{MB} is the solid angle of the main beam, and Ω_{total} is the total solid angle of the antenna. Using this, we can convert the corrected antenna temperature (T_{A}^{*}) to a main beam temperature (T_{MB}) scale, as:

Figure 5.4: APEX gazing into the cosmos (credit: Babak Tafreshi, ESO)

$$T_{\mathrm{MB}} = \frac{T_{\mathrm{A}}^{*}}{\eta_{\mathrm{MB}}} \tag{5.3}$$

This is the intensity scale mainly used in astrophysical calculations using single-dish data.

5.2.1 The APEX telescope

The Atacama Pathfinder Experiment (APEX[1], Güsten et al. 2006, Fig. 5.4), is a 12-m telescope operating at millimetre and sub-millimetre wavelengths, located at ~5000 m altitude in the Chajnantor plateau in the Chilean Andes, one of the driest places on the planet. It is currently the largest sub-mm/mm telescope in the southern hemisphere, and can observe a range of astronomical sources and phenomena, from nearby stars and nebulae, to galaxies and cold clouds in the distant universe.

APEX hosts several instruments, ranging from large-aperture bolometers (e.g. *ArTéMiS*, Revéret et al. 2014) to heterodyne receivers (e.g. *SEPIA*, Belitsky et al. 2018). APEX was inaugurated in 2005, and is currently operated by the Max Planck Institute for Radio Astronomy (MPIfR) in Bonn, Germany. This project uses data

[1] APEX is a collaboration between the Max Planck Institute for Radio Astronomy (MPIfR Bonn, Germany), the European Southern Observatory (ESO), and the Onsala Space Observatory (OSO), Sweden.

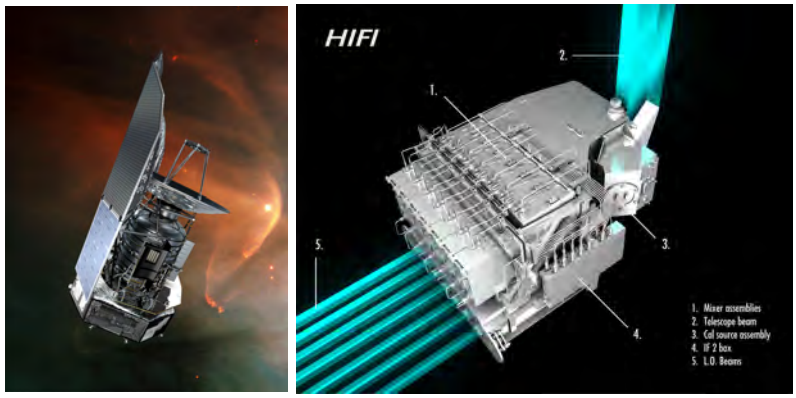

Figure 5.5: Artist's impression of the Herschel space telescope (left) and a schematic diagram of the HIFI instrument (right) (credit: ESA/Caltech/Herschel)

obtained with APEX, observed using the following receivers: SEPIA band 5 (159 - 211 GHz, Belitsky et al. 2018), PI230[2] (200 - 270 GHz), and SHeFI (200 - 270 and 272 - 376 GHz, Vassilev et al. 2008). See Sect. 3.1 of Paper I for a detailed description of the observations.

5.2.2 The HIFI instrument

The Heterodyne Instrument for the Far-Infrared (HIFI, de Graauw et al. 2010, Fig. 5.5) was a spectrometer aboard the European Space Agency's (ESA) Herschel Space Observatory (Pilbratt et al. 2010) launched in 2009, operating in the far-infrared and sub-millimeter wavelength ranges. It contained a set of 7 tuneable heterodyne receivers which covered the frequency ranges 480-1250 GHz and 1410-1910 GHz, and was designed to provide very high spectral resolution over the entire frequency range. The nominal spectral resolution of HIFI is around 1.1 MHz. The instrument was developed by a consortium led by the Space Research Organisation Netherlands (SRON). The Herschel mission was decommissioned in 2013.

This project uses data obtained using the HIFI spectrometer, carried out in spectral scan mode, covering the frequency range 479.5–1121.9 GHz, spanning bands 1a, 1b, 2a, 2b, 3a, 3b, 4a, and 4b, with a velocity resolution of $\sim 0.3 - 0.7$ km s^{-1}. For a

[2]PI230 is a collaboration between the European Southern Observatory (ESO) and the Max-Planck-Institut für Radioastronomie (MPIfR).

detailed description of the observing modes and data processing methods of HIFI, we refer to Roelfsema et al. (2012), Mueller et al. (2014), and Shipman et al. (2017).

5.3 Radio interferometry

The contents of this section are broadly based on Wilson et al. (2013) and Thompson et al. (2017), which serve as the general references wherever other literature is not explicitly cited.

The basic introduction to the theory and practice of interferometry presented in this section is far from complete, and is intended only as a simplistic overview of the bare minimum of its demanding concepts. A more detailed analysis of radio interferometry is outside the scope and intention of this thesis. Extensive literature is available on the topic, that the curious reader may refer to, including but not limited to Born & Wolf (1999); Taylor et al. (1999); Wilson et al. (2013) and Thompson et al. (2017).

Single-dish telescopes, while being very useful observing tools, have several limitations. As mentioned before, the mapping of the spatial distribution of the observed emission is not easily possible using single-dishes. Although they can be used to produce mosaic maps, this is still limited in terms of resolution and sensitivity. The angular resolution of a telescope is related to the wavelength of observation (λ), and the diameter (D) of the telescope, as:

$$\theta_{\rm res} \propto \frac{\lambda}{D} \tag{5.4}$$

This means that, for a given wavelength, the angular resolution is better for a larger telescope. Also, for long-wavelength observations, very large-diameter telescopes are required to achieve the same angular resolution as a smaller telescope has at shorter wavelengths. Even though very large-aperture single-dish telescopes like the Five-hundred-meter Aperture Spherical Telescope (FAST), and the Arecibo observatory have been built, practical constraints make the construction of larger and larger single-dish telescopes impossible, and they also become increasingly less flexible in the ways they can observe, as their aperture size increases. It is to overcome this limitation that the technique of radio interferometry was developed.

Radio interferometers work based on the principle that a resolution of $\theta_{\rm res}$ obtained by a single-dish of diameter D can also be obtained by combining the signal

received by two antennas of smaller diameter, ($d \ll D$, see Fig. 5.7) but separated by a distance D (see Born & Wolf 1999). This means that the angular resolution of an interferometer is limited not by the diameters of the individual antennas, but by the largest separation between two dishes. The separations between the antennas of an interferometer are known as baselines.

This technique can be extended to a multi-antenna system which can produce high-resolution images of the sky by combining independent observations of pairs of antennas spread over the equivalent aperture. This is known as aperture synthesis. The angular resolution of an aperture synthesis interferometer is given by:

$$\theta_{\rm res} = \frac{\lambda}{|\mathbf{b}|} \tag{5.5}$$

where $|\mathbf{b}|$ is the length of the longest baseline. Increasingly finer structures can be resolved by increasing $|\mathbf{b}|$. It is to be noted that the "equivalent aperture" generated by an interferometer, albeit offering high spatial resolution, is not filled, and hence does not offer exactly the same sensitivity as that of the hypothetical single-dish telescope the size of the equivalent aperture. Lack of specific baselines in the array configuration can also lead to structures at various scales being resolved out.

Nevertheless, modern interferometers offer excellent spatial resolution and sensitivity, sufficient to even resolve the photospheres of nearby AGB stars (see Fig. 2.6). Fig. 5.6 presents the resolution and sensitivity of current and planned sub-mm/radio interferometers, including VLA, ALMA, SKA, and the ngVLA, at different frequencies (Bojnordi Arbab et al. 2024), showing that the high imaging sensitivity of the SKA, and the planned high sensitivity and angular resolution of the ngVLA can lead to high-resolution observations of AGB atmospheres across the galaxy at a wide range of frequencies.

5.3.1 Observing with a radio interferometer

A block diagram of a simple two-element interferometer is shown in Fig. 5.7. The two antennas are separated by a baseline separation **b**, and are connected to a correlator which multiplies and time-averages the signals from the two antennas.

When we observe an astrophysical phenomenon happening at location **R** in space, what we are effectively doing is to record the time-varying electric field (**E**(**R**,t)) which propagates to us from that point. We can write the magnitude of this electric field as a sum of Fourier components. The fourier coefficients ($\mathbf{E}_\nu(\mathbf{R})$) thus obtained are complex quantities. However, the propagated components of the electric field at

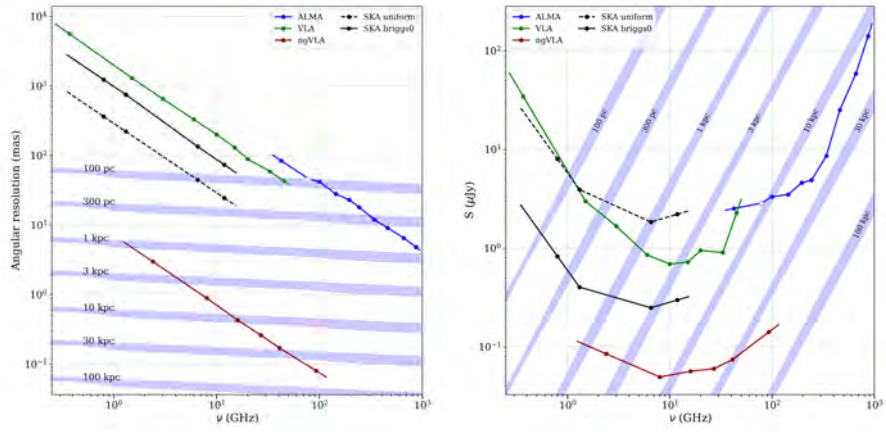

Figure 5.6: Angular resolution (left) and sensitivity (right) of current and future sub-mm/radio interferometers as a function of frequency, for an 8-hour integration (Bojnordi Arbab et al. 2024). The blue-filled areas show the resolved stellar angular diameter ranges (left), and the stellar flux density ranges for unresolved observations (right), at the indicated distances, based on a DARWIN model (Höfner et al. 2022) of AGB atmospheres.

the observer's location, say $\mathbf{E}_\nu(\mathbf{r})$, are what are observable to us. Of particular interest to interferometry is the *correlation* of the electric fields at two observing points, say $\mathbf{r}_1$ and $\mathbf{r}_2$. This is calculated by the *correlator* (Fig. 5.7) of the interferometer. Under the reasonable simplifying assumptions that the radiating source is very far away, and that the emission from two different points in space is spatially incoherent, we can write this correlation as an integral of the observed intensity (I_ν) over solid angle (see Clark, in Taylor et al. 1999), as:

$$V_\nu(\mathbf{r}_1, \mathbf{r}_2) = \int I_\nu(\mathbf{s}) e^{-2\pi i \nu \mathbf{s}\cdot(\mathbf{r}_1-\mathbf{r}_2)/c} d\Omega \tag{5.6}$$

where $\mathbf{s}$ is the unit vector in the direction of the source, and c is the speed of light. It can be seen that Eq. 5.6 depends only on the separation between the two observing points ($\mathbf{r}_1$ - $\mathbf{r}_2$), and not on their absolute positions. The function $V_\nu(\mathbf{r}_1, \mathbf{r}_2)$ is known as the *spatial correlation function* of the field components. Also, Eq. 5.6 can be inverted to find the intensity distribution of the emitting source. The interferometer

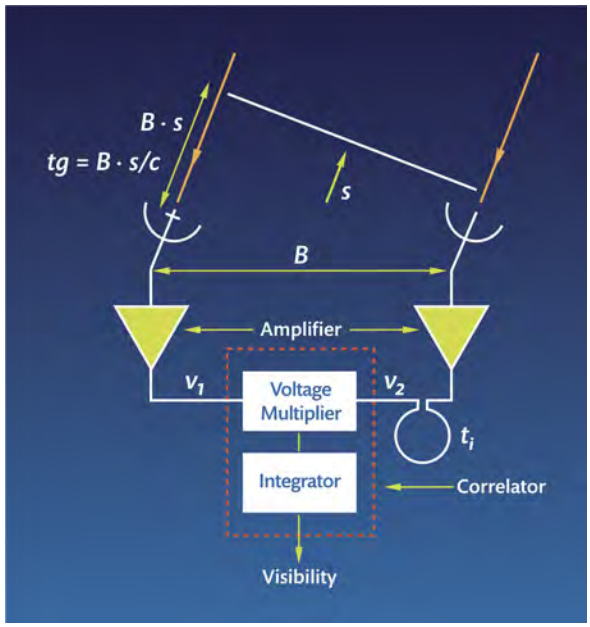

Figure 5.7: Block diagram of a two-element interferometer. t_g is the geometric delay between the times at which the two antennas separated by a baseline **B** receive signal from the far-away astronomical source in the direction **s**. The inputs are first amplified individually, and are then combined in the voltage multiplier after accommodating for the time delay to ensure proper alignment, generating the visibility. The voltage multiplier output is also summed over a short time in the integrator (credit: ALMA observatory).

is an instrument to measure the values of this function.

If we define the coordinate system describing the baseline separations ($\mathbf{r}_1$ - $\mathbf{r}_2$) as (u, v), measured in units of wavelength (λ), and set the components of the sky coordinates (**s**) to be described by the unit vectors (l, m), we can rewrite Eq. 5.6 as:

$$V_\nu(u,v) = \iint A_\nu(l,m) I_\nu(l,m) e^{-2\pi i(ul+vm)} dldm \tag{5.7}$$

where a normalising factor, A_ν(l, m), has also been included to account for the directional sensitivity of the antenna reception. This quantity, $V_\nu(u,v)$, is known as the *complex visibility function*, and has an amplitude and a phase. The fundamental prin-

ciple of radio interferometry, the *van Cittert-Zernike theorem*, states that the complex visibility function is the Fourier transform of the brightness distribution of the source in the sky (see Thompson, Moran, and Swenson, in Thompson et al. 2017).

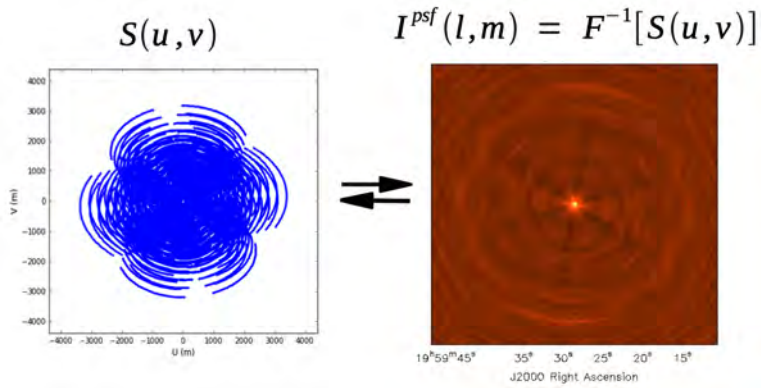

Figure 5.8: A typical *uv* coverage (left) and the corresponding PSF (right) of a modern radio interferometer (credit: NRAO).

The sampling of the *uv* plane can be increased for a given baseline configuration by making use of the fact that the Earth's rotation constantly changes the effective direction of the baseline vectors. This process is known as *Earth rotation synthesis*. Even then, a practical interferometer can never sample the *uv* plane entirely, as it can have only a limited number of discrete baselines. Hence, the inversion of this equation will not provide the exact emission distribution in the sky, but only one which is convolved with the Fourier transform of the sampling function ($S(u,v)$) of the array (see Clark, in Taylor et al. 1999), i.e.,

$$I_\nu^D(l,m) = \iint V_\nu(u,v) S(u,v) e^{2\pi i(ul+vm)} du dv \tag{5.8}$$

where $I_\nu^D(l,m)$ is called the *dirty image*, which is a convolution of the point spread function (PSF) or *synthesised beam* ($B(l,m)$, the Fourier transform of $S(u,v)$) with the actual source intensity distribution ($I_\nu(l,m)$).

$$I_\nu^D(l,m) = I_\nu^{sky}(l,m) * B(l,m) \tag{5.9}$$

Fig. 5.8 shows a typical *uv* coverage and PSF of a modern radio interferometer. The dirty image is contaminated by the sidelobes of the PSF. The purpose of most

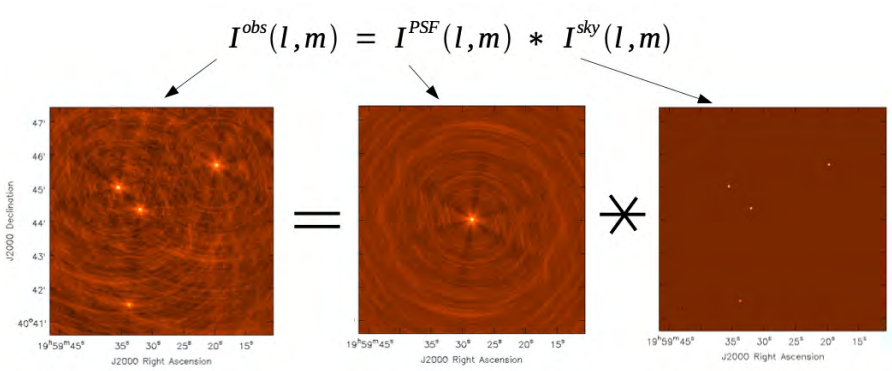

Figure 5.9: The observed (dirty) image, the PSF, and the actual sky distribution of a typical interferometric observation, visually depicting the convolution given in Eq. 5.9 (credit: NRAO).

interferometric imaging algorithms is the Fourier inversion of the observed visibilities to produce the dirty image (Eq. 5.8), followed by the iterative deconvolution of the dirty beam from the dirty image to obtain a clean image representing the true source distribution, without sidelobe contamination. This process is known as *cleaning*, and algorithms like *clean* (Högbom 1974) and *multiscale tclean* (Cornwell 2008) have been developed for this purpose.

In each iteration, the algorithm identifies the position of the peak intensity in the dirty image and subtracts a fraction of the dirty beam (determined by the user-defined 'loop gain') centered at that location. This position and amplitude are recorded as a 'clean component', and the process is repeated on the resulting residual image until the peak intensity drops below a user-defined threshold, usually a multiple of the rms noise. Finally, the accumulated point-source model is convolved with a 'clean beam', i.e., a Gaussian approximating the dirty beam's main lobe, and is added back to the final residual image to produce the restored, clean image. The observed (dirty) image, the PSF, and the actual sky distribution of a typical interferometric observation are shown in Fig. 5.9. Fig. 5.10 shows a flowchart outlining the typical data reduction and clean imaging workflow.

Cleaning is the most widely used method for imaging interferometric observations from telescopes like ALMA (see Sect. 5.3.4), and is the technique adopted to produce the ALMA images presented in Paper I. Sparse interferometric arrays like the Event

Horizon telescope (EHT[3]) often use alternative imaging procedures like regularised maximum likelihood (RML, see e.g. Akiyama & Matthews 2019; Zawadzki et al. 2023) methods, which rely on more Bayesian techniques, and become particularly useful when the visibilities are poorly sampled.

Different weighting schemes can be used to assign weights to visibilities while imaging, to suppress or enhance artefacts/features as necessary. These include *natural weighting*, where all visibilities have the same weight, resulting in the best possible signal-to-noise ratio but poorer angular resolution, and *uniform weighting*, where each measured spatial frequency is given the same weight, irrespective of its sampling density, resulting in higher angular resolution. Additionally, the *Briggs weighting* scheme (Briggs 1995) can be used to balance the trade-off between signal-to-noise ratio and angular resolution, using an adjustable *robustness* parameter, which can take values between -2 (close to uniform weighting) and 2 (close to natural weighting). The weighting scheme used for the images presented in Paper I is Briggs weighting, with a robustness parameter of 0.5.

5.3.2 Calibration

The visibilities observed by an interferometer need not exactly equal the true sky visibilities, as multiple factors, including atmospheric and instrumental distortions will introduce errors in the observed quantities. The ratio of the observed visibilities to the true visibilities is known as the *complex gain* of the interferometer. Based on their origin, gains can be frequency- and/or time-dependent. The process of estimating the true visibilities from the observed ones, by correcting for the various gains, is known as calibration.

There are a variety of calibration steps that need to be applied to the visibility data, before it is ready for imaging. First, corrections for instrumental errors like those in pointing and antenna positions are applied to the observed data. This is followed by three major calibration processes, namely bandpass calibration, phase calibration, and flux calibration. To enable these calibrations to be performed, calibrator sources, whose flux and position are well known, mostly quasars or solar system objects, are observed at specific intervals in between the science target observations.

Bandpass calibration compensates for the variation of the antenna gains with frequency, by applying the gain solutions calculated to flatten the observed spectrum of the bandpass calibrator to the science target. The bandpass calibrator has to be a

[3] https://eventhorizontelescope.org

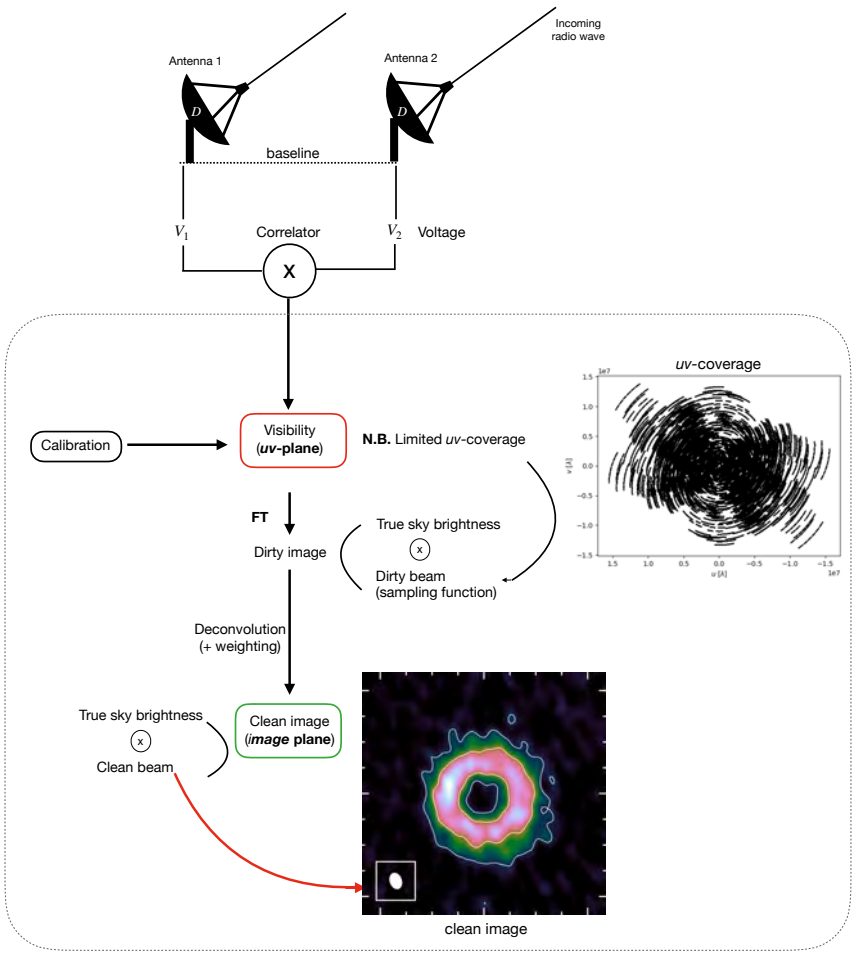

Figure 5.10: A flowchart showing the various steps involved in the reduction and imaging of interferometric data (credit: M. Andriantsaralaza, Ph.D. thesis; W. H. T. Vlemmings; T. Khouri; Paper I).

source with a flat spectrum, or a known spectral index.

Phase calibration corrects the frequency-independent gains, i.e., it compensates for the relative time variations in the phase of the correlated signal, caused by the

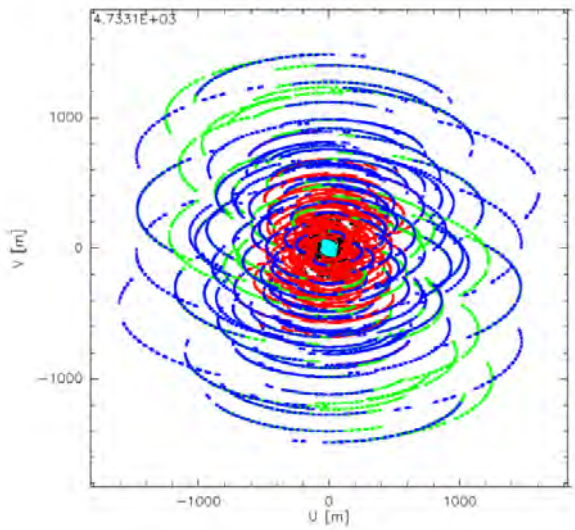

Figure 5.11: Combination of visibilities from different baseline configurations, shown in the *uv* plane. The red points indicate compact baselines, while the green and blue points show successively extended array configurations (credit: NRAO).

atmosphere. Phase calibration is hence crucial to recover the source structure in the sky. The phase calibrator has to be a point source (i.e. zero phase), or an object with a precisely known source structure, located close to the science target in the sky, so that the atmosphere is roughly the same towards both.

Flux calibration is used to set the amplitude scales of the observed intensity. It also compensates for the atmospheric opacity and instrumental signal loss. The flux calibrator needs to be a source for which an accurate, independently calibrated flux model exists, typically a well-monitored quasar. Previously, solar system objects like planets and asteroids were also used as flux calibrators. Errors in calibration, for example those caused by badly modelled flux calibrators, can lead to artefacts in the final images, as discussed in Sect. 3.2 of Paper I.

Self-calibration is another method of correcting the phase errors, but at smaller timescales than that of phase calibration, by using a sky model created from bright, compact emission (like a compact continuum) from the science target itself, rather than a separate calibrator source. This gives the added advantage that the assumption

during normal phase calibration that the atmospheric variations are the same towards the calibrator and the target, is no longer required. Self-calibration is a very powerful technique, but may or may not provide significant improvements in sensitivity, depending on the compactness and strength of the emission chosen to create the model, and the timescales of the leftover phase variations present in the calibrated *uv* data. In Paper I, self-calibration was attempted on several tunings of the ALMA data, but did not result in any noticeable improvement in the final images.

5.3.3 Data combination

It is possible to combine multiple interferometric observations performed towards a source by concatenating the visibilities from the different observations. This leads to a better sampling of the *uv* plane, and therefore to images of better fidelity and sensitivity. It is also possible to concatenate data from different arrays of an interferometer, e.g. the 12-m and 7-m arrays of ALMA (see Sect. 5.3.4). The combination of visibilities from different baseline configurations in the *uv* plane is shown in Fig. 5.11. Fig. 5.12 shows the ALMA images of the barred spiral galaxy M100 in CO $J = 1 - 0$ line emission, before and after data combination.

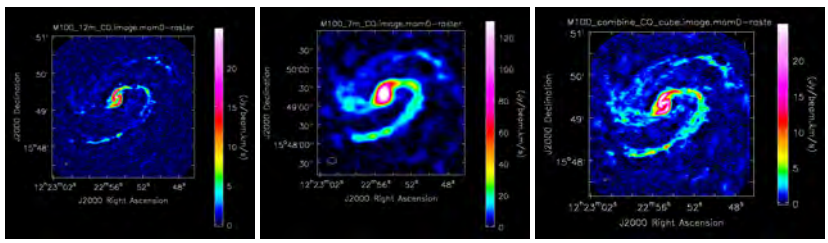

(a) 12-m array image **(b)** 7-m array image **(c)** Combined image

Figure 5.12: Images of the CO $J = 1 - 0$ emission from the galaxy M100, (a) using the ALMA main array, (b) using the ACA, and (c) using combined data from the ALMA main array and the ACA. Note the increased fidelity in the combined image (credit: NRAO).

For Paper I, two different ALMA datasets, both from the main (12-m) array, but with different array configurations, were combined (see Sect. 3.3 of Paper I). This significantly improved the quality of the resulting images, both in terms of angular resolution and sensitivity, and led to the detection of several weak emission lines. It is also possible to combine single-dish and interferometric observations to account

for the zero-spacing information in the *uv*-plane, while achieving the high resolution of the interferometer. This can be done using various methods including feathering (e.g. Cotton 2017) and joint deconvolution (e.g. Rau et al. 2019).

5.3.4 The ALMA observatory

The Atacama Large Millimeter/sub-millimeter Array (ALMA[4], Fig. 5.13), is a 66 antenna sub-mm/mm aperture synthesis interferometer, located at ~5000 m altitude in the Chajnantor plateau in Chile, close to the APEX telescope. The extremely dry atmosphere and the high altitude of Chajnantor offer excellent conditions for high-sensitivity sub-mm/mm observations.

Figure 5.13: An excited observer at the ALMA site (photo by Mamiko Sato)

ALMA has been operating since 2011, and it is currently the largest sub-mm/mm interferometer in the world, and one of the most complicated scientific instruments

[4]ALMA is a partnership of ESO (representing its member states), NSF (USA) and NINS (Japan), together with NRC (Canada), MOST and ASIAA (Taiwan), and KASI (Republic of Korea), in cooperation with the Republic of Chile.

ever built. It consists of two arrays, with fifty 12-m antennas forming the ALMA main array, complemented by the twelve closely-spaced 7-m antennas of the Atacama Compact Array (ACA), also known as the Morita array. In addition, it also has four single-dish or total-power (TP) antennas. ALMA currently has 9 observing bands, together covering the frequency range of 35−950 GHz, with some interruptions in between. Band 1 is a single-sideband (SSB, Sect. 5.2) system, while bands 3 to 8 are dual-sideband (2SB, Sect. 5.2), and bands 9 and 10 are double-sideband (DSB, Sect. 5.2). One more band (Band 2) is under development, which will cover the frequency range 67−116 GHz. The production of ALMA Band 2 receivers is being carried out by an international consortium which includes the Group for Advanced Receiver Development (GARD[5]) at Onsala Space Observatory, Chalmers University of Technology, Sweden. ALMA can observe in only one band at any given time. Each receiver band can detect two orthogonal linear polarisations. See the ALMA technical handbook[6] for more specifications and details of the ALMA antennas, receivers, and bands.

The antennas of the ALMA array can be arranged in different baseline configurations across the 192 antenna foundation pads, to perform observations aimed at recovering emission at various spatial scales. The minimum and maximum baselines obtainable are 15 m and ∼16 km, respectively, enabling ALMA to observe at a broad range of spatial scales and resolutions. Planned instrumentation upgrades, including the ALMA Wideband Sensitivity Upgrade (WSU[7], see Carpenter et al. 2023; González 2024), which is part of the ALMA 2030 Development Roadmap (Carpenter et al. 2020), are set to deliver large improvements in both bandwidth and sensitivity, dramatically increasing the observational capabilities of ALMA.

This work has used ALMA observations in Band 3 (84-116 GHz). The minimum and maximum baselines, beam sizes, spectral resolutions, and other observational details of the data used in this project are listed in Table 2 of Paper I.

[5] https://www.chalmers.se/en/departments/see/research/oso/advanced-receiver-development-gard/
[6] https://almascience.nrao.edu/documents-and-tools/cycle10/alma-technical-handbook
[7] https://www.almaobservatory.org/en/scientists/alma-2030-wsu/wsu-program/

6

Radiative transfer

The contents of this chapter are broadly based on Rybicki & Lightman (1986) and Peraiah (2001), which serve as the general references wherever other literature is not explicitly cited.

As outlined in Chapter 3, spectral lines serve as essential diagnostic tools for probing the physical and chemical properties of circumstellar envelopes (CSEs). The various techniques employed to observe such emission lines have been described in Chapter 5. A key objective of observing molecular emission lines from sources like AGB CSEs, as in this work, is the determination of molecular abundances. To achieve this, models that solve the radiative transfer (RT) equations based on the properties of the emitting gas are utilised. RT equations provide the theoretical basis for understanding how the intensity of electromagnetic radiation changes as it traverses and interacts with matter, accounting for its absorption, emission, and scattering, enabling the characterisation of the medium's physical properties and radiation field as well.

Accurate determination of molecular abundances in CSEs necessitates well-defined constraints on the existing radiation field and the physical properties of the emitting material, including the stellar luminosity and effective temperature and the radial

variations in the temperature and density of the circumstellar gas and dust. Estimating these parameters requires comprehensive RT modelling of the dust (to determine stellar and dust properties), along with the determination of the gas mass-loss rate and temperature, usually accomplished through RT modelling of CO line emission. Determination of molecular abundances requires further RT modelling of the molecular line emission of the specific species. Consequently, multiple iterations of RT modelling are essential for constraining the properties of the circumstellar dust and molecular gas. This chapter provides a general description of these efforts, outlining the steps involved in estimating the stellar and dust properties, the gas mass-loss rate and hence the density and temperature profiles of the gas, followed by the abundances of various molecular species in the CSE. We begin by describing the basic equations of radiative transfer below.

6.1 Radiative transfer equations

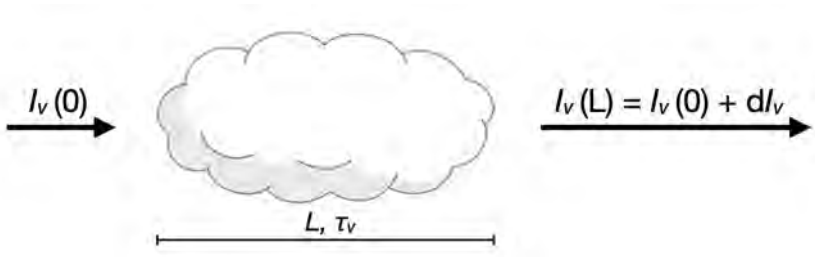

Figure 6.1: Schematic diagram showing the incident ($I_\nu(0)$) and emergent ($I_\nu(L)$) intensity of radiation at frequency ν from a cloud of geometric length L and optical depth τ_ν.

The RT equation describes the variation in the intensity (I_ν) of light as it travels through a medium (e.g. Fig. 6.1) where both absorption and emission processes occur:

$$dI_\nu(s) = -k_\nu(s)I_\nu \mathrm{d}s + j_\nu(s)\mathrm{d}s, \tag{6.1}$$

Here, k_ν and j_ν are the absorption and emission coefficients respectively, and ds is the geometrical depth. The spectral intensity (I_ν) emerging from the medium can be obtained by integrating the RT equation (Eq. 6.1) along the path length (L) through

the medium, as

$$I_\nu(L) = I_\nu(0) + \int_0^L [-k_\nu I_\nu + j_\nu]\mathrm{d}s \tag{6.2}$$

where $I_\nu(0)$ is the initial intensity of the radiation at the beginning of the path. The integral of the absorption coefficient (k_ν) along the path traversed by the radiation is called the optical depth (τ_ν), given by

$$\tau_\nu = \int_0^L k_\nu \mathrm{d}s, \tag{6.3}$$

The ratio of the emission and absorption coefficients is known as the source function (S_ν), written as

$$S_\nu = \frac{j_\nu}{k_\nu}, \tag{6.4}$$

With these definitions, Eq. 6.2 can be rewritten in terms of τ_ν and S_ν, assuming that the optical depth at the beginning of the path, $\tau_\nu(0)$, is zero. This gives

$$I_\nu(\tau_\nu) = I_\nu(0)e^{-\tau_\nu} + \int_0^{\tau_\nu} S_\nu e^{-\tau_\nu}\mathrm{d}\tau_\nu \tag{6.5}$$

Here, the term $e^{-\tau_\nu}$ represents the attenuation of the initial intensity, $I_\nu(0)$, as it traverses a medium of length L and accumulated optical depth τ_ν. The integral term takes into account the emission accumulated along the path, considering both the emission and absorption in the medium implicit in the source function.

It is to be noted that for radiation emitted due to a transition between two rotational energy levels ($u \leftrightarrow l$[1]) of a molecule, the coefficients j_ν and k_ν are dependent on the level populations (n_u and n_l) of the respective energy levels (see Sect. 6.4.1) of the molecule, as

$$j_\nu = \frac{h\nu}{4\pi} n_u A_{ul} \phi(\nu), \tag{6.6}$$

and

$$k_\nu = \frac{h\nu}{4\pi}(n_l B_{lu} - n_u B_{ul})\phi(\nu), \tag{6.7}$$

where $\phi(\nu)$ is the spectral line profile and A_{ul}, B_{ul}, and B_{lu} are the Einstein coefficients for spontaneous emission, stimulated emission, and absorption, respectively. This means that the source function (S_ν, Eq. 6.4) is, in general, dependent on the level

[1] u and l denote the upper and lower energy levels involved in the transition, respectively.

populations, a fact that will become important later on, in Sections 6.4.3 and 6.4.4, where we will see how these equations are used to model emission from sources under different scenarios.

6.2 Envelope Model

For our AGB CSEs, we adopt a smooth, spherically symmetric wind model, based on an isotropic, constant mass-loss rate (MLR, $\dot{M}$) and a fixed dust-to-gas mass ratio (Ψ), as usually done in the literature (e.g. Massalkhi et al. 2024; Danilovich et al. 2019; Agúndez et al. 2017; Velilla Prieto et al. 2019). This assumption has proved fruitful in reproducing the overall observed line shapes and averaged radial intensity profiles for several AGB CSEs, even in cases where the underlying morphology is known to be more complex and discrete.

The central AGB star is defined by its luminosity ($L_\star$) and surface temperature ($T_\star$). We assume that dust is present in the CSE only beyond a distance of three times the stellar radius ($3R_\star$) from the central star, which is termed as the dust condensation radius (R_c, Bladh & Höfner 2012; Höfner & Olofsson 2018). Inside the dust condensation radius, the wind velocity is assumed to be constant (v_0 = 3 km s^{-1}, approximately equal to the sound speed at R_c, see e.g. Danilovich et al. 2015). Any change in the velocity profile here will most likely not affect our RT results significantly, as the volume of gas in this region (1-3 $R_\star$) is very low compared to the overall CSE. From R_c onwards, the wind is assumed to be smoothly accelerating, eventually reaching a terminal expansion velocity (v_∞). This velocity profile can be expressed as

$$v_{\rm exp}(r) = v_0 + (v_\infty - v_0)\left(1 - \frac{R_c}{r}\right)^\beta, \tag{6.8}$$

where β is a parameter that controls wind acceleration (Höfner & Olofsson 2018). We assume no drift velocity between the gas and the dust, and also adopt a constant turbulent velocity of 1.5 km s^{-1}. The circumstellar gas density was assumed to follow an inverse square law, given by

$$n_{\rm H_2} = \frac{\dot{M}_g}{4\pi r^2 v(r)} \frac{1}{m_{\rm H_2}}, \tag{6.9}$$

where $\dot{M}_g$ denotes the gas MLR, $v(r)$ is the wind expansion velocity at radius r, and $m_{\rm H_2}$ is the molecular mass of hydrogen. The gas temperature in the CSE was assumed

to be a power law, given by

$$T(r) = T_0 \left(\frac{r}{R_{\rm in}} \right)^{\alpha}, \tag{6.10}$$

where T_0 is the temperature of the gas at the inner radius ($R_{\rm in}$). The fractional abundance of a given molecule is expressed relative to molecular hydrogen (H_2) and is defined as

$$f_X(r) = \frac{n_X(r)}{n_{\rm H_2}(r)}, \tag{6.11}$$

where $n_X(r)$ and $n_{\rm H_2}(r)$ are the number density distributions of the molecule and H_2, respectively. H_2 is used as the reference since it has the most spatially extended abundance distribution among all circumstellar molecular species (Huggins & Glassgold 1982). With the envelope model and various related parameters thus defined, we shall now proceed step-by-step to describe the various RT modelling procedures we need to employ in order to estimate physical quantities and molecular abundances using the observed data.

6.3 Dust modelling

AGB stars are a major source of dust production in the universe (e.g. Millar (Ch. 5), in Habing & Olofsson 2003; Gail & Sedlmayr 2013; Höfner & Olofsson 2018). The main characteristics of AGB dust formation are summarised in Sect. 2.3.3.3. Not only does dust play a crucial role in the dynamics of the CSE (see Sect. 2.4), but it also affects the circumstellar radiation field.

To a first approximation, the dust emission behaves roughly like a blackbody. The spectral energy distribution (SED) of an AGB star and its CSE comprises of the stellar continuum radiation, spectral features from the stellar atmosphere, and the emission from the surrounding dust. Following the RT equations described in Sect. 6.1, the dust gets heated by absorbing radiation from the central star and re-emits it in the infrared, shifting the peak of the SED to longer wavelengths (~1 μm). Therefore, fitting the overall SED of the star and the CSE, obtained from multi-wavelength photometric observations (typically from the optical to the far-IR), can be used to constrain dust RT models, yielding the properties of both the AGB star and its circumstellar dust. Fig. 6.2 show examples of SEDs and modelled fits to the photometric data towards several AGB stars (see Gullieuszik et al. 2012, and Paper II).

The most important factor in dust RT modelling is the dust optical depth, given by

$$\tau_\nu = \int_{r_{\rm in}}^{r_{\rm out}} k_\nu(r)\, dr, \tag{6.12}$$

where k_ν is the absorption coefficient, also known as the dust opacity, and $r_{\rm in}$ and $r_{\rm out}$ are the inner and outer radius of the CSE, respectively.

We used the RT code MCMax (Min et al. 2009) to model the SEDs of our stars (see Paper II). MCMax employs the Monte Carlo method to solve the RT equations for dust, using stochastic simulations of the interactions between photons and dust grains, taking into account absorption, re-emission, and scattering. We use 1-dimensional (1D) models assuming a standard dusty CSE. In the MCmax modelling process, stellar photon packets undergo random walks where their paths are affected by the dust. The temperature of the grains increases as photons are absorbed. This process is iteratively adjusted to achieve a balance between the energy absorbed and emitted by the dust grains, allowing us to constrain the dust temperature profile. The combined SED of the star and the dust is constructed from the escaping photons which now carry information about both the stellar spectrum and the thermal emission from the dust. This method offers reliable fits to the SEDs despite being computationally expensive and relatively slow.

For the stellar spectra, we mainly used the COMARCS model atmospheres developed by Aringer et al. (2019). In a few cases where we could not get any good fits using spectra from the temperature range provided by the COMARCS models (2500 - 3300 K), we had to resort to cooler stars which were then described by black bodies. The dust grains were assumed to be composed of amorphous carbon, as is typical for C-type AGB stars, with optical properties as described in Suh (2000), and a uniform radius of 1 μm. We tested different grain sizes in the usually expected range for AGB stars (see e.g. Mattsson et al. 2010; Höfner & Olofsson 2018, and references therein), but found that sizes smaller than 1 μm either led to unsatisfying SED fits or forced the dust condensation radius ($R_{\rm c}$) to be much larger than $3R_\star$ in order to yield reasonable dust condensation temperatures ($T_{\rm c}$), which is in contradiction to the dust-driven wind scenario, leading us to adopt 1 μm as our dust grain radius. The reasons and limitations of this choice have been discussed in more detail in Paper II. A constant dust grain density of 2 g cm^{-3} was adopted for the amorphous carbon grains.

The three free input parameters were the stellar luminosity, stellar temperature, and the dust-mass-loss rate. Source-specific parameters like the distance (d) and

the expansion velocity ($v_{\rm exp}$) were fixed inputs to the code, necessitating the use of individual grids for each star. Each model then calculated the dust optical depth at 10 μm (τ_{10}) and the dust condensation temperature ($T_{\rm dust}$), together with the temperature and density profiles of the dust in the CSE, and returned a corresponding modelled SED (see Fig. 6.2).

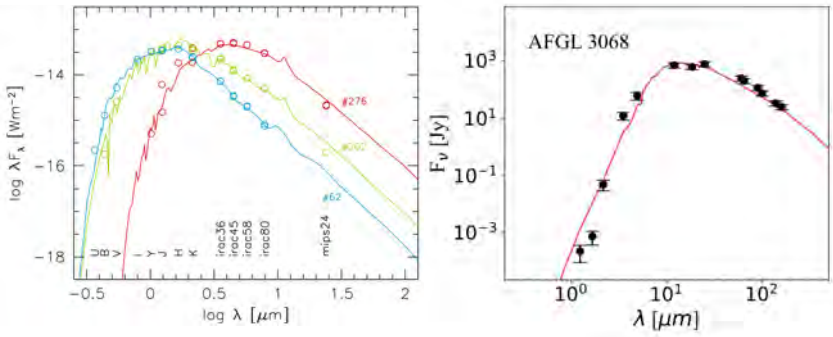

Figure 6.2: *Left*: Photometric data points and the fitted SEDs for three AGB stars (Gullieuszik et al. 2012); *Right*: Fit to the SED of the C-type AGB star LL Pegasi (Paper II).

To find the best-fit model, we used the reduced chi-square ($\chi^2_{\rm red}$) statistic to compare the observed and modelled SEDs, given by

$$\chi^2 = \sum_{i=1}^{N} \frac{(F_{{\rm mod},\lambda} - F_{{\rm obs},\lambda})^2}{\sigma_\lambda^2}, \qquad \chi^2_{\rm red} = \frac{\chi^2}{N - p} \tag{6.13}$$

where N denotes the number of individual flux points, F_λ is the flux density, σ_λ is the corresponding uncertainty and p is the number of free parameters in the grid. Fig. 6.2 shows SED fits thus obtained towards two of the sources. The resulting dust and stellar properties are in turn used as inputs to the CO gas RT modelling (see Sect. 6.4.4.1). To summarise, by finding the best-fit model SED, we obtain estimates of the following parameters: $T_\star$, $L_\star$, $\dot{M}_{\rm dust}$, τ_{10}, $T_{\rm dust}(r)$. See Paper II and Andriantsaralaza (2024) for a detailed discussion on the observed SEDs, input parameters, modelling strategy, results, and the related uncertainties.

6.4 Gas radiative transfer

In the previous section, we discussed the radiative transfer for the circumstellar dust. With the stellar and dust parameters now constrained, the next step is to solve the RT equation for the circumstellar molecular gas. We do this in two steps. First, to determine the gas-mass-loss rate and the temperature and density profiles of the gas, we model CO line emission. We can then model line emission from other molecules, to constrain their circumstellar abundance profiles. See Sect. 6.4.4.1 for the motivation behind the use of CO for mass-loss-rate determination. The basic theory involved in the RT modelling of spectral line emission is discussed below.

6.4.1 Population of molecular energy levels

Determining the level populations, i.e., the distribution of particles among the distinct energy levels of a molecule is crucial to RT modelling, as this directly influences the intensities of the spectral lines formed by various transitions of the molecule. We focus here on rotational energy levels. Level populations are usually determined by the density and kinetic temperature of the gas. It is either radiative or collisional processes that lead to transitions between the various energy levels of a molecule. These are briefly discussed below.

6.4.1.1 Radiative processes

In radiative excitation, a molecule is excited from a lower level (l) to an upper level (u) by absorbing radiation. Similarly, the molecule can de-excite ($u \rightarrow l$) by the emission of radiation. The rates of absorption and emission depend on various factors: the spectral intensity of the incidient radiation at the frequency $\nu = \Delta E/h$, where ΔE is the difference in energy between the two transition levels (E_u - E_l); the number of particles in the lower level (n_l) for absorption, or the upper level (n_u) for emission, and the corresponding Einstein coefficient (see Sect. 6.4.1.3 and Fig. 6.3).

6.4.1.2 Collisional processes

On the other hand, collisional processes are those in which the excitation and de-excitation of a molecule is caused by collisions between the molecule and its collision partners (typically H_2) in the medium. The collisional excitation (C_{lu}) and de-excitation (C_{ul}) rates between two levels l and u depend on the molecule and are

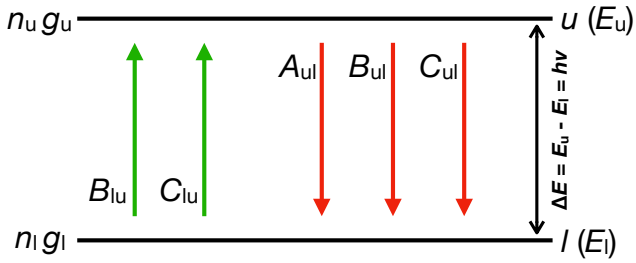

Figure 6.3: Possible excitation (green) and de-excitation (red) mechanisms in a two-level system, with lower level (l) energy E_l and upper level (u) energy E_u. A_{ul}, B_{ul}, and B_{lu} are the Einstein coefficients for spontaneous emission, stimulated emission, and absorption, respectively, whereas C_{lu} and C_{ul} represent the collisional excitation and de-excitation rates. ΔE is the energy difference between the two levels, and n_u and n_l denote the numbers of molecules in the upper and lower levels, respectively. g_u and g_l are the statistical weights of the two levels.

related to each other by the formula

$$\frac{g_l C_{lu}}{g_u C_{ul}} = \exp\left(-\frac{h\nu}{k_B T_k}\right), \tag{6.14}$$

where T_k is the gas kinetic temperature. Tabulated values of collisional rate coefficients (γ_{ul}, in units of $cm^3 s^{-1}$) are usually available for most major molecular species in various databases, like LAMDA[2], for various collision partners (H_2, He, etc.), from which the values of C_{ul} can be calculated as

$$C_{ul} = n(X)\gamma_{ul}, \tag{6.15}$$

where $n(X)$ is the number density of the chosen collision partner (van der Tak et al. 2007). Once C_{ul} is known, C_{lu} can be obtained using Eq. 6.14. When collisional rate coefficients for a given molecule are not available in such databases, values from a molecule of comparable size are often adopted instead. In typical circumstellar conditions, molecular hydrogen (H_2) is generally assumed to be the main collision partner, since it is the most abundant species in the gas phase.

[2] https://home.strw.leidenuniv.nl/~moldata/

6.4.1.3 The two-level system

For a two-level system (see Fig. 6.3), considering both radiative and collisional processes, the overall rate of change of the number of molecules in the lower level (l) can be written as

$$\frac{dn_l}{dt} = A_{ul}n_u + B_{ul}n_u I_\nu + C_{ul}n_u - B_{lu}n_l I_\nu - C_{lu}n_l. \tag{6.16}$$

Conservation of the total number of particles also gives

$$n_l + n_u = n_{\rm tot}. \tag{6.17}$$

Eqs. 6.16 and 6.17 together form a set of equations that can be solved to obtain the individual level populations. These equations can be expanded to multi-level systems as well (see Sect. 6.4.4).

6.4.2 Statistical equilibrium

Given a set of physical conditions, a multi-level system, i.e., a system of molecules of a particular species having a large number of energy levels, achieves statistical equilibrium. This means that there is no net change in the overall level populations, as the number of molecules in each energy level stays constant ($\mathrm{d}n_i/\mathrm{d}t = 0$). In this case, the relative population of each unique set of energy levels can be described by a Boltzmann distribution characterised by a particular excitation temperature ($T_{\rm ex}$), as

$$\frac{n_u}{n_l} = \frac{g_u}{g_l} e^{-\Delta E/k_{\rm B}T_{\rm ex}} \tag{6.18}$$

where $\Delta E = E_u - E_l$ is the difference in energy between the two levels, and $k_{\rm B}$ is the Boltzmann constant. Depending on the excitation temperature, we can classify this further into local thermodynamic equilibrium (LTE) and non-LTE scenarios. Differentiating between LTE and non-LTE conditions is crucial for RT analysis. These cases are described in more detail in the sections below.

6.4.3 Local thermodynamic equilibrium

A source is said to be in local thermodynamic equilibrium (LTE), if the level populations for all level pairs can be described by a Boltzmann distribution (Eq. 6.18), characterised by a single excitation temperature ($T_{\rm ex}$), which is equal to the kinetic

temperature (T_k) of the gas, i.e., $T_\mathrm{ex} = T_\mathrm{k}$, for all energy level pairs (Eq. 6.19).

$$\frac{n_u}{n_l} = \frac{g_u}{g_l} e^{-\Delta E / k_\mathrm{B} T_\mathrm{k}} \tag{6.19}$$

This also means that the population of any individual level (n_i) is related to the total population (n_tot) as

$$\frac{n_i}{n_\mathrm{tot}} = \frac{g_i}{Z_\mathrm{rot}} e^{-E_i / k_\mathrm{B} T_\mathrm{k}}, \tag{6.20}$$

where Z_rot is the rotational partition function, given by

$$Z_\mathrm{rot} = \sum_i g_i \exp\left(-\frac{E_i}{k_\mathrm{B} T_\mathrm{ex}}\right). \tag{6.21}$$

Effectively, LTE conditions occur in collision-dominated environments, where the level populations are fixed to a Boltzmann distribution independent of the radiation field present. In such a case, the source function (S_ν, Eq. 6.4) reduces to $S_\nu = B_\nu(T_\mathrm{ex})$ $= B_\nu(T_\mathrm{kin})$, where B_ν is simply the spectral intensity according to the Planck function

$$B_\nu(T) = \frac{2h\nu^3}{c^2} \frac{1}{e^{h\nu / k_\mathrm{B} T} - 1} \tag{6.22}$$

Since the LTE source function is independent of the level populations, it is possible to directly solve the LTE RT equations analytically. Hence, if LTE conditions are met, level populations can be estimated without the need to explicitly solve coupled differential equations, and the population diagram method (Sect. 6.4.3.1) can be used to obtain the total column densities of molecules. In Paper I, we used this technique to obtain abundance estimates of a large number of molecular species towards the stars in our sample. This method is briefly described below.

6.4.3.1 Population diagrams

The population diagram, also called rotational diagram, is a commonly employed column density estimation method for molecules with multiple detected rotational transitions. It allows for the determination of both the rotational temperature, T_rot, and the total column density, N_tot. The term T_rot is used to denote the excitation temperature only to emphasise that the transitions being considered here are rotational transitions. This method relies on the assumption that the rotational level populations follow a single Boltzmann distribution (Eq. 6.18), as, for example, in the LTE sce-

nario (Sect. 6.4.3). The source-averaged column density of a given upper rotational energy level (u), N_u, can be estimated from the observed velocity-integrated intensity, $\int I_{ul} dv$, of the rotational emission line ($u \rightarrow l$) as (Goldsmith & Langer 1999)

$$N_u = \frac{4\pi \int I_{ul} dv}{hcA_{ul}\Omega_s} \left(\frac{\tau_\nu}{1 - e^{-\tau_\nu}} \right) \tag{6.23}$$

where ν_{ul} is the transition rest frequency, A_{ul} is the Einstein A-coefficient, Ω_s is the solid angle of the emitting region, h is the Planck constant, c is the speed of light in vacuum, and τ_ν is the optical depth of the line. N_u is also related to the rotational temperature (the excitation temperature of the rotational transitions, which is equal to the kinetic temperature under LTE) and the total column density by

$$\ln \frac{N_u}{g_u} = \ln \frac{N_{\rm tot}}{Z(T_{\rm rot})} - \frac{E_u}{k_{\rm B} T_{\rm rot}}, \tag{6.24}$$

A plot of $\ln(N_u/g_u)$ versus $E_u/k_{\rm B}$ will yield a straight line if the assumptions of a single Boltzmann distribution of the level populations and optically thin emission hold. The slope of the line is related to $T_{\rm rot}$, while the intercept provides $N_{\rm tot}$. The population diagrams and their straight line fits for selected molecules from Paper I are shown in Fig. 6.4.

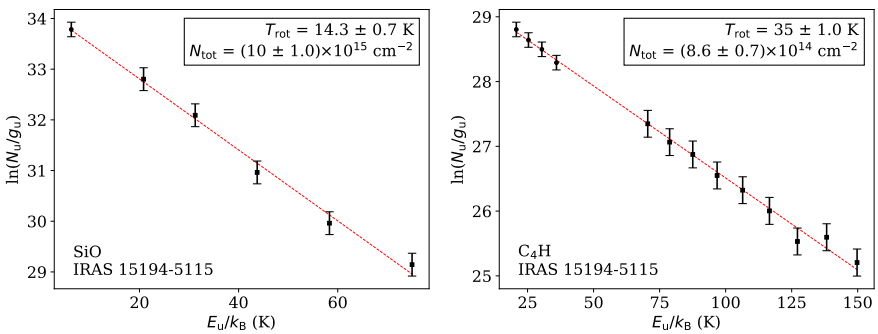

Figure 6.4: Population diagrams for SiO (left) and C_4H (right), for IRAS 15194−5115. The solid line (red) is the best-fit linear model to the data (black points). Circle and square points denote lines observed with ALMA and APEX, respectively (Paper I).

Under perfect LTE conditions, the points in the population diagram should all lie in a perfect straight line. Hence, significant deviations from such linear behaviour, beyond the expected uncertainties, can be taken as indications of the prevalence of non-LTE conditions, if all the lines included are known to be optically thin. This also means that the intensities of multiple spectral lines of a molecule must be observed to determine if the system is possibly in LTE or not. However, it is to be noted that a population diagram can, in principle, yield straight line fits to the points in it even when the system is in non-LTE, for example if the rotational excitation temperature is set by the radiation field such that a Boltzmann distribution is reached in the level populations. In such a case, the rotational temperature will be the same as the radiation temperature ($T_{\rm rad}$) but not necessarily the kinetic temperature of the gas.

Further, using the column densities derived from population diagrams, we can calculate the molecular fractional abundances (see Eq. 6.11) relative to H_2 using

$$f_{\rm X} = \frac{2\pi m_{\rm H} v_{\rm exp} N_{\rm tot,X}}{\dot{M}} \left(\frac{R_{\rm e}^2}{R_{\rm e} - R_i} \right), \tag{6.25}$$

where $\dot{M}$ is the gas mass-loss rate, $v_{\rm exp}$ is the gas expansion velocity, $m_{\rm H}$ is the mass of the hydrogen atom, and R_i and $R_{\rm e}$ are the inner and outer radii of the emitting region, respectively. In Paper I, we used emitting regions estimated from our ALMA maps and mass-loss rates obtained from the literature, to derive the fractional abundances of multiple molecular species using Eq. 6.25. This equation assumes a CSE model with an isotropic, constant mass-loss rate, in line with the CSE model used for our non-LTE RT models (Sect. 6.2), except for the uniform, terminal velocity, gas expansion assumed here, in contrast to the accelerating velocity profiles used in the RT models. However, this does not constitute a significant difference, given that the contribution of the accelerating regions, which lie very close to the star, to large aperture spectra used to calculate the line intensities used in the population diagrams is very small.

6.4.3.2 Approximate abundance estimates from single lines

If only one or two transitions of a molecule are detected, or the detected transitions cover only a narrow range of upper-level energies, the population diagram method is not useful. In such cases, we obtain approximate estimates of the fractional abundances using the velocity-integrated flux of the highest signal-to-noise line available, under LTE assumptions. Assuming a constant excitation temperature $T_{\rm ex}$ through-

out the emitting region and an r^{-2} density distribution, the approximate fractional abundance is calculated using the following analytical equation

$$f_{\rm X} = 1.3 \times 10^{-19} \frac{v_{\rm exp} DZ(T_{\rm ex})}{g_u A_{ul} \dot{M}(R_{\rm e} - R_i)} e^{E_u/k_{\rm B}T_{\rm ex}} \int S_{ul} dv, \tag{6.26}$$

where $v_{\rm exp}$ is the expansion velocity of the CSE in km/s, $\dot{M}$ is the gas-mass-loss rate in $M_\odot\,{\rm yr}^{-1}$, D is the distance to the star in kpc, R_i and $R_{\rm e}$ are the inner and outer radius of the emitting region in cm, and $\int S_{ul} dv$ is the line integrated intensity in units of Jy km/s. We present such abundance estimates for several species in Paper I. This equation assumes the same CSE model as Eq. 6.25.

6.4.4 Non-LTE conditions

Whereas the level populations cannot be described with a single $T_{\rm ex}$ that corresponds to $T_{\rm kin}$ in the non-LTE case, the system is still in statistical equilibrium (i.e., $\mathrm{d}n_i/\mathrm{d}t = 0$), and Eq. 6.18 still holds, but with $T_{\rm ex}$ now variable across different level pairs (i.e., $T_{\rm ex} \neq T_{\rm k}$). In this case, to obtain the overall level populations, we have to solve the statistical equilibrium equations in non-LTE for all levels simultaneously, with all possible radiative and collisional processes that can affect the level populations taken into account. Expanding Eq. 6.16 to a multi-level case, the level population equations to be solved can be summarised as (van der Tak et al. 2007)

$$\frac{dn_i}{dt} = \sum_{j \neq i}^{N} n_j P_{ji} - n_i \sum_{j \neq i}^{N} P_{ij} = 0, \tag{6.27}$$

where

$$P_{ij} = \begin{cases} A_{ij} + B_{ij} I_\nu + C_{ij}, & \text{if } i > j \\ B_{ij} I_\nu + C_{ij}, & \text{if } i < j \end{cases} \tag{6.28}$$

are the transition rates, and

$$\sum_{i}^{N} n_i = n_{\rm tot}, \tag{6.29}$$

as in Eq. 6.17. Most importantly, in the non-LTE case, the source function is not independent of the level populations as in LTE, but depends on them as given by Eq. 6.6 and Eq. 6.7. This means that the level populations depend on the radiation field (Eqs. 6.27, 6.28) simultaneously as the source function in the RT equations

depends on the level populations.

Solving such coupled differential equations demands detailed modelling using numerical approaches, as there is no analytical way to solve these simultaneously across many energy levels. In Paper II, we employ well-tested, detailed non-LTE radiative transfer codes, namely the Monte Carlo Program (MCP, Schöier & Olofsson 2001), and the Accelerated Lambda Iteration (ALI, Rybicki & Hummer 1991; Maercker et al. 2008) code, to solve the non-LTE radiative transfer for CO and CS rotational emission lines, respectively. Our methodology is elaborated below.

6.4.4.1 CO as a tracer of gas properties

In order to determine the molecular abundances of various species, we first need to derive the gas mass-loss rate and the density and temperature profiles of the circumstellar gas. Carbon Monoxide (CO) is the most commonly used molecular species for tracing gas properties and estimating such physical parameters of the source medium. CO is the second most abundant species in CSEs, after molecular hydrogen (H_2). H_2, though more stable and abundant than CO, cannot be used for such purposes as it has no rotational emission lines owing to its lack of a permanent electric dipole moment as a homonuclear diatomic molecule, and hence cannot be observed in multiple transitions.

Further, CO is easily formed in CSEs due to the abundant availability of carbon and oxygen, and is ubiquitously present, tracing all morphological structures within the CSE, from small to large scales. Because of its high binding energy, CO is also a very stable molecule, whose emission extends far beyond that of all other circumstellar molecules, and hence can be used to trace the CSE from relatively very close to the central AGB star, to far out regions where all other species are photodissociated. Owing to its high self-shielding, CO has a large photodissociation radius, second only to that of H_2. Its low chemical reactivity makes it stable against chemical destruction as well. The excitation energies of CO are quite low compared to other species, and it is hence easily collisionally excited, making it a very good tracer of density and temperature.

6.4.4.2 The MCP RT code

We employ detailed radiative transfer models constrained using the CO line intensities and line profile shapes, to estimate the physical properties of the gas, including mass-loss rate, density and temperature. We used the 1D, non-LTE RT code Monte

Carlo Programme (MCP, Schöier & Olofsson 2001) to model the CO line emission. MCP has been widely used in the literature to model CO and other line emission (e.g. Schöier et al. 2013; Danilovich et al. 2015) from AGB CSEs.

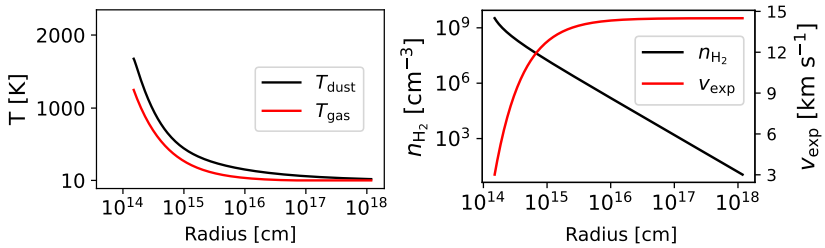

Figure 6.5: An example of the profiles of the various physical parameters involved in the dust and gas RT models, taken from a random point in the grid. Left panel: dust temperature (black), gas temperature (red); right panel: gas density (black), gas expansion velocity (red). Note that the gas expansion velocity accelerates in the inner part of the CSE but eventually reaches a constant value given by the terminal expansion velocity. The temperature profiles can be approximated by power laws, and the density profile decreases as r^{-2}.

MCP uses a Monte Carlo approach (Bernes 1979; Schöier 2000) to solve for the level populations (see Eqs. 6.27 - 6.29). This involves successively propagating a number of model photons as random walks through the medium and keeping track of all the absorption and emission events that take place corresponding to each of them, within every box or shell the modelled region is divided into. These are then used to recalculate the level populations iteratively using statistical equilibrium equations, also taking into account the supplied rates of collisional excitation and de-excitation. The convergence speed of the level populations for such a method will depend on several factors, most importantly the optical depth of the transitions. Higher optical depths lead to slower convergence. The number of model photons used also affects the overall computation time, as the number of computations required to trace the photons through the medium greatly increases with the number of photons used in the models. Once the level populations have satisfactorily converged, the emerging intensity of the radiation can be calculated using the RT equations (Eq. 6.5). We use the ray-tracing program known as PRF (P. Bergman, priv. comm.) for this purpose.

MCP takes as input the results from the dust modelling ($T_\star$, $L_\star$, $\dot{M}_{\rm dust}$, τ_{10}, $T_{\rm dust}(r)$; see Sect. 6.3), the distance to the star, and the terminal expansion velocity of the enve-

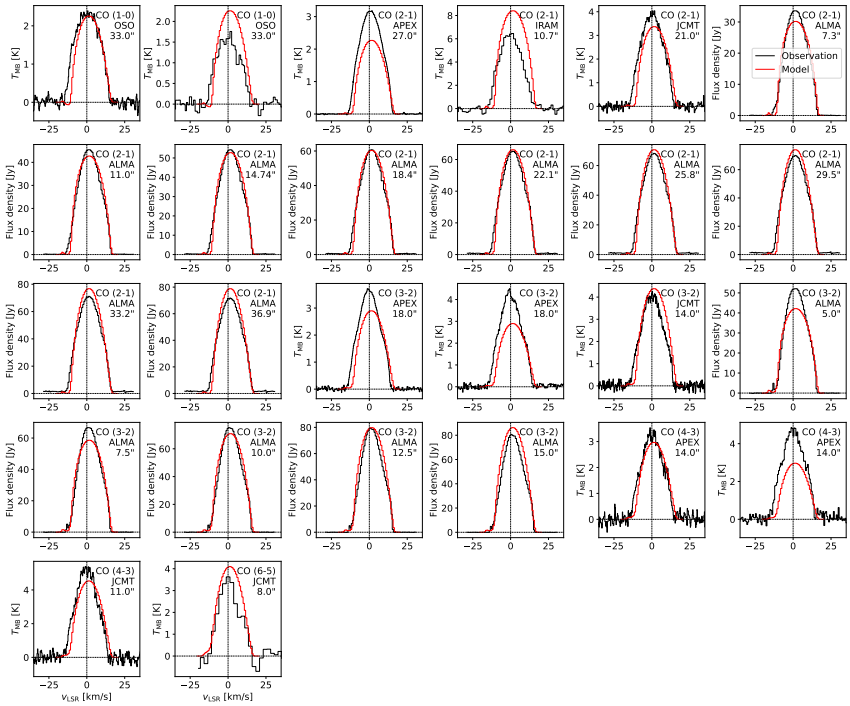

Figure 6.6: Best-fit modelled CO line profiles (red) compared to observed lines (black), for AFGL 3068. The transition names, telescope used for observation, and the corresponding beam size, are listed on the top right of each panel (Paper II).

lope, and uses the envelope model described in Sect. 6.2. The profiles of the physical parameters used/calculated in the models are shown in Fig. 6.5 for a random grid point. In our CO modelling (see Paper II), we included rotational energy levels from $J = 0 - 40$ in both the $v = 0$ and $v = 1$ vibrationally-excited states. These levels together cover upper level energies ranging from ~5.5 K to ~7578 K. H_2 was considered as the main collision partner, and inelastic CO-H_2 collisional rates provided by Yang et al. (2010) were used, assuming a typical ortho-to-para H_2 ratio of 3. The CO fractional abundance was represented using the formula

$$f(r) = f_0 \exp\left(-\ln 2 \left(\frac{r}{R_{1/2}}\right)^s\right), \tag{6.30}$$

where f_0 denotes the initial photospheric abundance of CO with respect to H_2, $R_{1/2}$ is the photodissociation radius, i.e., the radius where the CO abundance has dropped to $f_0/2$, and s is the slope. We adopted a typical canonical value of $f_0 = 1 \times 10^{-3}$ for all stars (e.g. Danilovich et al. 2015). Values of $R_{1/2}$ and s corresponding to the input mass-loss rates and terminal expansion velocity were calculated from the tables presented by Saberi et al. (2019).

The free parameters in the grid of models were the gas mass-loss rate ($\dot{M}_g$), and the kinetic temperature profile of the gas (see Eq. 6.10), represented by the peak temperature T_0 and slope α. The best fit model was estimated using a chi-squared (χ^2) minimisation process between the modelled and observed CO line intensities, combined with a manual check of the match between the overall shapes of the modelled and observed line profiles. The best-fit spectra thus obtained for one of the sources are shown in Fig. 6.6. Multi-aperture spectra extracted from ALMA cubes were used wherever available, so as to also include spatial constraints in the fit. The grid search and best-fit estimation process, including the use of multi-aperture ALMA spectra, has been described in detail in Paper II. Once the gas mass-loss rate is estimated, the gas density profile can be determined using Eq. 6.9. The various parameters derived from the best-fit dust and CO RT models serve as inputs to the molecular line RT models With the gas temperature and density profiles thus estimated, we can now proceed to estimating the molecular abundances.

6.4.4.3 Deriving molecular abundances: The ALI RT code

The importance of molecules as diagnostic tools for astrophysics and astrochemistry has been discussed in Chapter 3. The determination of rigorous molecular abundances in AGB CSEs is of paramount importance to circumstellar astrochemistry. Detailed non-LTE RT codes that model the molecular line emission are often employed to constrain the same. Fig. 6.7 shows the radial fractional abundance profiles of various molecular species in the CSE of IRC +10 216, estimated from non-LTE radiative transfer models constrained using IRAM 30m observations of molecular line emission by Agúndez et al. (2012). In Papers II and III, we used the 1D non-LTE Accelerated Lambda Iteration (ALI) RT code (P. Bergman, priv. comm.; Maercker et al. 2008) to model emission from CS, SiO, SiS, and HCN.

This code is based on the ALI method (Rybicki & Hummer 1991) that is used to increase the computing speed of the matrix operations underlying the iterative level population calculations described below. The version of ALI that we use additionally includes another similar speeding-up method called Ng acceleration (Ng 1974)

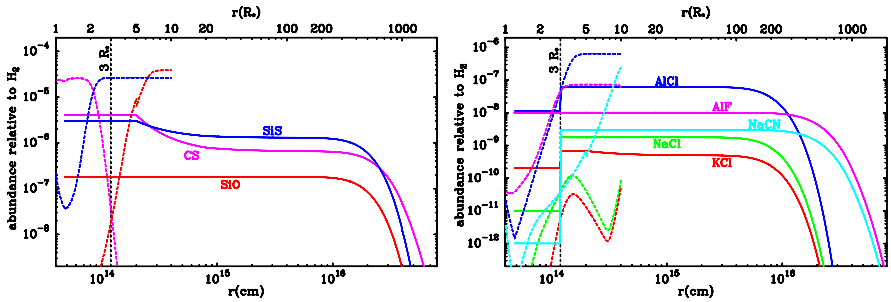

Figure 6.7: Fractional abundance profiles of various molecular species in the CSE of IRC +10 216, derived using radiative transfer modelling (Agúndez et al. 2012).

as well. One major advantage of this RT code over other similar non-LTE packages like RADEX, is that it takes into account the interdependency of the level populations and intensities at the different parts of the cloud as discussed above, whereas RADEX and other codes which rely on approximations like the large velocity gradient (LVG) model use globally averaged intensities often based on photon escape probability calculations (see e.g. van der Tak et al. 2007). However, more complex codes which can take into account 3D source morphologies and asymmetrical geometries are also available, like LIME (Brinch & Hogerheijde 2010). The ALI RT code has been widely used to model molecular lines from AGB CSEs and molecular clouds (Maercker et al. 2008; Schöier et al. 2011; Danilovich et al. 2016). A brief description of the working of the RT code is provided below.

ALI is a 1D code which assumes a spherically symmetric CSE source, which in our case follows the envelope model described in Sect. 6.2. This envelope, extending from the inner radius ($R_{\rm in}$) up to the outer radius ($R_{\rm out}$), is internally divided into multiple spherical shells, with physical parameters like temperature, density, and molecular abundance varying as user-defined gradients from $R_{\rm in}$ to $R_{\rm out}$. It is assumed that the cloud only consists of a single collision partner (typically H_2), the molecule whose abundance is being modelled, and dust. The aim of the code is to iteratively calculate stable non-LTE level populations (see Eqs. 6.27 - 6.29) for the molecule of interest, consistent with the input physical conditions including dust opacity, at every point in the source.

The level populations thus estimated can then be used to determine the source function (S_ν, Eq. 6.4) at every point, by calculating the emission and absorption coefficients based on Eqs. 6.6 and 6.7, and to determine the optical depth (τ_ν, Eq. 6.3).

These values (S_ν, τ_ν) are then used as inputs to solve the RT equation (Eq. 6.5) and estimate the emergent spectral intensity by integrating through the envelope. Using the modelled spectral intensity thus obtained, an antenna temperature (T_A) can be derived, given the distance to the source and the beam size of the telescope used for observations. This can be compared with the observed line spectra to determine the goodness of the model, and can be used to refine the input parameters (abundance profile in this case as explained below, see Eq. 6.32), hence constraining the molecular abundance across the CSE.

Under non-LTE conditions, the level population at each point is affected by the absorption and emission of photons in the corresponding shell, which is in turn influenced by the level populations in the surrounding positions (see Sect. 6.4.4). To properly take this into account, the initial incident intensity at the inner edge of the envelope is first estimated from the stellar radiation field, and an initial estimate of the level populations is calculated assuming LTE conditions in all shells. ALI then considers various paths at different angles along which each point in the envelope can receive incident radiation. The level populations at each point along every such considered path are then updated based on the change in the accumulated incident intensity after traversing each point in the path. At each point where the level populations are to be determined, a local average of the intensities received along each considered path to that point is calculated by integrating over the solid angle (Ω) as

$$\bar{J}_\nu = \frac{1}{4\pi} \int I_\nu \, \mathrm{d}\Omega, \tag{6.31}$$

The level population at that point is then determined by inputting this averaged intensity into Eq. 6.27. This process is repeated iteratively until convergence, simultaneously for all points and considered angles to obtain self-consistent solutions to the level populations across the envelope.

In our modelling, the abundance profiles of the parent species (see Sect. 4.3) were represented by Gaussians, as

$$f(r) = f_0 \exp\left(-\left(\frac{r}{R_e}\right)^2\right), \tag{6.32}$$

where f_0 is the peak abundance close to the star, and R_e is the e-folding radius, i.e., the radius where the abundance falls to f_0/e. f_0 and R_e were the two free parameters. This is valid since the parent species are all centrally-peaked, i.e., their abundances peak close to the central star and decrease gradually as we move further out into

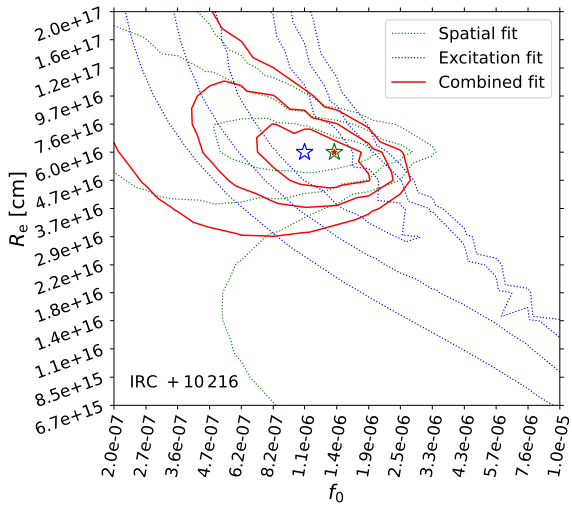

Figure 6.8: Contour map of χ^2 values for our grid of CS models for IRC +10 216, from Paper II. The contours depict 1σ, 2σ, and 3σ ranges, when constrained using only the spatial information from the ALMA CS $J = 2-1$ line (green), vs just the excitation information from the different J lines (blue). The red contours are from when both the spatial and excitation information are simultaneously used to constrain the RT models. The three stars show the best-fit models as estimated from the contour maps of their respective colours.

the CSE. This is because they are formed close to the stellar photosphere, and are destroyed by photodissociation farther out in the CSE. The photodissociation radius of different species varies depending on their shielding capacities and abundances.

The ALI code took as input the results from the dust and CO RT models, i.e. the physical properties of the central star and the circumstellar gas and dust, and assumed the CSE model described in Sect. 6.2. The details of the collisional rates and energy levels used are described in Paper II (CS) and Paper III (SiO, SiS). The PRF (P. Bergman, priv. comm.) ray tracer was used to generate synthetic line profiles, as in the case of the CO modelling, once the level populations were calculated by ALI. We ran a grid of models with different abundance profiles, and compared the resulting modelled line profiles and intensities from each model in the grid to the observed molecular emission line profiles in order to estimate the best-fit model for each source. We also modelled the emission from the isotopologues of these

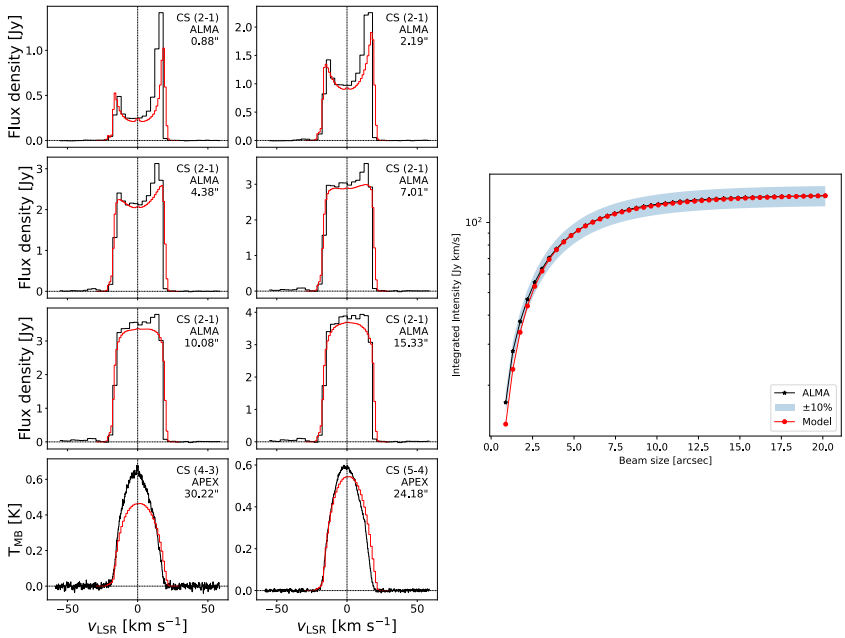

Figure 6.9: Left: Best fit modelled CS line profiles (red) compared to the observed spectra (black) for IRAS 15082−4808. Right: Cumulative intensity plot showing the modelled (red) vs observed (black) integrated line intensities from spectra extracted for progressively increasing apertures from the ALMA cube of the CS $J = 2 - 1$ line for the same star. The blue shaded region denotes a ±10% uncertainty range in the observed integrated intensities. See Paper II for a detailed description.

molecules to derive isotopic ratios.

To constrain our models, we utilised integrated line intensities obtained from multiple apertures from the ALMA data, combined with a range of single-dish (SD) measurements. By incorporating both excitation conditions (derived from various rotational transitions) and the azimuthally averaged spatial distribution of emission (from multi-aperture intensities from the ALMA maps), we effectively probe emission at multiple scales and across different excitation conditions in the outflow. The compact ALMA apertures and higher-J SD lines primarily trace the inner wind structure, whereas the extended ALMA apertures and lower-J SD lines provide constraints on the larger-scale outer wind geometry. The significant improvement in the grid search

and uncertainty estimates brought about by such combined fitting of both spatial and excitation information, and the method adopted to implement the same into the chi-squared (χ^2) formalism, has been presented in detail in Paper II. A contour map of the χ^2 values for the two-free-parameter grid from our CS modelling is shown in Fig. 6.8, clearly depicting the difference in how well the parameters can be constrained when using the excitation information alone, the spatial information alone, and both combined. Note that the combined fit yields more closed contours compared to the other two, hence yielding more robust uncertainty estimates on the fit parameters.

The modelled line profiles from our best-fit CS model are shown in Fig. 6.9 in comparison to the observed spectra for one of our sources. Also shown are the modelled and observed integrated intensities from the multi-aperture ALMA spectra. Note that the ALMA integrated intensities (in units of Jy km s^{-1}) first increase as the aperture size increases, and eventually become flat at large apertures, indicating that all detected emission has now been recovered.

We derived molecular abundances of the parent species and estimated their isotopic ratios. By comparing the line intensities, and also the T_{ex}/T_{kin} ratios across the envelope, from models that did and did not take radiative/IR pumping (see Sect. 3.1) into consideration, we found that radiative excitation cannot be neglected in the case of CS RT modelling. The same conclusion is reached for SiO and SiS from Paper III. We also compared our findings with the results from detailed chemical models, as discussed in Chapter 7. Refer to Paper II for a detailed discussion about our CS modelling results. RT modelling based on the above-described methodology occasionally does not succeed in yielding very good overall fits to multiple observed line profiles of molecules like SiO, unlike in the case of CS, especially when both the spatial and excitation constraints, as discussed above, are simultaneously present. The modelling of the silicon-bearing species SiO and SiS, and the limitations encountered therein, are discussed in detail in Paper III.

7

Chemical modelling

Tracing the formation, distribution, and destruction of molecules in space lies at the heart of astrochemistry. AGB circumstellar envelopes, in particular, present exquisite cosmic chemical laboratories abundant in various kinds of molecular species. The complex molecular chemistry prevalent in AGB CSEs was discussed in Chapter 4.

Chemical modelling is a crucial tool for deciphering molecular observations and unravelling the evolution of chemical complexity in space. Broadly defined, chemical modelling in astrophysics refers to the construction and time-evolution of networks of chemical reactions under astrophysically relevant physical conditions, allowing us to predict changes in the abundances of molecules over time and across different environments. By adjusting parameters like temperature, density, and radiation exposure, we can test various hypotheses about overall reaction types and pathways, as well as the formation and destruction processes of specific species.

While spectroscopic observations reveal the chemical composition of a source by detecting various spectral lines, chemical models make predictions about abundances and their spatial distributions, and can be used to examine the reaction pathways that could have led to the observed chemical composition. Without the use of such models, our interpretation of the chemistry happening in complex astrochemical sources like AGB CSEs would remain largely incomplete. Chemical models thus lead to

deeper insights from observational data than are directly discernible.

In practice, a chemical model starts from a given set of initial abundances for the parent species, assuming basic details about the physical properties of the source medium, and a network of chemical reactions, and lets the chemistry evolve in time, which is achieved by continuously recalculating the abundance of each included species at every radial point by solving ordinary differential equations involving the rate coefficients of the formation and destruction processes of each species. This models the gradual destruction of the parent species by chemical reactions or photodissociation, and the formation of new daughter molecular species, by the various included reaction pathways. The newly formed species may also react among each other. In such models, a larger and more complete input reaction network leads to a more realistic depiction of the overall chemistry.

7.1 Modelling the chemistry in AGB CSEs

Chemical models of AGB CSEs have to take into account the fact that it is a complex interplay of stellar winds, shocks, photochemistry, and dust-gas interactions that drives molecular formation and destruction in these sources, with the chemistry closely coupled with the dynamics across the CSE. Works like Agúndez et al. (2020) have modelled the atmospheric chemical composition of M-, S-, and C-type AGB stars, while detailed chemical modelling studies of the distribution of complex molecular species like long carbon chains (see Fig. 7.1) across the extended CSEs of carbon-stars have also been carried out (e.g. Agúndez et al. 2017). With the advent of high-resolution interferometers like ALMA, it has also become possible to use direct observational results about the spatial distribution of various molecules in the CSE to compare and constrain radiative transfer and chemical models (see e.g. Agúndez et al. (2017); Paper II; Paper III).

Most conventional chemical models of AGB CSEs choose to focus either on the inner envelope non-equilibrium chemistry and dust formation (e.g. Gobrecht et al. 2016b; Boulangier et al. 2019) or on the photochemistry in the outer layers of the CSE (e.g. Millar & Herbst 1994; Li et al. 2016). While the inner-wind models typically do not take photochemistry into account, they include the effect of shocks caused by stellar pulsations (Cherchneff 2006; Boulangier et al. 2019). Such models have had reasonable success in predicting abundances that match estimates derived from observations, and in matching the observed trends in specific molecular abundances with mass-loss rate. A limitation of most of these models is that they ignore

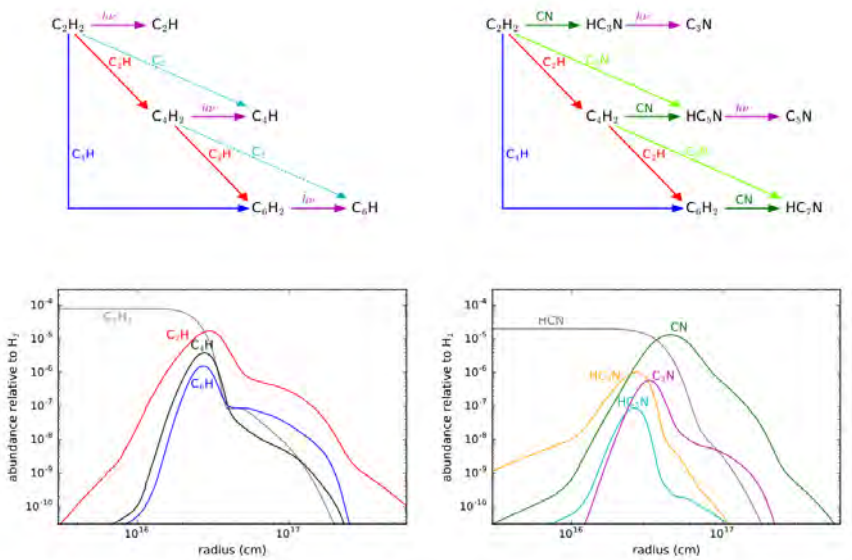

Figure 7.1: Schematic diagram of chemical reaction networks showing the growth of polyyne and cyanopolyyne carbon chains (top panels) and the fractional abundances of the same species derived from the chemical model as a function of radius (bottom panels) (Agúndez et al. 2020).

the effect of dust-gas interactions, though dust makes up a significant portion of AGB CSEs. This may affect the predicted molecular abundance profiles, particularly in the intermediate wind, where depletion onto dust grains is expected to occur (González Delgado et al. 2003; Massalkhi et al. 2019).

Newer models (e.g. Van de Sande et al. 2019) have attempted to resolve this issue by taking into account also the dust-gas interactions like accretion, thermal desorption, and non-thermal desorption in the chemical reaction networks, in addition to the regular gas-phase chemistry. There are also several other CSE chemical models that have been extensively used to study AGB circumstellar chemistry (e.g. Cordiner & Millar 2009; Van de Sande & Millar 2022; Van de Sande et al. 2019, 2020, 2021) which deal with various aspects of the chemistry including the effects of grain size distributions, density enhancements, clumpiness and porosity in the medium, the role of the radiation from the central AGB star, and the influence of stellar companions on photochemistry, among other factors.

7.2 Reaction networks

A reaction network is, simply put, a database of chemical reactions and their rates. There are several such chemical reaction networks that can be employed in chemical models, like the Kinetic Database for Astrochemistry (KIDA, Wakelam et al. 2015, 2024), the GRETOBAPE gas-phase reaction network (Tinacci et al. 2023), and the UMIST Database for Astrochemistry (UDfA, McElroy et al. 2013; Millar et al. 2024). They occasionally differ in the nature and extent of reactions taken into consideration, though most major networks include all the standard, well-known gas-phase reactions and their rates.

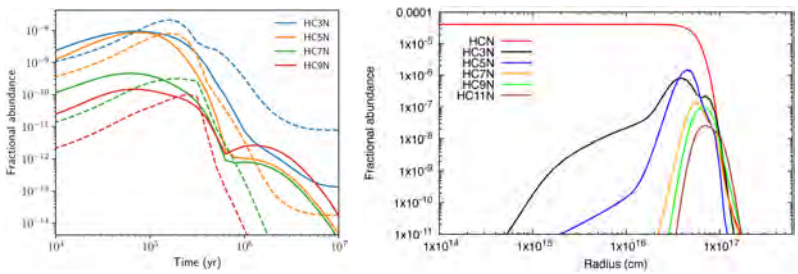

Figure 7.2: *Left*: Time evolution of cyanopolyyne abundances in an O-rich dark cloud model for the current `RATE22` (solid lines, Millar et al. 2024) and the previous `RATE12` (dashed lines, McElroy et al. 2013) reaction networks. *Right*: Radial variation in the cyanopolyyne abundances for a C-rich AGB CSE of gas MLR 3.0×10^{-5} $M_{\odot}$ yr^{-1} using the `RATE22` network (Millar et al. 2024).

Sample results from the publicly available UDfA `RATE12` (McElroy et al. 2013) and `RATE22` (Millar et al. 2024) reaction networks, showing the time and radial evolution of the modelled fractional abundances of various molecular species for different astronomical sources are shown in Fig. 7.2. In papers II and III, we used a 1D chemical model based on the latest version (UDfA `RATE22`, Millar et al. 2024) of this reaction network, which includes updated rate coefficients for 8767 reactions among 737 species, to calculate circumstellar molecular abundance profiles for our sources. The chemical model adopts the same physical CSE structure as described in Sect. 6.2. The modelling formalism is presented in Paper II. Our chemical model abundance profiles for SiO and SiS are shown along with those derived from our RT models in Fig. 7.3, reproduced from Paper III. We refer to Millar et al. (2000) and Van de Sande et al. (2018) for a detailed description of the specific chemical model

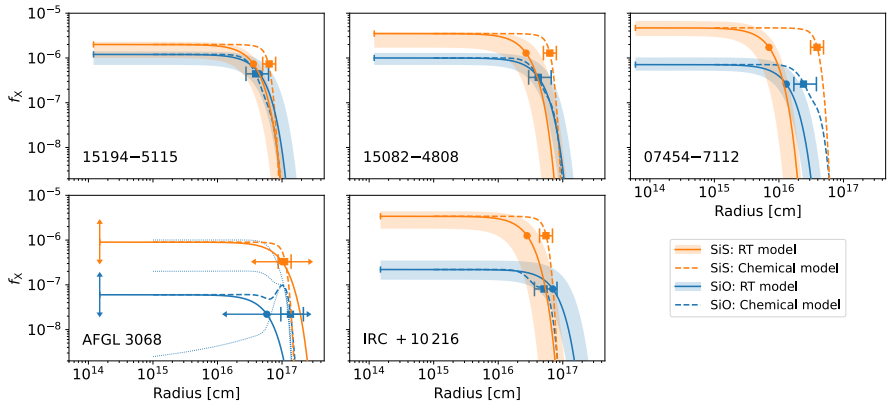

Figure 7.3: Comparison of abundance profiles obtained from RT modelling (solid lines with shaded uncertainties) and chemical modelling (dashed lines). The blue lines are for SiO, and the orange lines denote SiS. The shaded regions mark the 1σ uncertainty in the abundance profiles derived from RT modelling. The circles and squares denote the e-folding radii (R_e) of the RT modelled and chemical modelled abundance profiles, respectively. The open error bars on the peak abundance (f_0) and R_e for AFGL 3068, indicate that the abundance profile has not been well constrained by the RT models. The error bars on the chemical model R_e are based on reaction rate uncertainties (see Van de Sande et al. 2025). The blue dotted lines for AFGL 3068 show chemical model abundance profiles with different initial abundance values. See Paper III for a detailed discussion.

itself. Overall, comparing chemical modelling results to abundances derived from RT modelling offers a way to discern between the various theoretically predicted photodissociation rates of a given molecule (see Paper II). Further, chemical models can also predict the expected shapes of the radial abundance profiles of various molecular species, taking into account the different chemical processes that can enhance or suppress the abundances at different radial distances across the CSE (see Paper III).

8

Summary of appended papers

8.1 Paper - I

Paper I (Unnikrishnan et al. 2024) presents the analysis and results of the spatially resolved ALMA band 3 (84−116 GHz) spectral survey observations of three C-rich AGB stars, IRAS 15194− 5115, IRAS 15082−4808, and IRAS 07454−7112. We attempt to compare and contrast the chemistry in their CSEs with that of the well-studied C-star IRC +10 216, aiming to put to the test the archetype C-star status often attributed to it in the literature (e.g. Agúndez et al. 2012, 2017; Cernicharo et al. 2000, 2010, 2015; Cordiner & Millar 2009). The paper provides a more generalised characterisation of the physical and chemical properties of carbon-rich AGB CSEs beyond what is observed in IRC +10 216. These are the first high spatial-resolution observations of the circumstellar molecular emission from a sample of carbon-stars other than IRC +10 216, across large bandwidths.

The paper first introduces the existing literature on the subject, outlining the necessity of the present study. The properties of the chosen sources and the reasons for their selection are then described. The stars are all Mira variables and present similar physical outflow properties, possessing roughly spherical CSEs with similar expansion velocities. They trace around an order of magnitude in mass-loss rates,

from 3×10^{-6} $M_\odot$ yr^{-1} to around 1.6×10^{-5} $M_\odot$ yr^{-1} (Woods et al. 2003). However, they have very different $^{12}C/^{13}C$ ratios (Woods et al. 2003), indicative of differences in their nucleosynthetic histories. Thus, they are ideal candidates for a comparative study of carbon-rich circumstellar envelopes.

We observed the three sources in the full bandwidth of ALMA band 3 (84-116 GHz), using the main array (12 m) antennas. The details of the observations and data reduction methods used are described in detail in the paper, including the recalibration and re-imaging that had to be performed on the archival data due to its poor quality, and the data combination process employed to combine parts of our dataset with an overlapping frequency range dataset from an additional archival ALMA project.

From the high resolution ALMA data, we detected a large range of molecules, including both parent molecules like HCN, SiO, SiS and CS, and multiple daughter species ranging from simple nitrogen-bearing species like CN and HNC, to carbon chains (C_2H, C_4H, etc.) and also cyanopolynnes like HC_3N and HC_5N. In total, the survey yielded 311 identified lines, including hyperfine splitting components, from 141 transitions of 49 molecular species and their various isotopologues. We report multiple new detections towards the stars in the sample, including ^{29}SiO, ^{30}SiO, ^{29}SiS, ^{30}SiS, Si^{34}S, C^{33}S, Si^{13}CC, C_6H, C_8H, l−C_4H_2, and doubly ^{13}C−substituted isotopologues of HC_3N. Our analysis also revealed variability in the C_2H and HC_3N lines of our sources in the 3 mm band, as also seen towards IRC+102 16 (Cernicharo et al. 2014; Pardo et al. 2018).

The spatially resolved ALMA observations revealed a similar degree of morphological complexity in these sources, as seen previously in IRC+10216 (e.g. Agúndez et al. 2017; Velilla Prieto et al. 2019). Two main morphological categories are found in the line emission maps, namely *centrally-peaked* emission (from parent species, like HCN, SiO, SiS, and CS), and emission from a *shell* (from daughter species, including C_2H, C_3H, C_4H, c-C_3H_2, CN, C_3N, HC_5N, and HNC). Two species, HC_3N and SiC_2, present more complex brightness distributions characterised by both central and shell components. For IRAS 15194−5115 and IRAS 15082−4808, deviations from a smooth spherical CSE are evident, as the multiple well-resolved arc-like structures seen are traced by several species. These CSEs display complex structures, possibly indicative of the presence of binary companions (e.g. Lykou et al. 2018).

We determined the spatial extents of the emission from various molecules from the resolved emission maps, by producing azimuthally averaged radial profiles (AARPs) of the systemic-velocity emission and fitting them with Gaussians. Using the high spatial resolution of the ALMA observations, we compared the radial order of ap-

pearance of various molecules in our stars, which is directly correlated with CSE chemistry, to that of IRC +10 216 (e.g. Agúndez et al. 2017), and find them to be roughly the same. The observed spatial extent of the emission was used to constrain molecular LTE abundance estimates. For molecules with three or more detected transitions sufficiently well-separated in upper-level energies, we employed the population diagram method (Goldsmith & Langer 1999) to estimate the abundances. For other species, we present approximate analytical estimates of fractional abundances, produced using assumed excitation temperatures. Within the uncertainties of the data and analysis, we find that the calculated abundances are very similar among our sources and IRC +10 216, indicating that the general chemistry in these objects is highly similar.

We also estimated the isotopic ratios of silicon and sulphur in the envelopes, and they match reasonably well with the typical expected AGB values (Karakas & Lugaro 2016). The $^{12}C/^{13}C$ ratios were also calculated for each envelope, from multiple molecules, and were found to conform very well to the values in the literature (Woods et al. 2003), while also significantly improving their uncertainty estimates.

Overall, we conclude that the chemistry in the three envelopes is likely very similar to one another and to IRC +10 216 (Agúndez et al. 2017; Velilla Prieto et al. 2019; Cordiner & Millar 2009; He et al. 2008; Agundez 2009; Agúndez et al. 2012; Daniel et al. 2012; Gong et al. 2015; De Beck et al. 2012; Massalkhi et al. 2018), both in terms of the radial extents of the emission from various species, and molecular abundances. Detailed radiative transfer modelling is required to more rigorously constrain the molecular abundances. This is presented in Paper II and Paper III.

8.2 Paper - II

Paper II (Unnikrishnan et al. 2025) presents detailed non-LTE RT modelling of the dust and gas in the CSEs of five C-type AGB stars, followed by the derivation of their circumstellar carbon monosulfide (CS) fractional abundance profiles. The broad goals of this paper are to estimate stellar and circumstellar properties for the five stars, and to compare the CS abundances among the sources, to inform circumstellar chemical models. Continuing from Paper I, this work also helps assess if IRC+10216 is a good representative of the physics and chemistry of carbon-star CSEs in general. In addition to the three stars presented in Paper I, Paper II also includes two other sources, namely AFGL 3068, and IRC+10216 itself, both Mira variables with high mass-loss rates like the original sample.

Our RT analysis employed a standard spherically symmetric model of the CSE, which assumes a uniform, isotropic mass-loss rate ($\dot{M}$). Despite the presence of asymmetric features in the CSEs as seen in the ALMA observations (Paper I), this simplified geometry successfully yielded reasonable fits to the CO and CS spectral line profiles and the radial intensity profiles. Models that fully take into account the observed CSE sub-structure are beyond the scope of this work. In our CSE model, the dust condensation radius (R_c) was fixed at three stellar radii ($3R_\star$) to be consistent with dust-driven wind models (Höfner 2009; Bladh & Höfner 2012; Höfner & Olofsson 2018) and interferometric measurements (e.g. Wittkowski et al. 2007; Karovicova et al. 2011). The circumstellar gas density was assumed to decrease as r^{-2}, and the gas temperature was described by a power law. Distance estimates for all five stars were taken from Andriantsaralaza et al. (2022).

We first used the Monte Carlo RT code MCMax (Min et al. 2009) to model the SEDs of our sources. COMARCS model atmospheres (Aringer et al. 2019) were used as input stellar spectra for three of the five stars, and blackbody spectra were employed for the other two sources for which no good fits were obtained using models in the temperature range available for COMARCS (2500–3300 K). We used amorphous carbon dust grains, as expected in carbon-stars (Höfner & Olofsson 2018), to model the SED contribution from circumstellar dust. We tested different grain sizes in the ~0.1 - 1 μm range usually expected for AGB circumstellar dust (e.g. Mattsson et al. 2010; Höfner & Olofsson 2018, and references therein), and found that only the 1 μm grain size models yield good SED fits as long as R_c was fixed at $3R_\star$, as noted above. The trend that smaller grain sizes required very large R_c values ($> 10\,R_\star$) to reproduce the observed SEDs is also seen in several previous works in the literature (Ramstedt et al. 2008; Ramstedt & Olofsson 2014). Since an R_c much larger than 2-3 $R_\star$ would be incompatible with dust-driven wind models, we chose to keep R_c fixed at $3R_\star$ and employed a 1 μm grain size in our models. The models were constrained using photometric data compiled from various catalogues (e.g. Gaia Collaboration et al. 2023; Cutri et al. 2003; Price et al. 2010; Smith et al. 2004; Helou & Walker 1988; Ishihara et al. 2010; Yamamura et al. 2010; Planck Collaboration et al. 2011; Di Francesco et al. 2008). This analysis yielded the stellar luminosity ($L_\star$), stellar temperature ($T_\star$), the dust-MLR ($\dot{M}_d$), dust temperature profile across the CSE, and the optical depth at 10 μm.

With the stellar and dust parameters constrained, the next step was to estimate the gas properties in the CSEs. This was achieved by non-LTE RT modelling of the CO line emission using the Monte Carlo Program (MCP, Schöier & Olofsson 2001) RT

code. We adopted a typical value of 1×10^{-3} for the CO peak-abundance for all five stars (e.g. Danilovich et al. 2015). The grid of models had the gas mass-loss rate and gas temperature profile as free parameters. Integrated intensities calculated from multi-aperture spectra from Atacama Compact Array (ACA) data from the DEATH-STAR project (Ramstedt et al. 2020; Andriantsaralaza et al. 2021), when available, were used along with multi-transition single-dish line intensities sourced from the literature (Olofsson et al. 1993; Schöier & Olofsson 2001; Woods et al. 2003; Ramstedt et al. 2008; De Beck et al. 2010; Danilovich et al. 2015), to constrain the models.

After estimating the gas temperature profiles and mass-loss rates from the CO modelling, we derived the fractional abundance profiles of CS and its isotopologues (^{13}CS, C^{34}S) in our CSEs. CS is a parent molecule which is readily formed under thermodynamic equilibrium conditions in the inner envelopes of carbon-stars due to the ample availability of carbon (Agúndez et al. 2020; Danilovich et al. 2018). We used the 1D non-LTE accelerated lambda iteration (ALI) RT code (Rybicki & Hummer 1991; Maercker et al. 2008) to model the observed CS line emission.

Unlike previous works which made use of either single-dish line intensities (e.g. Danilovich et al. 2018) or a few selected interferometric maps (e.g. Velilla Prieto et al. 2019) to constrain such models, we present, for the first time for carbon-stars, molecular RT models constrained using both spatial information (line profiles and cumulative radial emission profiles from the ALMA data) and excitation information (the different J line intensities and line profile shapes from APEX, HIFI, IRAM 30m, and other single-dish data) simultaneously. We used centrally-peaked Gaussian abundance profiles for CS, with the peak abundance (f_0) at the inner edge of the envelope and the e-folding radius (R_e), being the two free parameters. A χ^2 minimisation technique, which took into account the correlated nature of the uncertainties on the line intensities extracted from the ALMA data, and weighed the spatial and excitation information equally, was used to determine the best-fit models.

Using the derived abundances of CS and its isotopologues ^{13}CS and C^{34}S, we estimated the ^{12}C/^{13}C and ^{32}S/^{34}S isotopic ratios for our stars. The ^{12}C/^{13}C ratios thus obtained were similar to those estimated previously from CO (Woods et al. 2003; Ramstedt & Olofsson 2014; Cernicharo et al. 2000; He et al. 2008). The possible reasons behind the extremely low ^{12}C/^{13}C ratio of IRAS 15194−5115 are discussed. The ^{32}S/^{34}S ratios were identical within uncertainties to the solar ^{32}S/^{34}S ratio of ∼20 (Asplund et al. 2009). This verifies the predictions from stellar yields models (Karakas & Lugaro 2016) which indicate no nucleosynthesis of sulphur at any stage of low/intermediate-mass stellar evolution up to the AGB.

Overall, the analysis revealed no significant differences between the derived CS abundance profile for the archetype IRC +10 216 and the other stars in the sample, beyond the expected variations driven by CSE density. This corroborates the use of IRC +10 216 as a representative object for studying circumstellar CS chemistry, at least for stars with high mass-loss rates, roughly in the range $\sim 0.5 - 5 \times 10^{-5} M_{\odot}$/yr. The derived radial extents (R_e) correlate well with circumstellar density, consistent with theoretical expectations and previous empirical trends. This indicates that the molecular envelope size is primarily set by photodissociation from the interstellar UV field, which is shielded more effectively in denser CSEs. We also confirmed that radiative pumping by infrared photons from the central star and the circumstellar dust is a dominant excitation mechanism for CS. The CS abundance profiles derived from the RT modelling show good agreement with predictions from state-of-the-art chemical kinetic models (Van de Sande et al. 2018) using the UMIST RATE22 database (Millar et al. 2024). Though we could not discern between the two predicted photodissociation rates for CS (Pattillo et al. 2018; Hrodmarsson & van Dishoeck 2023), beyond our estimated uncertainties, our derived abundance profiles match very well with those predicted by the chemical model.

This work demonstrates the advantage that using spatially resolved interferometric data and multi-transition single-dish data together to constrain RT models offers for breaking model degeneracies and refining abundance estimates. Similar modelling of the SiO and SiS line emission from these sources is presented in Paper III.

8.3 Paper - III

Paper III (Unnikrishnan et al. in prep.) deals with the non-LTE RT modelling of the molecular species SiO and SiS in C-type AGB CSEs. It includes the same source sample as in Paper II, and uses the same underlying CSE model based on the dust and CO results from Paper II. The aim of the paper is to derive the circumstellar abundance profiles for these species for the carbon-star sample, and compare the molecular abundances across the sources and with chemical model predictions. We used the 1D ALI RT code (Rybicki & Hummer 1991; Maercker et al. 2008) for our modelling. As done in Paper II for CS, our RT models in this work are also constrained by both morphological and excitation information obtained from spatially resolved ALMA maps and a large number of single-dish line observations, from telescopes including APEX, *Herschel*/HIFI, IRAM 30 m, and the Yebes 40 m. We model all available isotopologues of both SiO and SiS independently, using Gaussian

abundance profiles with the peak abundance and *e*-folding radius as free parameters. Overall, we obtain good fits to the SiO and SiS line profiles for all sources, and derive well-constrained abundance profiles and isotopic ratios. For AFGL 3068, we are not able to place strict constraints on the abundance profiles, due to the lack of spatially resolved observations for this source. It is seen from the results that *e*-folding radius increases with circumstellar gas density for both SiO and SiS. We also find that IR pumping (see Sect. 3.1) contributes significantly to the excitation of both SiO and SiS, as also seen for CS in Paper II.

In some cases, the analysis highlights the limitations inherent in 1D RT modelling using simplified stellar/circumstellar models, revealing the necessity for more complex modelling. For example, for SiO in IRC+10 216, we find that our RT models cannot fit the low- and high-J lines simultaneously. The large number of constraints available also demonstrates that usual methods, including varying the abundance profile shape in the inner CSE (e.g. Danilovich et al. 2019) do not manage to solve such mismatches, given the availability of multi-aperture spectra from the spatially resolved data.

We find that chemical models with and without dust-gas chemistry included do not show any significant differences in their SiO and SiS abundance profiles when using our dust and gas properties as inputs. This is because the dust around our stars is too warm (dust condensation temperature, T_c ~1500-1800 K) to produce significant depletion of gas-phase SiO and SiS onto the dust. Further, while the chemical models reproduce the derived SiO abundance profiles very well, they over-predict the radial extents of the SiS abundance profiles, indicating that the SiS photodissociation rate used in the chemical models is overestimated.

Overall, other than the changes in radial extents with circumstellar density, and a factor of ~5 spread in the derived peak abundances, we do not see any major differences between the abundance profiles for IRC+10 216 and the rest of the sources, for both SiO and SiS, affirming that also for the chemistry of these two species, IRC+10 216 can be regarded as a representative carbon-star, at least in the high-MLR regime which our source sample represents.

These results highlight the need for spatially resolved observations across multiple transitions probing a wide range of excitation conditions to study circumstellar chemistry in detail. Comprehensive radiative transfer modelling of various molecular species, guided by such data, and based on more complex models of the physical properties of the circumstellar gas and dust, is needed to robustly constrain circumstellar molecular abundances. The application of such modelling to a larger sample

of AGB stars spanning a broad range of mass-loss rates, particularly those lower than in our current sample, together with updated chemical models, is essential for developing a comprehensive understanding of molecular chemistry in carbon-star circumstellar envelopes.

9

Outlook

This thesis and the attached papers present a detailed investigation of the molecular chemistry in the circumstellar envelopes of a sample of carbon-rich (C-type) AGB stars, with the broad goal of obtaining a generalised understanding of the physical and chemical properties of such sources, and observationally verifying the archetypal status often attributed in the literature to the well-studied nearby carbon-star IRC+10216. This work is primarily based on an unbiased, spatially resolved ALMA band 3 spectral survey of the circumstellar molecular line emission from three C-type AGB stars other than IRC+10216, namely IRAS 15194-5115 (II Lup), IRAS 15082-4808 (V358 Lup), and IRAS 07454-7112 (AI Vol). We also utilise single-dish observations, including APEX spectral surveys (159 - 270 GHz) for the above three sources, along with AFGL 3068 and IRC 10 216; and APEX (272 - 376 GHz) and *Herschel*/HIFI (479.5–1121.9 GHz) surveys of IRAS 15194-5115. These surveys, in combination with the ALMA band 3 data, and auxiliary data where available, contain a wealth of emission line information which allows us to comprehensively explore the physical conditions prevalent in these CSEs, and determine their chemical compositions.

The scope of the current project, as described in this thesis, is limited to the study of chemistry in carbon-star CSEs. We also note that all stars in our sample are ex-

pected to be in the high mass-loss rate phase towards the end of their AGB evolution (Vassiliadis & Wood 1993). Similar studies of C-type and other AGB stars in lower mass-loss rate ranges present an avenue yet to be explored. The extension of such deep molecular spectral surveys and the subsequent physical and chemical analysis as presented here, into the regimes of M-type and S-type AGB stars is another logical next step. Only with such coordinated studies across the different AGB types can we hope to comprehensively understand the complex evolution taking place in this phase of stellar evolution, particularly given that the chemical evolution on the AGB is intricately linked to the physical properties and evolution of the stars itself (see e.g. Habing & Olofsson 2003; Höfner & Olofsson 2018). Such studies will also help expand the molecular inventories of circumstellar material across the different AGB types. As discussed in Paper III, the presence of a large number of strict spatial and excitation constraints illuminates the limitations inherent to 1D RT modelling of the observed line emission from these objects, using typical density/temperature/abundance profiles representative of smooth spherical envelopes. Proper treatment of the observed complex physical structure needs to be incorporated into RT models in order to obtain precisely constrained molecular abundances across the CSEs. 3D RT modelling of circumstellar line emission is therefore a plausible next step in this direction.

There is a lot of work to be done on understanding circumstellar morphological complexity as well. The observed complex structures, including arcs, shells, and spirals in AGB CSEs like those of IRC+10216 and the other sources in this work, are primarily thought to be due to the influence of binary companions (e.g. Decin et al. 2020; Lykou et al. 2018; Kim et al. 2015a; Kervella et al. 2016) on the mass loss from the central star. Direct detection of such companions, however, has proven to be extremely difficult, given the high luminosities of the AGB stars and the strong dust obscuration in their vicinity. The predicted existence of binary companions to AGB stars hence remains speculative to date, though binary population statistics indicate that at least 50% of stars on the AGB should have companions. High resolution circumstellar observational studies, in combination with hydrodynamical modelling (e.g. Maes et al. 2021; Malfait et al. 2021), can help to indirectly determine the properties of possible companions, as the observed density structures can be connected to binary parameters including companion type, mass, orbital separation, and eccentricity (see e.g. Cernicharo et al. 2015; Guélin et al. 2018; Decin et al. 2015; Kim et al. 2015b, 2017). Interestingly, molecular line observations can also help trace the possible chemical imprints of such binarity, for example, companion-induced

photochemistry (e.g. Siebert et al. 2022), and help verify predictions from chemical models (see Van de Sande & Millar 2022). Circumstellar observations can thus aid both hydrodynamical and chemical studies aimed at understanding the nature of binary companions of AGB stars. Dust formation in the wake of the companion (e.g. Montargès et al. 2025; Danilovich et al. 2025) is another potentially observable phenomenon that can help understand the nature of these stellar systems. Such additional dust formation is also important to constrain since it can affect mass-loss rate estimates.

Although an overall, broad understanding of the physics and chemistry on the AGB has been established (e.g. Habing & Olofsson 2003; Höfner & Olofsson 2018) and is being regularly updated through extensive modelling and observations, there are still many aspects of the AGB phase that are yet to be completely understood. Explaining the mass loss mechanism from first principles to develop a predictive theory of AGB mass loss, and characterising the nature and extent of the various complex chemical pathways and processes taking place in circumstellar envelopes, are just two major examples. Recent advances in our observing capabilities, such as the development of the Atacama Large Millimeter/submillimeter Array (ALMA), the James Webb Space Telescope (JWST), and the upcoming Square Kilometre Array (SKA), are opening up new and exciting avenues for the future of AGB research. ALMA now allows us to probe the molecular chemistry of AGB CSEs in unprecedented spatial resolution and sensitivity, revealing complex morphological structures and leading to the detection of more and more molecular species. Further, ALMA can now spatially resolve surface structures of nearby AGB stars (Vlemmings et al. 2024), revealing details that can improve our understanding of the mass loss mechanism in AGB stars. The SKA will enable the study of the dynamical atmospheres of a very large number of AGB stars at radio wavelengths, unveiling the origin of their stellar winds and exploring their dust-formation zones (Bojnordi Arbab et al. 2024). The planned new-generation Very Large Array (ngVLA) is also set to significantly advance both the resolution and sensitivity of such studies, across broader frequency ranges. The JWST can make the photometry and spectroscopy of AGB stars in nearby galaxies easier (e.g. Meixner 2011; Eriksson et al. 2014). Together, these instruments will allow us to explore the AGB in a broad range of wavelengths, and obtain a more comprehensive picture of these fantastic objects.

Bibliography

Agundez, M. 2009, Estudio de la Química en la Envoltura Circunestelar IRC +10216, PhD thesis, Center for Astrobiology, Madrid

Agúndez, M., Cernicharo, J., Quintana-Lacaci, G., et al. 2017, A&A, 601, A4

Agúndez, M., Fonfría, J. P., Cernicharo, J., et al. 2012, A&A, 543, A48

Agúndez, M., Martínez, J. I., de Andres, P. L., Cernicharo, J., & Martín-Gago, J. A. 2020, A&A, 637, A59

Akiyama, K. & Matthews, L. D. 2019, arXiv e-prints, arXiv:1910.00013

Alcolea, J., Agúndez, M., Bujarrabal, V., et al. 2022, Galaxies, 10, 47

Allain, T., Sedlmayr, E., & Leach, S. 1997, A&A, 323, 163

Andriantsaralaza, M. 2024, Mass Loss of Evolved Stars: Improving Mass-Loss Rates and Distances (Ph.D. thesis)

Andriantsaralaza, M., Ramstedt, S., Vlemmings, W. H. T., et al. 2021, A&A, 653, A53

Andriantsaralaza, M., Ramstedt, S., Vlemmings, W. H. T., & De Beck, E. 2022, A&A, 667, A74

Aringer, B., Marigo, P., Nowotny, W., et al. 2019, MNRAS, 487, 2133

Asplund, M., Grevesse, N., Sauval, A. J., & Scott, P. 2009, ARA&A, 47, 481

Belitsky, V., Lapkin, I., Fredrixon, M., et al. 2018, A&A, 612, A23

Bernes, C. 1979, A&A, 73, 67

Bladh, S. & Höfner, S. 2012, A&A, 546, A76

Blöcker, T. 2001, Ap&SS, 275, 1

Blommaert, J. A. D. L., de Vries, B. L., Waters, L. B. F. M., et al. 2014, A&A, 565, A109

Blommaert, J. A. D. L., Groenewegen, M. A. T., Okumura, K., et al. 2006, A&A, 460, 555

Bodenheimer, P. H. 2011, Principles of Star Formation

Bojnordi Arbab, B., Vlemmings, W., Khouri, T., & Höfner, S. 2024, ApJ, 976, 138

Born, M. & Oppenheimer, R. 1927, Annalen der Physik, 389, 457

Born, M. & Wolf, E. 1999, Principles of Optics

Boulangier, J., Gobrecht, D., Decin, L., de Koter, A., & Yates, J. 2019, MNRAS, 489, 4890

Bowen, G. H. 1988, ApJ, 329, 299

Briggs, D. S. 1995, High fidelity deconvolution of moderately resolved sources, PhD thesis, New Mexico Institute of Mining and Technology

Brinch, C. & Hogerheijde, M. R. 2010, A&A, 523, A25

Brown, J. M. & Millar, T. J. 2003, MNRAS, 339, 1041

Bujarrabal, V., Fuente, A., & Omont, A. 1994, A&A, 285, 247

Cabezas, C., Pardo, J. R., Agúndez, M., et al. 2023, A&A, 672, L12

Carpenter, J., Brogan, C., Iono, D., & Mroczkowski, T. 2023, in Physics and Chemistry of Star Formation: The Dynamical ISM Across Time and Spatial Scales, ed. V. Ossenkopf-Okada, R. Schaaf, I. Breloy, & J. Stutzki, 304

Carpenter, J., Iono, D., Kemper, F., & Wootten, A. 2020, arXiv e-prints, arXiv:2001.11076

Cernicharo, J., Cabezas, C., Pardo, J. R., et al. 2023, A&A, 672, L13

Cernicharo, J., Guélin, M., & Kahane, C. 2000, A&AS, 142, 181

Cernicharo, J., Marcelino, N., Agúndez, M., & Guélin, M. 2015, A&A, 575, A91

Cernicharo, J., Pardo, J. R., Agúndez, M., et al. 2025, A&A, 700, L20

Cernicharo, J., Teyssier, D., Quintana-Lacaci, G., et al. 2014, ApJ, 796, L21

Cernicharo, J., Waters, L. B. F. M., Decin, L., et al. 2010, A&A, 521, L8

Cherchneff, I. 2006, A&A, 456, 1001

Cherchneff, I., Barker, J. R., & Tielens, A. G. G. M. 1992, ApJ, 401, 269

Claussen, M. J., Sjouwerman, L. O., Rupen, M. P., et al. 2011, ApJ, 739, L5

Cordiner, M. A. & Millar, T. J. 2009, ApJ, 697, 68

Cornwell, T. J. 2008, IEEE Journal of Selected Topics in Signal Processing, 2, 793

Cotton, W. D. 2017, PASP, 129, 094501

Cutri, R. M., Skrutskie, M. F., van Dyk, S., et al. 2003, 2MASS All Sky Catalog of point sources.

Daniel, F., Agúndez, M., Cernicharo, J., et al. 2012, A&A, 542, A37

Danilovich, T., De Beck, E., Black, J. H., Olofsson, H., & Justtanont, K. 2016, A&A, 588, A119

Danilovich, T., Ramstedt, S., Gobrecht, D., et al. 2018, A&A, 617, A132

Danilovich, T., Richards, A. M. S., Decin, L., Van de Sande, M., & Gottlieb, C. A. 2020, MNRAS, 494, 1323

Danilovich, T., Richards, A. M. S., Karakas, A. I., et al. 2019, MNRAS, 484, 494

Danilovich, T., Samaratunge, N., Mori, Y., et al. 2025, arXiv e-prints, arXiv:2504.00517

Danilovich, T., Teyssier, D., Justtanont, K., et al. 2015, A&A, 581, A60

De Beck, E., Decin, L., de Koter, A., et al. 2010, A&A, 523, A18

De Beck, E., Lombaert, R., Agúndez, M., et al. 2012, A&A, 539, A108

De Beck, E. & Olofsson, H. 2018, A&A, 615, A8

De Beck, E. & Olofsson, H. 2020, A&A, 642, A20

de Graauw, T., Helmich, F. P., Phillips, T. G., et al. 2010, A&A, 518, L6

De Nutte, R., Decin, L., Olofsson, H., et al. 2017, A&A, 600, A71

Decin, L., Montargès, M., Richards, A. M. S., et al. 2020, Science, 369, 1497

Decin, L., Richards, A. M. S., Neufeld, D., et al. 2015, A&A, 574, A5

Di Francesco, J., Johnstone, D., Kirk, H., MacKenzie, T., & Ledwosinska, E. 2008, ApJS, 175, 277

Dinh-V-Trung & Lim, J. 2008, ApJ, 678, 303

Dorschner, J. 2010, in Lecture Notes in Physics, Berlin Springer Verlag, ed. T. Henning, Vol. 815, 1–60

Eriksson, K., Nowotny, W., Höfner, S., Aringer, B., & Wachter, A. 2014, A&A, 566, A95

Feast, M. W., Whitelock, P. A., & Marang, F. 2003, MNRAS, 346, 878

Fonfría, J. P., DeWitt, C. N., Montiel, E. J., Cernicharo, J., & Richter, M. J. 2022, ApJ, 927, L33

Gaia Collaboration, Vallenari, A., Brown, A. G. A., et al. 2023, A&A, 674, A1

Gail, H.-P. & Sedlmayr, E. 2013, Physics and Chemistry of Circumstellar Dust Shells

Gobrecht, D., Cherchneff, I., Sarangi, A., Plane, J. M. C., & Bromley, S. T. 2016a, A&A, 585, A6

Gobrecht, D., Cherchneff, I., Sarangi, A., Plane, J. M. C., & Bromley, S. T. 2016b, A&A, 585, A6

Goldsmith, P. F. & Langer, W. D. 1999, ApJ, 517, 209

Gong, Y., Henkel, C., Spezzano, S., et al. 2015, A&A, 574, A56

González, Á. 2024, in The Promises and Challenges of the ALMA Wideband Sensitivity Upgrade, 35

González Delgado, D., Olofsson, H., Kerschbaum, F., et al. 2003, A&A, 411, 123

Groenewegen, M. A. T., Barlow, M. J., Blommaert, J. A. D. L., et al. 2012, A&A, 543, L8

Guélin, M., Patel, N. A., Bremer, M., et al. 2018, A&A, 610, A4

Guerrero, M. A. & Manchado, A. 1996, ApJ, 472, 711

Guerrero, M. A., Ruiz, N., Hamann, W. R., et al. 2012, ApJ, 755, 129

Gullieuszik, M., Groenewegen, M. A. T., Cioni, M. R. L., et al. 2012, A&A, 537, A105

Güsten, R., Nyman, L. Å., Schilke, P., et al. 2006, A&A, 454, L13

Habing, H. J. & Olofsson, H. 2003, Asymptotic giant branch stars

He, J. H., Dinh-V-Trung, Kwok, S., et al. 2008, ApJS, 177, 275

Helou, G. & Walker, D. W., eds. 1988, Infrared Astronomical Satellite (IRAS) Catalogs and Atlases.Volume 7: The Small Scale Structure Catalog., Vol. 7

Herwig, F. 2005, ARA&A, 43, 435

Höfner, S. 2009, in Astronomical Society of the Pacific Conference Series, Vol. 414, Cosmic Dust - Near and Far, ed. T. Henning, E. Grün, & J. Steinacker, 3

Höfner, S., Bladh, S., Aringer, B., & Ahuja, R. 2016, A&A, 594, A108

Höfner, S., Bladh, S., Aringer, B., & Eriksson, K. 2022, A&A, 657, A109

Höfner, S. & Olofsson, H. 2018, A&A Rev., 26, 1

Högbom, J. A. 1974, A&AS, 15, 417

Hrodmarsson, H. R. & van Dishoeck, E. F. 2023, A&A, 675, A25

Huggins, P. J. & Glassgold, A. E. 1982, ApJ, 252, 201

Iben, Jr., I., Kaler, J. B., Truran, J. W., & Renzini, A. 1983, ApJ, 264, 605

Iben, I., J. 1975, ApJ, 196, 525

Iben, Icko, J. 1973, ApJ, 185, 209

Ishihara, D., Onaka, T., Kataza, H., et al. 2010, A&A, 514, A1

Jacoby, G. H. 1979, PASP, 91, 754

Karakas, A. I. & Lattanzio, J. C. 2014, PASA, 31, e030

Karakas, A. I. & Lugaro, M. 2010, PASA, 27, 227

Karakas, A. I. & Lugaro, M. 2016, ApJ, 825, 26

Karovicova, I., Wittkowski, M., Boboltz, D. A., et al. 2011, A&A, 532, A134

Kervella, P., Homan, W., Richards, A. M. S., et al. 2016, A&A, 596, A92

Khouri, T., Tafoya, D., Vlemmings, W. H. T., et al. 2025, A&A, 694, A222

Khouri, T., Vlemmings, W. H. T., Paladini, C., et al. 2020, A&A, 635, A200

Kim, H., Lee, H.-G., Mauron, N., & Chu, Y.-H. 2015a, ApJ, 804, L10

Kim, H., Liu, S.-Y., Hirano, N., et al. 2015b, ApJ, 814, 61

Kim, H. & Taam, R. E. 2012, ApJ, 744, 136

Kim, H., Trejo, A., Liu, S.-Y., et al. 2017, Nature Astronomy, 1, 0060

Kippenhahn, R. & Weigert, A. 1990, Stellar Structure and Evolution

Kobayashi, C., Karakas, A. I., & Lugaro, M. 2020, ApJ, 900, 179

Koelemay, L. A. & Ziurys, L. M. 2023, ApJ, 958, L6

Kraemer, K. E., Sloan, G. C., Keller, L. D., et al. 2019, ApJ, 887, 82

Kwok, S. 2007, Physics and Chemistry of the Interstellar Medium

Lamers, H. J. G. L. M. & Levesque, E. M. 2017, Understanding Stellar Evolution

LeBlanc, F. 2010, An Introduction to Stellar Astrophysics

Li, X., Millar, T. J., Heays, A. N., et al. 2016, A&A, 588, A4

Li, X., Millar, T. J., Walsh, C., Heays, A. N., & van Dishoeck, E. F. 2014, A&A, 568, A111

Liljegren, S. 2018, Stellar winds of cool giants: Investigating the mass-loss mechanism of AGB Stars, PhD thesis, Uppsala University, Sweden

Lykou, F., Zijlstra, A. A., Kluska, J., et al. 2018, MNRAS, 480, 1006

Maercker, M., Danilovich, T., Olofsson, H., et al. 2016a, A&A, 591, A44

Maercker, M., Schöier, F. L., Olofsson, H., Bergman, P., & Ramstedt, S. 2008, A&A, 479, 779

Maercker, M., Vlemmings, W. H. T., Brunner, M., et al. 2016b, A&A, 586, A5

Maes, S., Homan, W., Malfait, J., et al. 2021, A&A, 653, A25

Malfait, J., Homan, W., Maes, S., et al. 2021, A&A, 652, A51

Markwick, A. J. 2000, Chemistry in dynamically evolving astrophysical regions, PhD thesis, University of Manchester, Institute of Science and Technology

Massalkhi, S., Agúndez, M., & Cernicharo, J. 2019, A&A, 628, A62

Massalkhi, S., Agúndez, M., Cernicharo, J., et al. 2018, A&A, 611, A29

Massalkhi, S., Agúndez, M., Fonfría, J. P., et al. 2024, A&A, 688, A16

Mattsson, L., Wahlin, R., & Höfner, S. 2010, A&A, 509, A14

McElroy, D., Walsh, C., Markwick, A. J., et al. 2013, A&A, 550, A36

McGuire, B. A. 2022, ApJS, 259, 30

McKee, C. F. & Ostriker, E. C. 2007, ARA&A, 45, 565

Meixner, M. 2011, in Astronomical Society of the Pacific Conference Series, Vol. 445, Why Galaxies Care about AGB Stars II: Shining Examples and Common Inhabitants, ed. F. Kerschbaum, T. Lebzelter, & R. F. Wing, 555

Menten, K. M., Reid, M. J., Kamiński, T., & Claussen, M. J. 2012, A&A, 543, A73

Millar, T. J. & Herbst, E. 1994, A&A, 288, 561

Millar, T. J., Herbst, E., & Bettens, R. P. A. 2000, MNRAS, 316, 195

Millar, T. J., Walsh, C., Van de Sande, M., & Markwick, A. J. 2024, A&A, 682, A109

Min, M., Dullemond, C. P., Dominik, C., de Koter, A., & Hovenier, J. W. 2009, A&A, 497, 155

Montargès, M., Malfait, J., Esseldeurs, M., et al. 2025, A&A, 699, A22

Mueller, M., Jellema, W., Olberg, M., Moreno, R., & Teyssier, D. 2014, The HIFI Beam: Release 1, Release Note for Astronomers, Tech. rep., Tech. Rep. HIFI-ICC-RP-2014-001, v1. 1, HIFI-ICC

Müller, H. S. P., Schlöder, F., Stutzki, J., & Winnewisser, G. 2005, Journal of Molecular Structure, 742, 215

Neugebauer, G. & Leighton, R. B. 1969, Two-micron sky survey. A preliminary catalogue

Ng, K. C. 1974, J. Chem. Phys., 61, 2680

Nyman, L. A., Olofsson, H., Johansson, L. E. B., et al. 1993, A&A, 269, 377

Olofsson, H., Eriksson, K., & Gustafsson, B. 1990, A&A, 230, 405

Olofsson, H., Eriksson, K., Gustafsson, B., & Carlstroem, U. 1993, ApJS, 87, 305

Olofsson, H., Khouri, T., Sargent, B., et al. in prep., Manuscript intended for submission to A&A

Olofsson, H., Khouri, T., Sargent, B. A., et al. 2022, A&A, 665, A82

Olofsson, H., Lindqvist, M., Nyman, L. A., & Winnberg, A. 1998, A&A, 329, 1059

Paladini, C., Baron, F., Jorissen, A., et al. 2018, Nature, 553, 310

Paladini, C., Klotz, D., Sacuto, S., et al. 2017, A&A, 600, A136

Pardo, J. R., Cernicharo, J., Tercero, B., et al. 2022, A&A, 658, A39

Pardo, J. R., Cernicharo, J., Velilla Prieto, L., et al. 2018, A&A, 615, L4

Pardo, J. R., Fonfría, J. P., Agúndez, M., et al. 2025, A&A, 700, L6

Patel, N. A., Young, K. H., Gottlieb, C. A., et al. 2011, ApJS, 193, 17

Pattillo, R. J., Cieszewski, R., Stancil, P. C., et al. 2018, ApJ, 858, 10

Peraiah, A. 2001, An Introduction to Radiative Transfer: Methods and Applications in Astrophysics

Pilbratt, G. L., Riedinger, J. R., Passvogel, T., et al. 2010, A&A, 518, L1

Planck Collaboration, Ade, P. A. R., Aghanim, N., et al. 2011, A&A, 536, A7

Price, S. D., Smith, B. J., Kuchar, T. A., Mizuno, D. R., & Kraemer, K. E. 2010, ApJS, 190, 203

Ramstedt, S. & Olofsson, H. 2014, A&A, 566, A145

Ramstedt, S., Schöier, F. L., Olofsson, H., & Lundgren, A. A. 2008, A&A, 487, 645

Ramstedt, S., Vlemmings, W. H. T., Doan, L., et al. 2020, A&A, 640, A133

Rau, U., Naik, N., & Braun, T. 2019, AJ, 158, 3

Revéret, V., André, P., Le Pennec, J., et al. 2014, in Society of Photo-Optical Instrumentation Engineers (SPIE) Conference Series, Vol. 9153, Millimeter, Submillimeter, and Far-Infrared Detectors and Instrumentation for Astronomy VII, ed. W. S. Holland & J. Zmuidzinas, 915305

Roelfsema, P. R., Helmich, F. P., Teyssier, D., et al. 2012, A&A, 537, A17

Rybicki, G. B. & Hummer, D. G. 1991, A&A, 245, 171

Rybicki, G. B. & Lightman, A. P. 1986, Radiative Processes in Astrophysics

Saberi, M., Vlemmings, W. H. T., & De Beck, E. 2019, A&A, 625, A81

Sackmann, I. J., Smith, R. L., & Despain, K. H. 1974, ApJ, 187, 555

Salaris, M. & Cassisi, S. 2005, Evolution of Stars and Stellar Populations

Schöier, F. L. 2000, Winds from red giant stars: observations and modelling of molecular line emission, PhD thesis, Stockholm University, Department of Astronomy

Schöier, F. L., Maercker, M., Justtanont, K., et al. 2011, A&A, 530, A83

Schöier, F. L. & Olofsson, H. 2001, A&A, 368, 969

Schöier, F. L., Ramstedt, S., Olofsson, H., et al. 2013, A&A, 550, A78

Sedlmayr, E. & Dominik, C. 1995, Space Sci. Rev., 73, 211

Shipman, R. F., Beaulieu, S. F., Teyssier, D., et al. 2017, A&A, 608, A49

Siebert, M. A., Van de Sande, M., Millar, T. J., & Remijan, A. J. 2022, ApJ, 941, 90

Sloan, G. C., Little-Marenin, I. R., & Price, S. D. 1998, AJ, 115, 809

Smith, B. J., Price, S. D., & Baker, R. I. 2004, ApJS, 154, 673

Smith, C. L., Zijlstra, A. A., & Fuller, G. A. 2015, MNRAS, 454, 177

Stahler, S. W. & Palla, F. 2004, The Formation of Stars

Sugimoto, D. & Nomoto, K. 1975, PASJ, 27, 197

Suh, K.-W. 2000, MNRAS, 315, 740

Tafoya, D., Toalá, J. A., Unnikrishnan, R., et al. 2022, ApJ, 925, L4

Tafoya, D., van Hoof, P. A. M., Toalá, J. A., et al. 2023, A&A, 677, L8

Taylor, G., Carilli, C., & Perly, R. 1999, in Astronomical Society of the Pacific Conference Series, Vol. 180, Synthesis Imaging in Radio Astronomy II

Thompson, A. R., Moran, J. M., & Swenson, George W., J. 2017, Interferometry and Synthesis in Radio Astronomy, 3rd Edition

Tielens, A. G. G. M. 2005, The Physics and Chemistry of the Interstellar Medium

Tinacci, L., Ferrada-Chamorro, S., Ceccarelli, C., et al. 2023, ApJS, 266, 38

Toalá, J. A., Lora, V., Montoro-Molina, B., Guerrero, M. A., & Esquivel, A. 2021, MNRAS, 505, 3883

Toonen, S., Hamers, A., & Portegies Zwart, S. 2016, Computational Astrophysics and Cosmology, 3, 6

Tosi, S., Dell'Agli, F., Huerta-Martinez, E., & Ventura, P. 2022, Universe, 8, 270

Unnikrishnan, R., Andriantsaralaza, M., De Beck, E., et al. 2025, A&A, 699, A48

Unnikrishnan, R., De Beck, E., Nyman, L. Å., et al. in prep., Manuscript intended for submission to A&A

Unnikrishnan, R., De Beck, E., Nyman, L. Å., et al. 2024, A&A, 684, A4

Van de Sande, M., Gueguen, M., Danilovich, T., & Millar, T. J. 2025, MNRAS

Van de Sande, M. & Millar, T. J. 2019, ApJ, 873, 36

Van de Sande, M. & Millar, T. J. 2022, MNRAS, 510, 1204

Van de Sande, M., Sundqvist, J. O., Millar, T. J., et al. 2018, A&A, 616, A106

Van de Sande, M., Walsh, C., & Danilovich, T. 2020, MNRAS, 495, 1650

Van de Sande, M., Walsh, C., Mangan, T. P., & Decin, L. 2019, MNRAS, 490, 2023

Van de Sande, M., Walsh, C., & Millar, T. J. 2021, MNRAS, 501, 491

van der Tak, F. F. S., Black, J. H., Schöier, F. L., Jansen, D. J., & van Dishoeck, E. F. 2007, A&A, 468, 627

Vassilev, V., Meledin, D., Lapkin, I., et al. 2008, A&A, 490, 1157

Vassiliadis, E. & Wood, P. R. 1993, ApJ, 413, 641

Velilla Prieto, L., Cernicharo, J., Agúndez, M., et al. 2019, A&A, 629, A146

Velilla Prieto, L., Cernicharo, J., Quintana-Lacaci, G., et al. 2015, ApJ, 805, L13

Velilla Prieto, L., Sánchez Contreras, C., Cernicharo, J., et al. 2017, A&A, 597, A25

Ventura, P., Dell'Agli, F., Schneider, R., et al. 2014, MNRAS, 439, 977

Vlemmings, W., Khouri, T., Bojnordi Arbab, B., De Beck, E., & Maercker, M. 2024, Nature, 633, 323

Wakelam, V., Gratier, P., Loison, J. C., et al. 2024, A&A, 689, A63

Wakelam, V., Loison, J. C., Herbst, E., et al. 2015, ApJS, 217, 20

Ward-Thompson, D. & Whitworth, A. P. 2011, An Introduction to Star Formation

Whitelock, P. A., Feast, M. W., Marang, F., & Groenewegen, M. A. T. 2006, MNRAS, 369, 751

Willson, L. A. 2000, ARA&A, 38, 573

Wilson, T. L., Rohlfs, K., & Hüttemeister, S. 2013, Tools of Radio Astronomy

Winters, J. M., Le Bertre, T., Jeong, K. S., Helling, C., & Sedlmayr, E. 2000, A&A, 361, 641

Wittkowski, M., Boboltz, D. A., Ohnaka, K., Driebe, T., & Scholz, M. 2007, A&A, 470, 191

Wood, P. R. 1979, ApJ, 227, 220

Woodruff, H. C., Ireland, M. J., Tuthill, P. G., et al. 2009, ApJ, 691, 1328

Woods, P. M., Schöier, F. L., Nyman, L. Å., & Olofsson, H. 2003, A&A, 402, 617

Yamamura, I., Makiuti, S., Ikeda, N., et al. 2010, VizieR Online Data Catalog: AKARI/FIS All-Sky Survey Point Source Catalogues (ISAS/JAXA, 2010), VizieR On-line Data Catalog: II/298. Originally published in: ISAS/JAXA (2010)

Yang, B., Stancil, P. C., Balakrishnan, N., & Forrey, R. C. 2010, ApJ, 718, 1062

Zawadzki, B., Czekala, I., Loomis, R. A., et al. 2023, PASP, 135, 064503

Zijlstra, A. A., Matsuura, M., Wood, P. R., et al. 2006, MNRAS, 370, 1961